Observation of Quantum Beats and Mediated Interactions

Polarons in Bose-Einstein Condensates

Andreas Madsen Morgen
Department of Physics and Astronomy
Aarhus University, Denmark

Ph.D. Thesis
August 2024

Front cover illustration: Formation of polarons and bipolarons in a Bose-Einstein Condensate with the presence of three-body recombinations.

Abstract

Ultracold quantum gases offer a high degree of experimental control and constitute an ideal framework for exploring complex quantum systems. One such case is the paradigmatic example of an electron moving in a crystal lattice, which is difficult to investigate experimentally in condensed matter physics. However, this scenario can be simulated in ultracold quantum gases by embedding an impurity into the gas, which then interacts with its surrounding medium. Such a system is successfully described in the quasiparticle framework, where the resulting polaron emerges. The polaron represents an intriguing many-body quantum system, with numerous technological prospects.

In this thesis, Bose-Einstein Condensates of ^{39}K are utilized to explore multiple aspects of the polaron. These include the short-time dynamics of an impurity suddenly embedded into the condensate, at repulsive impurity-medium interactions where two polaron states exist. Using an interferometric sequence, the polaron formation is captured and a quantum beat effect between the polaron states is observed. Benchmarking the system requires accurate knowledge of the medium density, which sets important parameters used for comparing extracted results with theoretical predictions. A detailed analysis of the loss processes in the system is therefore provided, to adequately determine the density at a variable point in the experimental sequence. Finally, spectroscopic measurements are presented, which provide access to the spectral response of the impurity, used for extracting the properties of the polaron. An additional signal is also observed that is interpreted as arising from an induced interaction between two polarons, the so-called bipolaron.

These results expand on the current understanding of the properties of the polaron, especially in regimes where contemporary theories disagree. They also provide insight to resolve the outstanding discrepancies and point to new areas for exploring impurity physics further.

Resumé

Danish Abstract

Ultrakolde kvante gasser tillader et højt niveau af eksperimentel kontrol og sætter de ideelle rammer for at udforske komplekse kvante systemer. Et eksempel herpå, er det paradigmatiske billede af en elektron der bevæger sig i et krystal gitter, hvilket er svært at undersøge eksperimentelt i faststoffysik. Dette kan dog simuleres i ultrakolde kvante gasser ved at indsætte en urenhed i gassen, som interagerer med det omgivende medium. Et sådan system kan beskrives i konteksten af kvasipartikler, hvor den resulterende polaron opstår. Polaronen repræsenterer et spændende mange-legeme kvante system, med adskillige teknologiske muligheder.

I denne afhandling bliver Bose-Einstein kondensater af ^{39}K brugt til at udforske forskellige aspekter af polaronen. Disse inkluderer kort-tids dynamikken når en urenhed pludselig bliver indsat i kondensatet, i tilfældet af repulsive unrenhed-medium interaktioner hvor to polaron tilstande eksisterer. Ved at bruge en interferometrisk sekvens, opfanges polaron formationen og en kvante beat effekt mellem de to polaron tilstande observeres. Benchmarking af systemet kræver nøjagtig viden om medium densiteten, som definerer vigtige parametre der bruges til at sammenligne de ekstraherede resultater med teorier. En dybdegående analyse af tabs processerne i systemet gives for at kunne bestemme medium densiten på et vilkårligt tidspunkt i den eksperimentelle sekvens. Endeligt bliver spektroskopiske målinger præsenteret for at kunne ekstrahere polaronens egenskaber, og et signal bliver observeret der tolkes som opstået grundet induceret interaktioner mellem to polaroner, også kaldet bipolaronen.

Resultaterne udvider den nuværende forståelse af polaronens egenskaber særligt i regimer hvor nuværende teorier er uenige. De giver også indsigt i hvordan de udestående uoverensstemmelser kan løses, såvel som nye områder hvor urenhedsfysik kan udforskes yderligere.

Preface

This thesis represents the conclusion of my PhD studies here at Aarhus University after 3.5 years. Although my PhD officially began in November 2020, I had already previously done my bachelor project as well as student colloquium within the group. Both of these projects piqued my interest in the field of atomic physics and naturally directed me toward the group for doing a PhD.

I am therefore very thankful to my supervisor Jan Arlt, for giving me the opportunity to join the group as well as for the support and countless scientific discussions over the years.

At the start of my PhD, COVID-19 lockdowns were still around and my involvement in the experiment had to be delayed until February 2021. I started in the MIX laboratory, where I had the pleasure of joining Magnus and Thomas, who taught me how to run the experiment. I am very thankful for this, as well as their warm welcome to the group. As both Magnus and Thomas finished their PhD's in the summer of 2021, I soon became the sole PhD student in the MIX laboratory. A big thank you therefore goes to Toke, who was in the neighboring laboratory, the so-called Lattice experiment, and the only other PhD student in the group for a time. I am grateful for the scientific and personal discussions we have had over the years.

In the summer of 2022, I was fortunate to be joined in the laboratory by PhD student Søren, with whom I have enjoyed spending time with in the laboratory as well as sharing the frustrations that follow from working on the experiment. Around this time, the group grew with both Malthe and Laurits joining the Lattice experiment, as well as recently with Ilja and Morten joining the Lattice and MIX team. I am sure you will all go on to achieve great results in the future!

Finally, the biggest thank you goes to my girlfriend for her love and support over the years. The conclusion of this thesis also marks the start of a great journey we are about to embark on, which I am very much looking forward to.

Andreas Madsen Morgen

List of publications

- M. G. Skou, K. K. Nielsen, T. G. Skov, A. M. Morgen, N. B. Jørgensen, A. Camacho-Guardian, T. Pohl, G. M. Bruun and J. J. Arlt, ‘Life and death of the Bose polaron’, Physical Review Research **4**, 043093 (2022).
- A. M. Morgen, S. S. Balling, K. K. Nielsen, T. Pohl, G. M. Bruun and J. J. Arlt, ‘Quantum beat spectroscopy of repulsive bose polarons’, arXiv:2310.18183 (2023).
- A. M. Morgen, S. S. Balling, M. T. Strøe, M. G. Skou and J. J. Arlt, ‘Three-body Physics in the Impurity Limit in ^{39}K’, In preparation (2024).
- A. M. Morgen, S. S. Balling, M. T. Strøe, K. K. Nielsen, T. Pohl, G. M. Bruun and J. J. Arlt, ‘Observation of Deeply Bound Polaronic States’, In preparation (2024).

Contents

CHAPTER 1

Introduction

At the beginning of the 20th century, the development of quantum mechanics revolutionized the way we think about physics, signaling a paradigm shift from classical physics. Starting with Max Planck's successful description of black-body radiation by considering energy only in specific integers, or *quanta* [5], this notion was extended by Albert Einstein and Niels Bohr, to describe the photoelectric effect [6] and the hydrogen atom [7]. The breakthrough of Louis de Broglie by describing the wave properties of matter, paved the way for modern quantum mechanics in the subsequent work of Erwin Schrödinger, Werner Heisenberg, Max Born, and Pascual Jordan. Wave mechanics, encapsulated in the famous Schrödinger equation, allowed for an accurate description of experimental results.

Although more than 100 years old, the effects and consequences of quantum mechanics continue to challenge and defy our intuition. The astonishing nature of quantum systems is highlighted by experiments, ranging from the legendary Stern-Gerlach experiment, revealing the spin property of atomic particles [8], to the continuously performed Bell tests, furthering our understanding of inherent limitations to the available information of quantum systems [9–12].

1.1 Ultracold Quantum Gases

Despite revolutionizing physics, the effects of quantum mechanics are not observable in our daily lives. Therefore, macroscopic quantum systems stand out as something truly unique and act as windows into the quantum world. In the novel work of Satyendra N. Bose and Einstein, they applied quantum statistics to an atomic bosonic ensemble and showed that at sufficiently low temperatures the atoms would occupy the same quantum state [13, 14]. The resulting Bose-Einstein Condensate (BEC), a new state of matter, exhibits properties only described by quantum mechanics. It is the inherent property of bosons that allows them to occupy the same quantum state and enables this condensation, in contrast to fermions which do not have this property. It would take 70 years from the proposal of Bose and Einstein before the experimental realization and observation of condensation for dilute alkali gases were obtained [15, 16]. In ultracold Fermi gases, the Pauli exclusion principle prevents the pile-up of atoms in the same quantum state, forcing them into higher energy states instead [17].

The progress of modern quantum mechanics has also led to important technological inventions, such as the laser [18] and transistor [19]. As technology is continuously pushed forward, new quantum technologies are being developed for areas such as sensing and metrology, communication, computing, and simulation [20]. The idea of quantum simulation is to realize a versatile quantum system to study theories that are otherwise difficult to test [21]. An atomic gas cooled to ultracold temperatures is an excellent candidate for such a system and is often referred to as the analog quantum computer [22]. The controlled environment posed by optical and magnetical potentials allows for tailoring the system to the desired specifications. The experimental efforts to realize Bose-Einstein Condensation as well as ultracold Fermi gases, have provided the techniques for efficient trapping and manipulation of the atoms. In particular, the tunability of the interaction between atoms by using so-called *Feshbach resonances*, has opened up for a variety of research directions [23, 24]. Although initially restricted primarily to alkali atoms, extensive efforts have been made towards achieving condensation of the more exotic rare-earths [25–28], furthering the available atomic species options.

Ultracold quantum gases have cemented themselves as excellent experimental playgrounds, finding usages in simulating various areas of physics such as superconductors [29], dark matter [30, 31], black holes [32], superfluidity [33] and light manipulation [34].

1.2 Impurity Physics

The concept of impurities is found in many areas of physics, such as astronomy [35, 36], nuclear physics [37, 38] as well as material science and chemistry [39, 40]. More relatable, impurities play an important role in the characteristic color of gemstones [41], as well as cloud formation where dust particles act as nucleation sites for water condensation [42].

In condensed matter physics, an electron moving in an atomic lattice is a classical example of impurity physics. The interactions between the electron and atoms distort the lattice, leading to excitations and a consequent dressing of the electron, as illustrated in Fig. 1.1. To describe this, Lev Landau and Solomon Pekar used the so-called *quasi-particle* framework, where the electron and the phononic lattice excitations are considered together as a new single particle, the *polaron* [43].

In the context of ultracold quantum gases, the above scenario may be simulated by embedding an impurity into the medium, as illustrated in Fig. 1.1. This allowed for the first experimental realization of the Fermi polaron in ultracold degenerate Fermi gases [45–50], with the Bose polaron observed later in a BEC [51, 52]. The Bose polaron is of special interest since the bosonic nature of the medium atoms provides a closer resemblance to the original scenario of an electron coupling to the phononic vibrations in the crystal lattice. Although the result of many-body correlations, the properties of the Bose polaron are effectively described by few-body

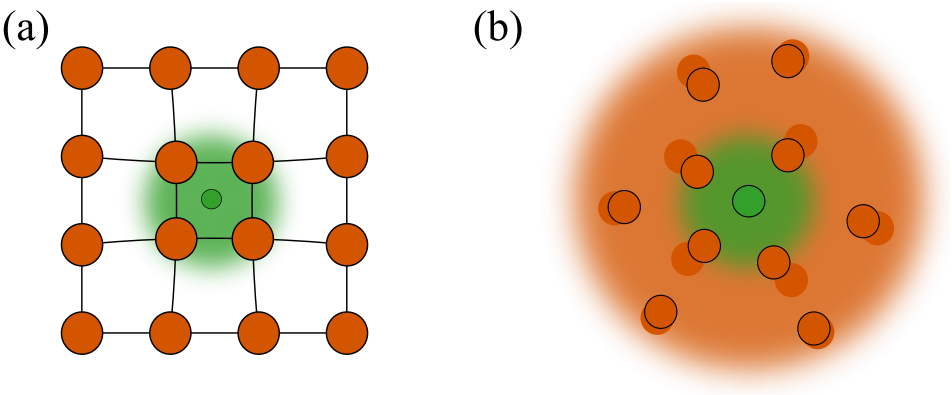

FIGURE 1.1: **(a)** In condensed matter physics, the polaron emerges due to interactions between an electron and atoms in a crystal lattice. **(b)** In ultracold quantum gases, a similar system can be realized, where an impurity interacts with the surrounding medium. Adapted from [44].

parameters. As an example, by tuning the two-body interaction between the impurity and medium atoms, the energy of the impurity is varied. Spectroscopy allowed for observation of this characteristic energy shift for both attractive and repulsive interactions [45, 47, 51–54]. Furthermore, using an interferometric technique, the initial dynamical evolution of the impurity towards the formation of the polaron was realized in a Fermi gas for both attractive and repulsive impurity-medium interactions [55, 56] and later in a BEC for attractive interactions [57]. This formation is signaled by a distinct crossover from two-body interactions into a many-body dynamical regime [1]. For the case of repulsive impurity-medium interactions, the dynamical evolution of the impurity is inherently more complicated and has not been investigated in detail for the Bose polaron, until now.

Two polarons may couple to each other by mediated interactions through their environment, leading to a direct induced interaction between them that is inherently attractive and could support the formation of a bound state known as the *bipolaron* [58–61]. Induced interactions also lead to Cooper pairing in conventional superconductors [62] and have numerous technological prospects [63–66]. However, the binding energy of this state is only expected to be significant at large attractive impurity-medium interaction strengths, making it experimentally challenging to measure. Additionally, it is debated whether such a state exists, given that the accumulation of medium atoms at a single impurity could lead to the formation of large clusters, with a similar experimental signal as the bipolaron [67]. Distinguishing between such signals imposes further restrictions on the experimental parameters as well as the data analysis. Recently, investigation of mediated interactions in a Fermi gas has led to the observation of an energy shift of the attractive and repulsive branches, with a difference in the direction of the observed shift for a bosonic and fermionic impurity [68]. This observation highlights that the mediated interactions can also affect the single impurity properties. Finally, mediated interactions in Bose-Fermi mixtures [69] as well as between ions embedded in quantum degenerate gases have also recently been proposed [70], showcasing the broad interest and application of this phenomena.

1.3 Few-Body Physics

Few-body physics plays a central role in ultracold quantum gases, as low-energy elastic collisions dominate the interactions. Ostensibly simple, the quantum mechanical treatment of few-body physics is highly non-trivial. The seminal work by Vitaly Efimov predicted the existence of an infinite series of bound states between three identical bosons, interacting resonantly pairwise [71, 72]. Remarkably, such Efimov trimers may form even in the absence of two-body bound states, which has been experimentally observed in ultracold quantum gases [73–77]. In particular, the Efimov effect can be considered as a mediated interaction between two particles by a third and has been extended to cover both fermions and multi-component systems, for which rich features arise by tuning the mass differences and interactions [78].

A closely related concept is the three-body recombination process, where three atoms collide, with two of the atoms forming a molecule and the third atom receiving the leftover energy. Such processes are prevalent in BECs due to the bosonic nature of the atoms, which allows them to occupy the same space. In the context of impurity physics, three-body physics is important both for characterizing the losses it imposes on the system, but also for understanding how these Efimov-like correlations affect the properties of the polaron [67, 79, 80].

1.4 Thesis Outline

The thesis is structured as follows:

Chapter 2: Ultracold Quantum Gases & Polaron Physics
A theoretical description of ultracold quantum gases is given and models for the polaron are reviewed.
Chapter 3: Experimental Cooling and Detection Techniques
A brief overview of the experimental apparatus is provided, together with a description of the sequence for the production and detection of Bose-Einstein Condensates for our system.
Chapter 4: Loss Spectroscopy and Three-body Physics
The different spectroscopy techniques utilized in this thesis are explained, which are used for examining the loss processes in the system. Modeling the loss processes is important for accurately determining the density of the system, which is presented in a publication.
Chapter 5: Observation of Deeply Bound Polaronic States
Utilizing a two-pulse spectroscopy sequence, the spectral response of the

polaron is investigated in detail, and a signal at lower energies is observed which is interpreted as a bipolaron response.

Chapter 6: Impurity Dynamics with Repulsive Interactions

An interferometric sequence is used for resolving the initial dynamics of an impurity interacting repulsively with a medium. This is presented in a publication, where the dynamical regimes are examined and the energies of the two polaron branches are extracted and compared to theoretical predictions.

Chapter 7: Conclusion & Outlook

The conclusions of the thesis are provided and future possible experiments are discussed in an outlook.

In accordance with GSNS rules, parts of this thesis were also used in the progress report for the qualifying examination.

CHAPTER 2

Ultracold Quantum Gases & Polaron Physics

To investigate impurity physics in quantum gases, a good theoretical understanding of both, is necessary. The purpose of this chapter is to examine the key properties of Bose-Einstein Condensates and Bose polarons.

The structure of this chapter is as follows. A brief introduction to Bose-Einstein Condensation is given in Sec. 2.1 and in Sec. 2.2 a theoretical model for the inclusion of interactions is provided, with the experimental method for tuning it. Few-body physics for ultracold quantum gases are discussed in Sec. 2.3. Finally, in Sec. 2.4, the theoretical framework of the polaron is presented and the role of mediated interactions is discussed.

The review of the subjects in Sec. 2.1 and Sec. 2.2 are based on the theoretical introduction given in Ref. [81]

2.1 Bose-Einstein Condensation

A non-interacting thermal gas of atoms displays a classical behavior and the atoms are distributed according to their energies as described by the Boltzmann distribution

$$f(\epsilon_\nu) = e^{-(\epsilon_\nu - \mu)/k_B T}, \tag{2.1}$$

where ϵ_ν is the energy, k_B is the Boltzmann constant, T the temperature and μ is the chemical potential. If the temperature is lowered sufficiently, the wavefunctions of the atoms begin to overlap and quantum statistics dictate the distribution. For bosons, there is a symmetry requirement of the wavefunction and they follow the Bose-Einstein distribution

$$f(\epsilon_\nu) = \frac{1}{e^{(\epsilon_\nu - \mu)/k_B T} - 1}. \tag{2.2}$$

This has the unique property that if the temperature is lowered below the so-called critical temperature, T_c, a macroscopic number of atoms occupy the ground state of the system even in the thermodynamic limit. This is also called Bose-Einstein condensation of the atoms and signals a phase transition in the system. In the case of an external confining 3D harmonic potential, the fraction of condensed atoms N_0 relative to the total atom number N is given by

$$\frac{N_0}{N} = \left[1 - \left(\frac{T}{T_c}\right)^3\right]. \tag{2.3}$$

This formula provides a simple method for evaluating the condensed fraction that remains experimentally relevant, although it does not take into account the interactions between the atoms, as well as a finite atom number, both of which modify the critical temperature [82, 83].

2.2 Interactions between Ultracold Atoms

Including interactions in a many-body system is generally complicated, but by utilizing the low-temperature property of the BEC, it is simplified considerably. For the case of two distinguishable particles interacting through a spherically symmetric potential, the total cross section is dominated by the lowest partial wave contribution, also known as s-wave scattering. This result is valid in the low-temperature limit, for which the total cross section is given by

$$\sigma = 4\pi a^2. \tag{2.4}$$

This only depends on the scattering length, a, which is interpreted as the distance at which two atoms "see" each other. For ultracold dilute gases, the interparticle distances are much greater than the typical length scale of the interaction. This means that the many-body interactions are effectively described by the simple two-body model. The interactions are formally included through an effective contact potential

$$U_{\text{eff}}(\mathbf{r}_i, \mathbf{r}_j) = \frac{4\pi\hbar^2 a}{m}\delta\left(\mathbf{r}_i - \mathbf{r}_j\right) = U_0\delta\left(\mathbf{r}_i - \mathbf{r}_j\right), \tag{2.5}$$

where m is the mass of the atoms and δ is the Dirac delta function. This contact potential is then included in the Hamiltonian for the system

$$H = \sum_{i=1}^{N}\left(-\frac{\hbar^2}{2m}\frac{\partial^2}{\partial \mathbf{r}_i^2} + V(\mathbf{r}_i)\right) + \sum_{i<j} U_0\delta(\mathbf{r}_i - \mathbf{r}_j), \tag{2.6}$$

where V is the external potential and a temperature at $T = 0$ is assumed such that all atoms are in the condensate. Using a Hartree-Fock approximation, the above Hamiltonian leads to the celebrated Gross-Pitaevskii equation

$$-\frac{\hbar^2}{2m}\nabla^2\psi(\mathbf{r}) + V(\mathbf{r})\psi(\mathbf{r}) + U_0|\psi(\mathbf{r})|^2\psi(\mathbf{r}) = \mu\psi(\mathbf{r}), \tag{2.7}$$

where ψ is the wavefunction of the condensed state and μ is the chemical potential. It resembles that of the Schrödinger equation, but includes a nonlinear term taking the interactions between the bosons into account and also has the chemical potential replacing the energy. The wavefunction is also conveniently related to the atomic density of the condensate through the relations

$$N = \int_V |\psi(\mathbf{r})|^2, \qquad n(\mathbf{r}) = |\psi(\mathbf{r})|^2. \tag{2.8}$$

For attractive interactions ($a < 0$), the condensate is unstable and can lead to a collapse of the system, which has been experimentally observed [84]. Repulsive interactions ($a > 0$) are therefore necessary to stabilize the system. In this case and for large atom numbers, the kinetic energy term of Eq. (2.7) may be neglected. This is the so-called Thomas-Fermi approximation and provides a direct solution for the density

$$n(\mathbf{r}) = |\psi(\mathbf{r})|^2 = \frac{\mu - V(\mathbf{r})}{U_0}. \tag{2.9}$$

In the case of an external harmonic potential, this has the shape of an inverted parabola and the spatial extent of the condensate is given by

$$R_i^2 = \frac{2\mu}{m\omega_i^2}, \qquad i = x, y, z \tag{2.10}$$

where the trap frequencies are given by ω_i. Although the results above are derived for a zero-temperature system, they are still relevant and applicable when working with finite temperatures in the laboratory.

2.2.1 Feshbach Resonances

The interactions between atoms are tunable through the scattering length by using so-called *Feshbach resonances* [24]. These resonances appear due to the coupling between an open and closed scattering channel. Two particles initially in an open channel may scatter to a bound state in a closed channel and then subsequently back to an open channel. By tuning the magnetic field, the total energy in the open channel is matched to the energy of the bound state in the closed channel. The effect is that the scattering length dramatically increases around this point. An empirical formula

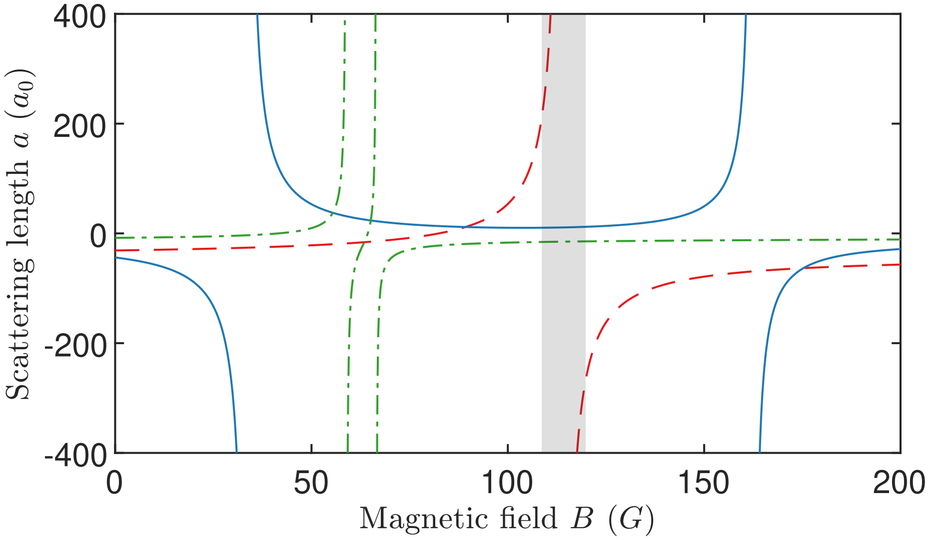

FIGURE 2.1: Magnetic Feshbach resonances of ^{39}K for selected states of the F = 1 manifold. The intrastate scattering length between atoms in the $|F=1, mF=-1\rangle$ state (blue line) and between the atoms in the $|F=1, mF=0\rangle$ state (green line) are shown. The interstate scattering length between atoms in the $|F=1, mF=-1\rangle$ and $|F=1, mF=0\rangle$ states is also shown (red line). A resonance is observed around 114 G (gray area), which allows for tuning between these two states.

for the scattering length provides the inclusion of these resonances as a function of the magnetic field B

$$a(B) = a_{bg}\left(1 - \frac{\Delta B}{B - B_0}\right), \tag{2.11}$$

where a_{bg} is the background scattering length between the resonances, B_0 is the magnetic field at a Feshbach resonance and ΔB is its associated width.

The Feshbach resonance structure can differ considerably between atomic species, but in the case of ^{39}K it is particularly rich. The resonance utilized in the experiments in this thesis is for the interstate scattering between the $|F=1,m_F=-1\rangle$ and $|F=1,m_F=0\rangle$ states. This resonance is located at 114G as shown in Fig. 2.1, where the internal scattering for each state is also plotted. Noticeably, it is a quite broad resonance, with a tunable region for both positive and negative scattering lengths. Additionally, in this region the internal scattering for the $|F=1,m_F=-1\rangle$ state is repulsive and essentially constant. As will be apparent later, this Feshbach resonance is an excellent candidate for exploring impurity physics with the $|F=1,m_F=-1\rangle$ and $|F=1,m_F=0\rangle$ states acting as medium and impurity, respectively.

2.3 Three-body Recombination

For the interactions described above, the scattering is usually elastic, but certain processes exist that lead to the permanent loss of otherwise trapped atoms. A prime example of this is three-body recombination, where three atoms collide, with two forming a bound molecule and the third atom receiving the remaining kinetic energy. The result is that all three atoms are lost from the trap. This process can be included in the, now time-dependent, Gross-Pitaevskii equation by the addition of an empirical imaginary term,

$$\begin{aligned} i\hbar\frac{\partial\Psi(\mathbf{r},t)}{\partial t} = \Bigg(&-\frac{\hbar^2}{2m}\nabla^2 + V(\mathbf{r}) + U_0\left|\Psi(\mathbf{r},t)\right|^2 \\ &-i\hbar\frac{L_3}{2}\left|\Psi(\mathbf{r},t)\right|^4\Bigg)\Psi(\mathbf{r},t), \end{aligned} \tag{2.12}$$

where L_3 is the three-body loss rate coefficient [85]. The local loss introduced by this term is proportional to the cube of the atomic density,

$$\frac{dn}{dt} = -L_3 n^3. \tag{2.13}$$

Given the high densities in the BEC, the loss introduced by Eq. (2.13) can have dramatic effects on experiments, which are often unwanted. However, the three-body recombination is also of fundamental interest in itself, as a method for pinpointing Feshbach resonances [24] and as an observable for Efimov physics [73, 74]. The latter of these consists of three-body bound states that appear as resonances in the three-body loss rate when tuning the interaction between the atoms. Investigations have shown that the three-body loss rate coefficient has a universal behavior given by

$$L_3 = C\frac{n_l a^4 \hbar}{m}, \tag{2.14}$$

where n_l is the number of atoms in the collision, usually set to 3, and C is a dimensionless constant depending on the sign of the scattering length, as well as the system in question [74, 86].

Another loss process to consider is two-body collisions with spin exchange where the atoms gain enough kinetic energy to escape the trapping potential and are lost. However, for the two states considered above, $|F=1, m_F=-1\rangle$ and $|F=1, m_F=0\rangle$, only three-body recombination is possible, due to angular momentum conservation. Two-body collisions therefore require atoms both in the $|F=1, m_F=-1\rangle$ and $|F=1, m_F=+1\rangle$ state, which is specifically utilized for the experiments presented later in this thesis.

2.4 Polaron Physics

The concept of the polaron originated in condensed matter physics but has been extensively investigated for ultracold quantum gases in the last $15-20$ years due to the high degree of control featured in these systems.

For historical context, a brief overview of the original work in condensed matter physics is first provided before turning to ultracold quantum gases.

2.4.1 Polarons in Condensed Matter Physics

The efforts in condensed matter physics to describe the behavior of an electron moving in a crystal lattice spans well over 90 years, beginning with the seminal work of Lev Landau and Solomon Pekar [87, 88]. In their work, the negatively charged electron ionizes the atoms in the lattice leading to phonon excitations and a resulting electron-phonon interaction (EPI). For a free electron moving in a continuous polarizable medium, the interaction with the lattice is encapsulated in an increased effective mass of the electron [43]. The increased mass of the electron merited its description as a new quasiparticle, the *polaron*.

Following this, a quantum mechanical treatment through second quantization of the EPI was proposed by Herbert Frölich [89]. For weak coupling between the electron and phonons, characterized by a dimensionless constant α, perturbation theory [90] gives an expression for the second order energy of the electron at momentum $\mathbf{k}$,

$$E_{\mathbf{k}} \simeq -\alpha\omega_0 + \frac{k^2}{2m^*}. \tag{2.15}$$

The first term gives the polaron binding energy E_P, and the second term contains the effective mass of the electron, given by $m^* \simeq m(1+\alpha/6)$. The increased mass is due to the electron dragging the phonon cloud around as it moves. For a polaron at rest, $\mathbf{k}=0$, the number of virtual phonons in the cloud is given by $N_{ph} = \alpha/2$, directly linking it to the coupling constant, which is interpreted as the "thickness" of the phonon cloud [90].

The above result shows that the properties of the electron, i.e. its energy and mass, are modified through the interactions with the phonon cloud. For an impurity immersed in an ultracold quantum gas, the same formalism applies and a similar behavior can be expected, which is discussed in the following.

2.4.2 Polarons in Ultracold Quantum Gases

In ultracold quantum gases, interactions between atoms are characterized by the scattering length, which is tunable through the use of Feshbach resonances as described in Sec. 2.2. For an impurity in such a gas, these interactions lead to a dressing of the impurity much like the case of the electron in the crystal lattice, and the polaron framework applies.

Extensive theoretical efforts have been made for the description of an impurity embedded in ultracold quantum gases, with a recent overview in Ref. [91]. In the case of ultracold Fermi gases, the fermionic nature of the medium separates it from the bosonic behavior of the phonon cloud in condensed matter physics. Nonetheless, it is a powerful platform for investigating impurity physics in the context of Landau's theory of Fermi liquids [92] as well as the Kondo effect [93]. For Bose-Einstein condensates, the system more closely resembles condensed matter physics given the bosonic nature of the BEC and phonon cloud. The resulting Bose polaron has distinct quasiparticle properties that are examined in the following. Note that the terms boson and medium are used interchangeably and refer to the atoms of the BEC. Expanding on the results of Frölich, the Hamiltonian describing the interactions between the impurity and bosons is given by

$$\begin{aligned} H =& \sum_{\mathbf{k}} \epsilon^{B}_{\mathbf{k}} a^{\dagger}_{\mathbf{k}} a_{\mathbf{k}} + \frac{1}{2V} \sum_{\mathbf{k}\mathbf{k}'\mathbf{q}} V_B(q) a^{\dagger}_{\mathbf{k}+\mathbf{q}} a^{\dagger}_{\mathbf{k}'-\mathbf{q}} a_{\mathbf{k}'} a_{\mathbf{k}} \\ &+ \sum_{\mathbf{k}} \epsilon^{I}_{\mathbf{k}} c^{\dagger}_{\mathbf{k}} c_{\mathbf{k}} + \frac{1}{V} \sum_{\mathbf{k}\mathbf{k}'\mathbf{q}} V_I(q) c^{\dagger}_{\mathbf{k}+\mathbf{q}} a^{\dagger}_{\mathbf{k}-\mathbf{q}'} a'_{\mathbf{k}} c_{\mathbf{k}}, \end{aligned} \tag{2.16}$$

with creation operators $c^{\dagger}_{\mathbf{k}}$ and $a^{\dagger}_{\mathbf{k}}$ for the impurity and boson, the free dispersions $\epsilon^{B,I}_{\mathbf{k}} = \frac{\hbar^2 k^2}{2m_{B,I}}$ and system volume V [94]. The coupling constants for medium-medium and impurity-medium interactions are given by $V_B(q)$ and $V_I(q)$, respectively. The former of these is assumed to be weak and described by Bogoliubov theory. The latter is determined through the impurity-medium scattering length, a, which can be both negative and positive, leading to attractive and repulsive interactions, respectively.

For weak impurity-medium coupling, perturbation theory provides exact results for the quasiparticle properties at zero temperature [94–96]. In this limit, the polaron is well-defined for attractive and repulsive interactions. The impurity energy is given by a mean-field energy shift through the interactions with the medium, with corrections in higher powers of the scattering length [94]. The so-called quasiparticle residue Z_P provides a measure of its quasiparticle nature, much comparable to that of the effective mass discussed earlier. It is given by the squared overlap between the wavefunctions of the polaron and the non-interacting bare impurity, $Z_\text{P} = \left|\left\langle \psi_0 \middle| \psi_\text{pol} \right\rangle\right|^2$. As the interaction is increased the residue decreases, signaling that a larger part of the polaron lies in the medium excitations.

For the case of strong coupling, an exact analytical solution does not exist, and instead, approximations are utilized. These include variational [51, 54, 97, 98] and diagrammatic methods [57, 99, 100] as well as quantum Monte-Carlo (QMC) calculations [53, 101, 102]. This last method provides numerical exact solutions, which can include all relevant interactions and correlations, but is computationally expensive.

Attractive interactions

The main results for an intuitive variational method in Ref. [54] for attractive impurity-medium interactions are first briefly presented. These results are completely consistent with those from the diagrammatic method [53], and the two are used interchangeably throughout this thesis. The variational ansatz was first developed for the description of the Fermi polaron [103] before being extended to the Bose polaron. The wavefunction

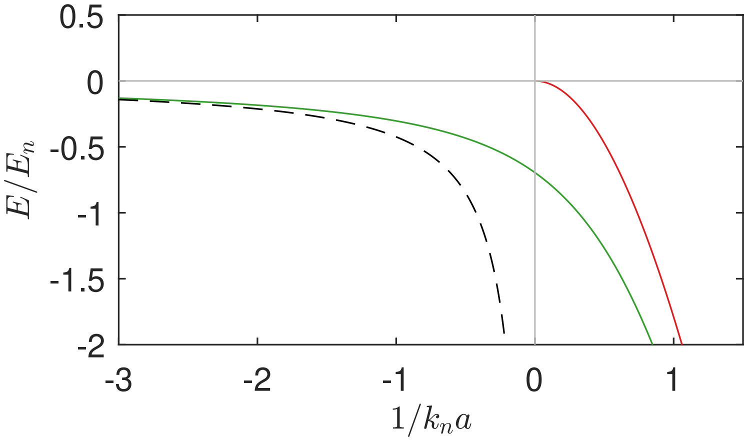

FIGURE 2.2: Energy of the attractive polaron state (green line) as a function of inverse interaction strength $1/k_n a$. This state converges with the molecular state (red line) on the repulsive side. The mean-field energy is also plotted for comparison (black dashed line).

consists of a superposition of an impurity at rest, $|\mathbf{0}\rangle_I$, and scattering with a boson into the momentum state, **-k**,

$$|\Psi\rangle = \phi_0 \, |\mathbf{0}\rangle_I \otimes |\mathrm{BEC}\rangle + \sqrt{N_B} \sum_{\mathbf{k}} \phi_{\mathbf{k}} a^{\dagger}_{\mathbf{k}} \, |{-\mathbf{k}}\rangle_I \otimes |\mathrm{BEC}\rangle \,. \tag{2.17}$$

The variational parameters are given by ϕ_0 and $\phi_{\mathbf{k}}$ and the condensate is described by a coherent state $|\mathrm{BEC}\rangle$, with the average boson number N_B. This ansatz is used to calculate the expectation value of the kinetic and potential energy from the Hamiltonian in Eq. (2.16). Minimization of the total energy gives the relation for the polaron energy as

$$E_\mathrm{P} \equiv \frac{\hbar^2 \kappa^2}{2m} = -\frac{E_\mathrm{mf}}{1 - \kappa a}, \tag{2.18}$$

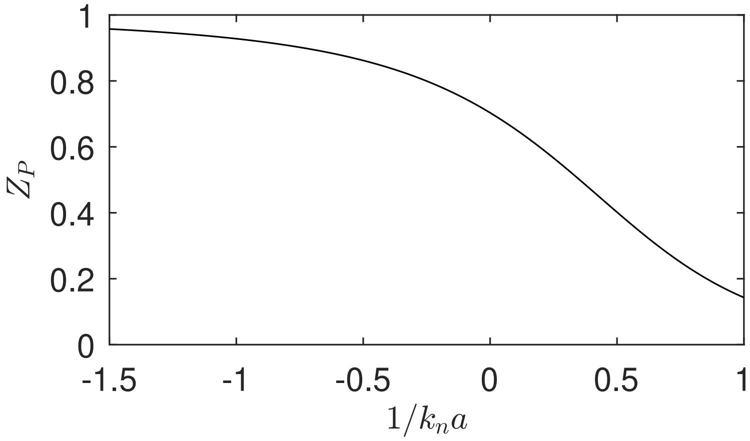

FIGURE 2.3: Quasiparticle residue Z_P of the attractive polaron state as a function of the inverse interaction strength, $1/k_n a$.

with the mean field energy, $E_\mathrm{mf} = \frac{2\pi\hbar^2 na}{m_r}$, atomic density of the BEC, n, and reduced mass of the boson and impurity, m_r. This equation is solved by expressing the parameter κ through the interaction strength of the system $k_n a$, where $k_n = (6\pi^2 n)^{1/3}$ is the characteristic wavenumber of the medium and a is the impurity-medium scattering length. The polaron energy is scaled by the characteristic energy of the medium, $E_n = \frac{\hbar^2 k_n^2}{2m}$, and is shown in Fig. 2.2, as a function of the inverse interaction strength $1/k_n a$. The polaron energy agrees with the mean-field prediction for low interaction strengths but is observed to cross unitarity at $1/k_n a = 0$, in contrast to the mean field result which diverges. The attractive polaron eventually converges with the molecular branch on the repulsive side.

From the above variational method, the quasiparticle residue for the attractive polaron can also be calculated as

$$Z_{\mathrm{P}} = \frac{1}{1 + \frac{3\pi}{8\sqrt{2}} \left| \frac{E_{\mathrm{P}}}{E_n} \right|^{3/2}}, \tag{2.19}$$

which only depends on the scaled polaron energy, E_{P}/E_n. The residue is plotted as a function of the inverse interaction strength in Fig. 2.3.

The energy and residue are essential for describing the spectral response of the polaron from radiofrequency (rf) spectroscopy [53, 54]. This experimental technique is further considered later in this thesis.

Repulsive interactions

For repulsive impurity-medium interactions, two distinct polaron states exist as shown in Fig 2.4. One is the attractive polaron state crossing unitarity and converging with the molecular state. The other is the repulsive polaron state, which becomes increasingly ill-defined when approaching strong interactions. This is due to both a many-body dephasing effect as well as the possibility of decaying to the lower-lying attractive branch [91, 104]. Generally, a theoretical investigation of the repulsive polaron behavior is challenging, and different methods give inconsistent results when approaching strong interactions. This is also highlighted in Fig. 2.4, where different calculations for the energy of the repulsive Bose polaron state are plotted as a function of the inverse interaction strength. For low interaction strength, all calculations agree with the mean-field prediction, but as strong interactions are approached, the discrepancies between the theories become apparent. Additionally, the energy separation of the attractive and repulsive polaron states is small at strong interactions but gets significantly larger at low interaction strengths. Recently, a theoretical prediction for the existence of metastable states between these two branches was made, adding to the complexity of theoretical predictions for this system [105].

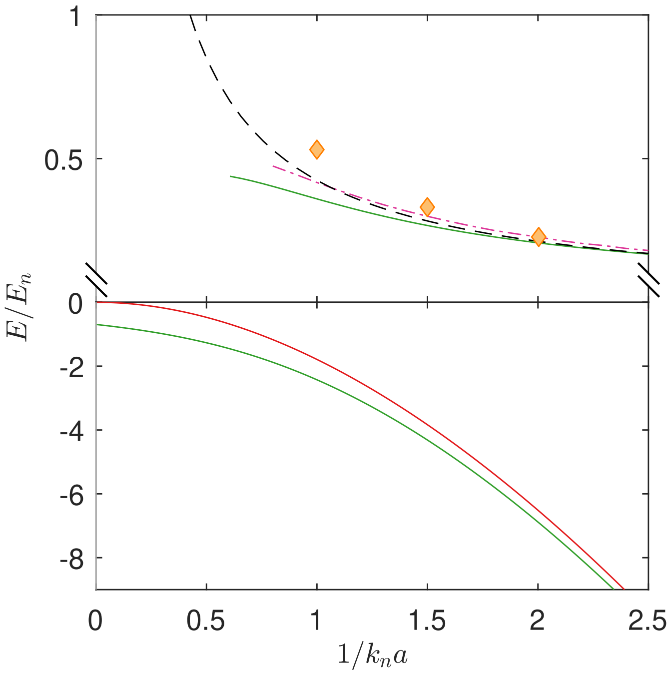

FIGURE 2.4: The energy of the repulsive and attractive polaron branches as a function of inverse interaction strength calculated from a diagrammatic prediction (green lines) [2]. A truncated basis method (magenta line) [53] and a Quantum Monte-Carlo simulation (yellow diamonds) [53] are also shown. The mean field result (black dashed line) and molecular state (red line) are plotted for comparison. Adapted from Ref. [2].

Strongly interacting regime

Generally, the theoretical models predict a polaron state for both attractive and repulsive impurity-medium interactions, with the former crossing over to the repulsive side. Experimental evidence for this is found for both the Fermi polaron [45, 47, 49] as well as for the Bose polaron [51, 52, 106]. For the former, there is strong evidence that the quasiparticle picture holds at strong interactions [91, 107–109]. In the case of the Bose polaron, contemporary theories give different results for the behavior of the polaron at strong attractive interactions. These can be grouped into two scenarios. The first predicts a smooth crossover to the molecular state [53, 54, 97, 99] similar to that indicated in Fig. 2.2, with possible modifications in the presence of Efimov physics [79, 80]. The second scenario predicts a breakdown and collapse of the attractive polaron [67, 110–112]. Therefore, experiments must resolve these theoretical discrepancies, along with those presented for repulsive interactions in Fig. 2.4.

For the case of attractive interactions, the experimental investigations at strong interactions are presented in Ch. 5, using a spectroscopic technique. For repulsive interactions, the system is probed using an interferometric sequence, as presented in Ch. 6.

2.4.3 Mediated Interactions

So far, only a single impurity interacting with the medium has been considered. For the case of two impurities, an induced interaction mediated by the medium can lead to a bound state termed the *bipolaron*. Bipolarons are of fundamental interest, as they have been suggested as the mechanism behind organic magnetoresistance [66], high-temperature superconductivity [63, 113] and even as a model for quantum dots [114]. For the case of a Bose-Einstein Condensate, the effective interaction between the impurities is expected to be more pronounced compared to a Fermi gas, due to the higher compressibility of the BEC [115].

Theoretical investigations of these mediated interactions between two impurities in a BEC have predicted the existence of a bipolaron state [58, 116]. In Ref. [58], the binding energy of the bipolaron state was calculated using a diagrammatic method, which was compared to quantum Monte-Carlo simulations. The ground state energies of the system containing one and two impurities were calculated and given by $E_1 = E_\mathrm{P}$ and

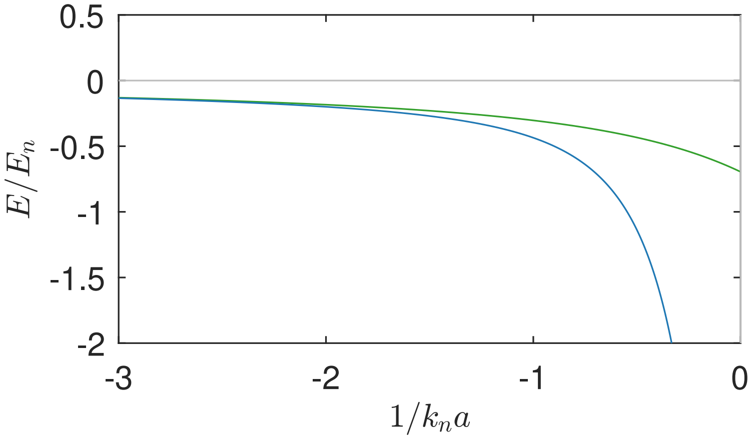

FIGURE 2.5: Energy of the attractive polaron branch (green line) and the bipolaron state (blue line) as a function of the inverse interaction strength, $1/k_na$.

E_2, respectively. The binding energy of the bipolaron was then calculated as $E_{\mathrm{BP}} = E_2 - 2E_{\mathrm{P}}$. At low impurity-medium interaction strengths, the binding energy of the bipolaron is small and the system consists of two independent polarons. The energy of the bipolaron is calculated as the sum of the binding energy and that of a single polaron as shown in Fig. 2.5 as a function of the inverse interaction strength. This interpretation connects the theory to the experiment, where rf-spectroscopy can disassociate the bipolaron and probe a single polaron, which is further discussed in Ch. 5. Importantly, it is only in the strongly interacting regime that large deviations from the polaron are observed, which is necessary for experimental observations.

As discussed previously, multiple theories predict the collapse of the attractive polaron at strong interaction strengths. The existence of the bipolaron is not consistent with these theories but is another intriguing theoretical prediction for the strongly interacting attractive regime.

CHAPTER 3

Experimental Cooling and Detection Techniques

The experimental apparatus was initially built in Hannover [117, 118], focusing on experiments with ^{87}Rb [119, 120]. In 2011, the experiment was moved to Aarhus University and was reconfigured to produce mixtures of ^{39}K $-^{87}$Rb with the possibility of ^{41}K$-^{87}$Rb mixtures as well [121, 122]. Since then, the overall structure of the experiment has remained the same, but with several modifications from the contributions of later PhD students [123, 124]. Additionally, the experimental focus has been on impurity physics for multiple PhD generations by now [44, 123], which means that only small modifications were necessary on my part.

This chapter provides a brief overview of the experiment, starting from the initial trapping and cooling of the atoms in Sec. 3.1 until condensation of the system is achieved as presented in Sec. 3.2. Additionally, the absorption imaging technique used for the detection of the atoms is discussed in Sec. 3.3, along with the necessary calibrations. Finally, some of the modifications to the apparatus during my PhD are mentioned in Sec. 3.4.

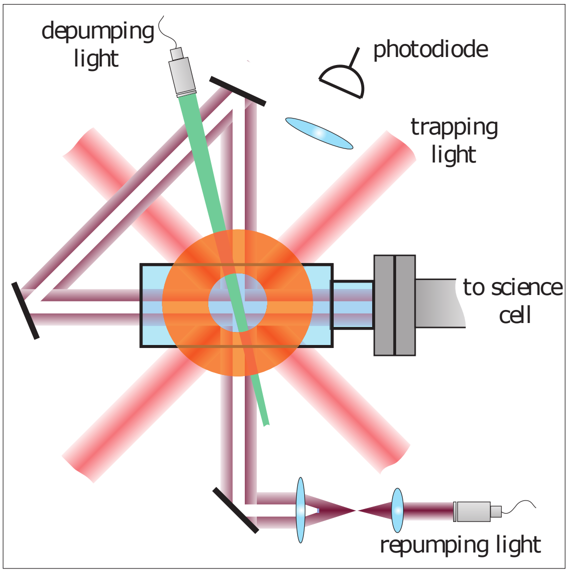

FIGURE 3.1: Overview of the Magneto-Optical-Trap employed in the experiment. A dark-SPOT for the repumping light and a depumping beam are utilized to prevent collisions between ^{39}K and ^{87}Rb atoms. Adapted from [125].

3.1 Dual-species MOT

The experiment was designed to investigate multiple atomic species. This was realized in 2014, with the observation of Bose-Einstein Condensates of both ^{39}K and ^{87}Rb [125]. However, in the current status of the experiment, the rubidium is sacrificed to maximize the potassium BEC, which is then used exclusively for the experiments.

The rubidium and potassium atoms are initially trapped and cooled in a Magneto-Optical-Trap (MOT), with an overview in Fig. 3.1. This is achieved by using the D_2 lines at 780 nm and 767 nm for rubidium and potassium [126], with energy levels shown in Fig. 3.2. A cooling beam for

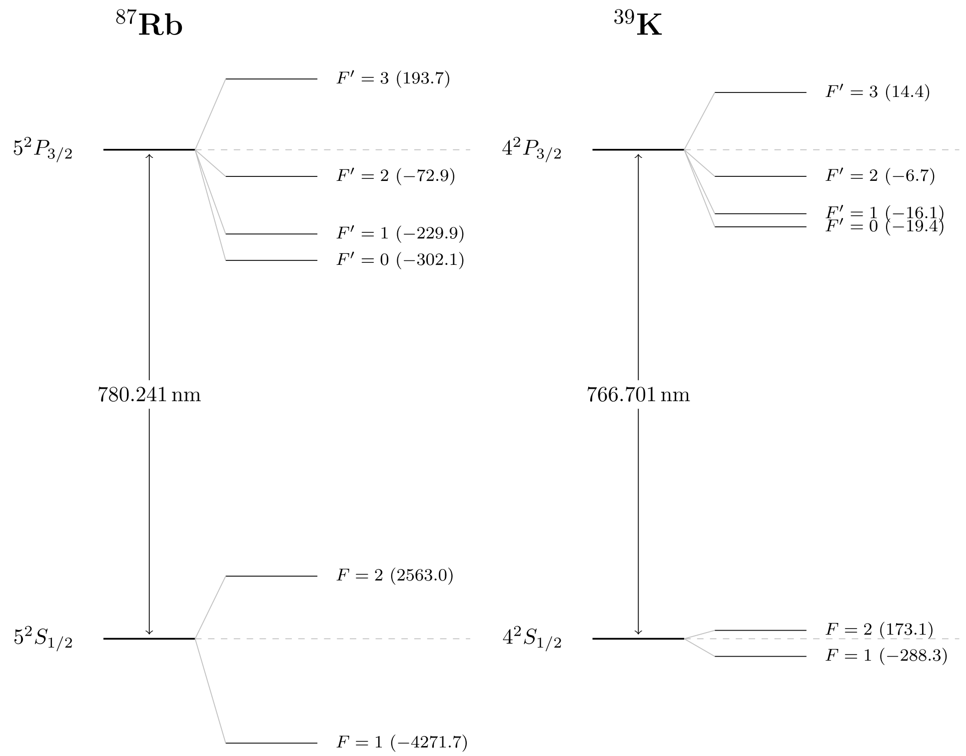

FIGURE 3.2: The relevant hyperfine states of ^{39}K and ^{87}Rb for the D_2 line, used for the cooling and trapping schemes. The parentheses show the relative detuning of the hyperfine states in MHz. Adapted from [126].

the $|F = 2\rangle$ to $|F' = 3\rangle$ transition and a repumping beam for the $|F = 1\rangle$ to $|F' = 2\rangle$ transition are used. Here, F and F' correspond to the ground and excited hyperfine states as in Fig. 3.2. Potassium has a small energy splitting of the excited hyperfine levels compared to rubidium and its maximum potential in the MOT is more limited. Furthermore, hyperfine-changing and light-assisted collisions [127, 128] act to further decrease the potassium atom numbers, with relatively little effect on the much larger rubidium sample. For these reasons, a so-called dark-SPOT of the repumping light for rubidium is employed at the MOT center. This forces the rubidium at the center into the dark state $|F=1\rangle$ and prevents the above-mentioned collisions. Additionally, a depumping beam enhances this effect by actively pumping the rubidium atoms at the center directly into the dark state. These two techniques allow for maximal accumulation of potassium atoms in the MOT, while still retaining a sufficiently high number of rubidium atoms [125].

The MOT phase lasts for 25 seconds and is followed by optical molasses for both atomic species. For the case of ^{39}K this is again more complicated due to the small excited hyperfine state splitting. However, by using specific detuning and intensity protocols for the cooling and repumping light, an effective sub-Doppler cooling regime can be identified [129]. After this, all the atoms are optically pumped into the magnetically trappable state $|F=2, m_F=2\rangle$, and are afterward transported to the so-called science cell, which features a higher vacuum. The transport is accomplished by ramping the magnetic field of the MOT and physically moving the coils, which are attached to a mechanical sleigh. A new pair of coils at the science cell are then used for transferring from the MOT. After the MOT and molasses phases, the atom numbers of ^{87}Rb and ^{39}K are 2.7×10^9 and 7×10^7 with temperatures of 35 µK and 117 µK, respectively. At the science cell, the trapped potassium and rubidium atoms are now ready for the next cooling stage, which is evaporative cooling.

3.2 Evaporative Cooling

The rubidium atoms are selectively evaporated using microwave radiation, to sympathetically cool the potassium sample. To avoid Majorana spin flips at the center of the trap, a Ioffe coil is introduced to the quadrupole trap, creating a harmonic potential with an offset at the minimum [130]. The evaporation is then performed until the rubidium sample is depleted. The remaining potassium atoms are then transferred into a 1064 nm crossed optical dipole trap (ODT), to free up the magnetic field as a tunable parameter. Two Rapid Adiabatic Passages (RAP) are utilized to first transfer the atoms from the $|F = 2, m_F = 2\rangle$ state to the $|F = 2, m_F = -2\rangle$ state and then to the $|F = 1, m_F = -1\rangle$ state. The atoms have a negative background scattering length at low magnetic fields [131], and it is necessary to tune it to large positive values, with the magnetic field, before evaporative cooling is performed. This allows for the condensation of the atoms, and this is the starting point for the experiments discussed within this thesis. To detect the atoms, the trapping potential is turned off and the cloud falls and expands during a time-of-flight (TOF), with subsequent absorption imaging.

3.3 Absorption Imaging

Absorption imaging uses an imaging beam incident on the atomic cloud which becomes attenuated due to absorption. For multi-level atoms, this is described by the Beer-Lambert law [132]

$$\frac{dI}{dx} = -n(x)\frac{\sigma_0}{\alpha^*}\frac{1}{1 + I/I_{\text{sat}}^{\text{eff}}}I, \tag{3.1}$$

where $\sigma_0 = 3\lambda_0^2/2\pi$ is the resonant scattering cross section for a two-level atom with a transition at the wavelength λ_0. The atomic density along the imaging beam is given by $n(x)$. Finally, $I_{\text{sat}}^{\text{eff}} = \alpha^* I_{\text{sat}}$ is an effective saturation intensity given by the product of the saturation intensity, which for our system is the D2 line for ^{39}K, $I_{\text{sat}} = 1.75$ mW/cm^2 [133], and the dimensionless parameter α^*. This parameter takes experimental factors into account such as imperfect polarization and multi-level structure, and is used for calibrating the imaging system.

The absorption of the imaging beam effectively results in a "hole" in its intensity profile $I(y,z)$, which is recorded on a camera for each pixel (y,z).

This is then compared to the case of a reference beam $I_0(y,z)$, without the absorption of the cloud. This allows for the extraction of the column density $\tilde{n}(y,z)$ and optical density $od(y,z)$ of the atomic cloud, which are found by integrating Eq. (3.1) along the imaging direction,

$$od(y,z) \equiv \tilde{n}(y,z)\sigma_0 = \alpha^* \ln\left(\frac{I_0(y,z)}{I(y,z)}\right) + \frac{I_0(y,z) - I(y,z)}{I_{\text{sat}}}. \tag{3.2}$$

The role of the parameter α^* is to ensure that the observed column density of the atomic cloud does not depend on the intensity of the imaging beam. To calibrate the experimental value of α^*, the intensity of the imaging beam is varied for atomic clouds of constant optical densities while keeping the number of photons in the imaging beam constant by adjusting the exposure time. For a chosen region of interest (ROI) on the camera, the intensities $I(y,z)$ and $I_0(y,z)$ are extracted for each pixel. This gives the following fitting function for α^* [134]

$$\sum_{\text{ROI}} \tilde{n}(y,z)\sigma_0 = \alpha^* \sum_{\text{ROI}} \ln\left(\frac{I_0(y,z)}{I(y,z)}\right) + \sum_{\text{ROI}} \frac{I_0(y,z) - I(y,z)}{I_{\text{sat}}}. \tag{3.3}$$

An example of such a calibration is shown in Fig. 3.3, along with the effect of varying this parameter on the standard deviation of the optical densities of the atomic clouds for the different intensities. The minimum lies at the same value as that extracted from the fit, $\alpha^* = 1.64(8)$.

The camera itself also requires calibrations consisting of pixel size calibration and photon calibration. The first is necessary due to the optical elements used in the imaging setup, resulting in an effective pixel size. It is performed by letting the atoms fall under the effect of gravity, for which they are accelerated by 9.815 m/s^2. The atoms vertical position on the camera is given by a quadratic equation, $f(t) = at^2 + bt + c$, as a function of TOF. This is shown in Fig. 3.4, where the pixel size is extracted as

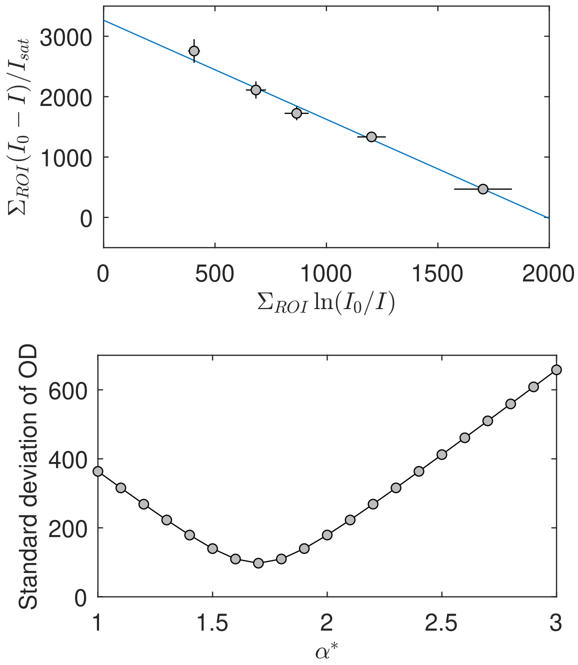

FIGURE 3.3: (top) The relation between the logarithmic and linear term of Eq. (3.3) allows for fitting of the parameter $\alpha^* = 1.64(8)$. (bottom) This value of α^* gives the lowest standard deviation of the optical density (OD) when varying the intensity of the imaging beam.

$$\text{pixel size} = \frac{9.815}{2a}\,\frac{\mu m}{\text{px}}. \tag{3.4}$$

From the fit to the data in Fig. 3.4, the pixel size is calculated to $2.85(1)\ \mu m/px$. The photon calibration of the camera relates the number of photon-electron counts recorded at the camera to the number of photons at the position of the atoms. First, the power in the imaging beam is measured before and after the science cell, and the average of these is taken as

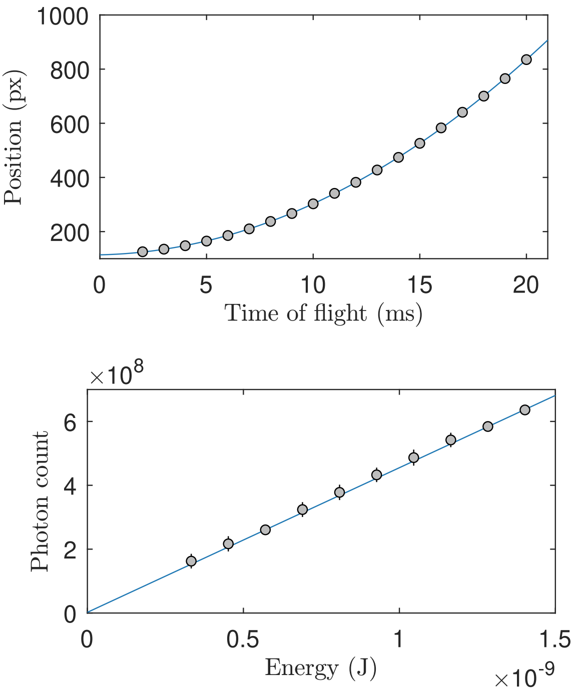

FIGURE 3.4: (top) Pixel size calibration, where the atoms fall under gravity and are fitted to a quadratic model (blue line), which allows for the extraction of the effective pixel size. (bottom) Photon calibration, relating the number of photons at the position of the atoms to those detected at the camera with a linear fit (blue line).

the power at the position of the atoms. The exposure time of the camera is then varied and the number of counts is plotted as a function of the energy in the imaging beam. This is shown in Fig. 3.4 and gives the value 2.21×10^{-18} J/count, or equivalently 0.0134 I_{sat} μs/count by using the pixel size and the units of I_{sat}. The imaging transition used for our experiment is the $|F = 2\rangle$ to $|F' = 3\rangle$ transition, along with repumping light from

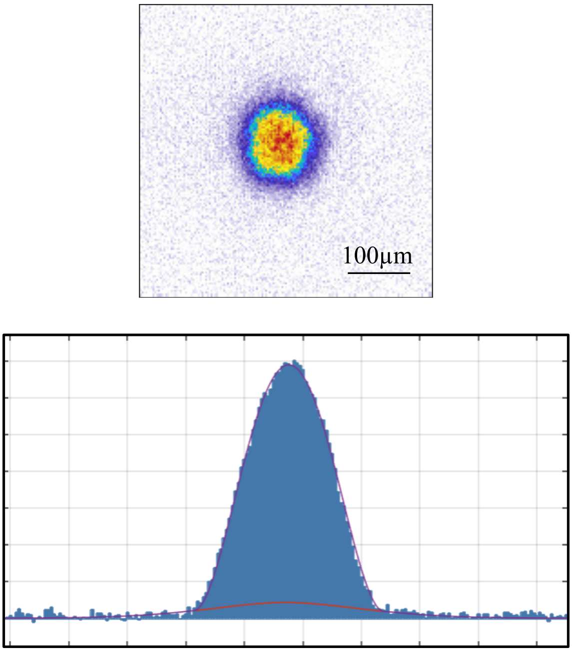

FIGURE 3.5: (top) Typical image of a ^{39}K BEC for our system, observed using absorption imaging after time-of-flight. Adapted from [44]. (bottom) The density profile of the cloud, with the bimodal fit for the thermal and condensate visible. Adapted from [124].

the $|F=1\rangle$ to $|F'=2\rangle$ state. A typical absorption image of a ^{39}K BEC is shown in Fig. 3.5, where the atom number is evaluated using a bimodal fit for the condensate and thermal parts of the cloud. The typical value of the number of atoms in the condensate is $50-60\times 10^3$. The total cycle time for the experiment from MOT to BEC is just over one minute and the experiment is often kept running overnight for data acquisition.

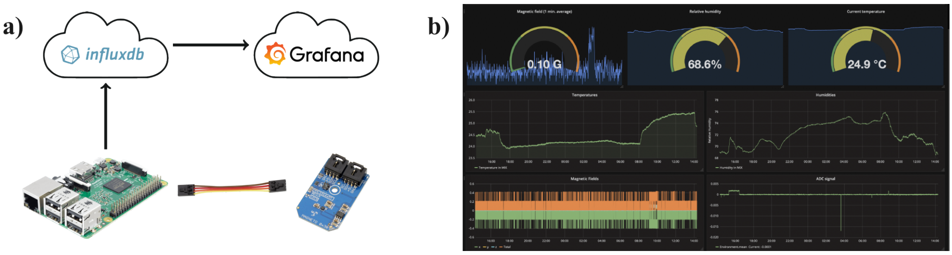

FIGURE 3.6: **a)** Overview of the sensor and communication to the Grafana database through the Raspberry Pi. **b)** Visualization of the sensor values uploaded to the Grafana database.

3.4 Modifications

In this section, selected contributions to the experiment during my PhD are highlighted. These include improvements and corrections to the already existing equipment as well as installations of new features.

Logging and monitoring

Given the long cycle time of the experiment, the experiment is often running for several hours to ensure a sufficient amount of data is collected. For the collected data to be consistent and comparable, the system must be as stable as possible to repeatedly produce equal-sized condensates. Multiple parameters can influence the stability of the system, such as the room temperature and humidity, as well as stray magnetic fields from neighboring laboratories. The last of these is controlled by measuring the magnetic field with the atoms daily, while also regularly nullifying external magnetic fields with passive compensation coils that surround the experiment. Additionally, the experiment is also locked to the same point in the 50 Hz cycle from the power grid right before magnetic field sensitive measurements are performed.

The laboratory itself is positioned underground and the temperature is controlled by a commercial cooling system. To control the humidity, a dehumidifier was purchased during my PhD, which attempts to keep the humidity at a steady level. In order to quantitatively measure how well these parameters are controlled, multiple sensors are placed around the laboratory. These employ I2C communication, which means that multiple sensors can be connected to a single Raspberry Pi by placing them in series. The data from the sensors are uploaded to the online database Grafana, as illustrated in Fig. 3.6, which allows for quick visualization of the trend of the parameters. Besides being useful for monitoring the environment, general analog-to-digital converter (ADC) modules find broad usages in the experiment. One example is monitoring the laser light out of specific optical fibers using a photodiode behind the first mirror after the fiber and connecting the photodiode to the ADC module. This allows for monitoring which fiber couplings are drifting overnight and logging this to check for systematic issues.

Tapered amplifier

Tapered amplifiers are widely used in the experiment to reach the necessary optical powers for the MOT cooling phase. Although commercially available, these have typically been homebuilt for our system. At the beginning of my PhD, I was tasked with building new tapered amplifiers (TA), according to the design in Ref. [135]. These differed from the old design, where everything was permanently glued together, by having a more structured design where the position of the in- and out-coupling lenses are freely varied. Initial testing of one of the TA's is shown in Fig. 3.7. Here, the amplification of the TA is given by the ratio of the output power and the input seed power, P_{out}/P_{seed}, and is observed to deliver large amplifications as the injection current is increased.

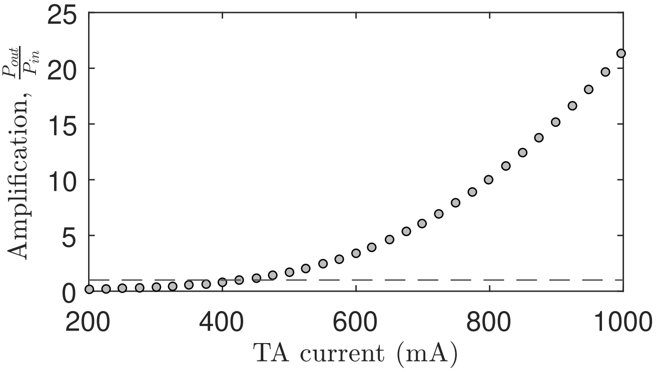

FIGURE 3.7: The amplification of the TA, P_{out}/P_{seed}, as a function of the injection current. The horizontal line marks the point where $P_{out} > P_{seed}$.

Imaging field

It is critical to have a well-defined magnetic field during the absorption imaging of the atoms. For this reason, it is good practice to cancel any background magnetic field, since they may interfere with the experiment when using low magnetic fields. The magnetic fields are therefore measured using a magnetic field sensor (Mag-03 from Barington) and the required field strengths of the coils are calculated. Three compensation coil pairs surround the science cell, where the coils in the Y- and Z-direction only cancel background fields.

The X-direction coils also cancel background fields but during the imaging sequence, they are ramped to higher currents to provide a guidance field. However, due to the slow GPIB communication there is a significant delay in the ramp as shown in Fig. 3.8. This means that the guiding field for the imaging sequence is not set until about 15 ms after the trigger has been issued by the control program. The situation is drastically improved by using a controllable MOSFET between the power supply (PSU) and the

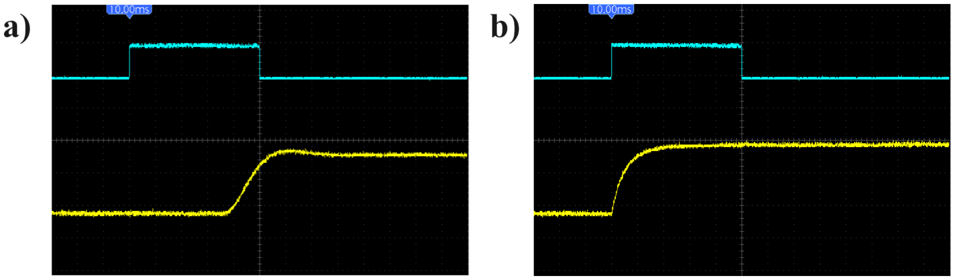

FIGURE 3.8: Response time for imaging field from trigger (blue line) to actual measured current (yellow line) through the compensation coils for **a)** GPIB command and **b)** MOSFET trigger.

coils. The PSU is set to high values much earlier but has its output blocked by the MOSFET. The field is then set with a digital trigger to the MOSFET, which has a much better response time, ~ 4 ms, as also seen in Fig. 3.8. This leads to a more predictable behavior for this part of the experimental sequence.

Future plans

Finally, plans for the experimental apparatus are mentioned here. These include rebuilding the laser system into modular components, to improve the stability and accessibility of the system. For the potassium laser system, there are currently three external-cavity diode lasers from Toptica in use, which often require attention to ensure adequate output power as well as sufficient single-mode lasing. For the redesign of the system, only one or two potassium lasers will be used, and additional TA's will be installed to ensure enough output power is achieved. This is possible since ^{39}K has a very small hyperfine splitting between its ground states, such that both can be addressed by shifting the frequency with AOM's.

As mentioned earlier, the cycle of the system from MOT to BEC is just over one minute. If this cycle time could be reduced it would be a significant improvement to the experiment, since the criteria for stability would be relaxed. Ideas for how to do this include immediate loading of the MOT after the atoms have been transferred to the science cell or implementing a 2D-MOT in connection with our 3D-MOT for fast and efficient loading. The former of these has already been tested and concluded to not be possible due to the science cell not being shielded well enough from the MOT light. Implementing a 2D-MOT in connection with our 3D-MOT is therefore a promising candidate that could remove the need for rubidium as Gray molasses has been shown to be an efficient cooling method for potassium [136]. However, it would also be a major re-configuration of the system that would require a great deal of effort and time.

CHAPTER 4

Loss Spectroscopy and Three-body Physics

Radio-frequency (rf) spectroscopy is one of the fundamental probes for investigating ultracold quantum gases. The spectral response of the system consisting of an impurity immersed in a Bose-Einstein Condensate allows for extracting important properties of the emerging Bose polaron. However, it also contains information on the three-body physics that leads to losses in these systems. Characterizing these losses is important for experimental sequences where the system is evolving and allows for tracking the atom number as a function of the evolution time. The atom number is central for benchmarking the system to properly compare the observed results with theoretical predictions.

The chapter is structured as follows: First, the spectral function of the polaron is discussed in Sec. 4.1. Afterward, the experimental spectroscopic techniques to probe this are provided in Sec. 4.2. The three-body recombination processes are described in Sec. 4.3, with a discussion of the specific details of our system. Finally, in Sec. 4.4, the results of the publication [3] are briefly summarized and an outlook is given before the full content is presented.

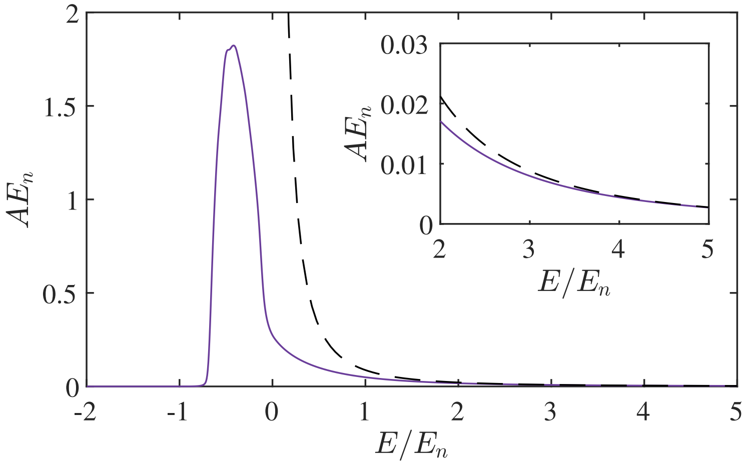

FIGURE 4.1: The polaron spectral function A (purple line), as a function of the energy of the rf-pulse, both scaled by the characteristic energy E_n (see main text). The energy of the rf-pulse is measured relative to the bare energy of the non-interacting impurity. A comparison of the high-frequency tail and an exact analytical solution (black line) is also shown (inset). Adapted from [44].

4.1 Spectral Function

For an impurity immersed in a Bose-Einstein Condensate, the resulting polaron may be investigated with different experimental tools to probe its properties. One of these is spectroscopy, which probes the spectral response of the system. As discussed in Ch. 2, the polaron consists of an impurity dressed with excitations of the medium it interacts with. This was modeled as a superposition of the impurity at rest and moving with finite momentum with an excitation moving in the opposite direction. Therefore, the system's expected spectral response consists of a peak corresponding to the ground state of the polaron at rest and a tail stretching to higher energies corresponding to the continuum of excitations. This is illustrated in Fig. 4.1, where the polaron spectral function was numerically calculated using a diagrammatic prediction for attractive impurity-medium interactions [57]. The peak displays a clear shift towards negative energies, relative to the energy of the non-interacting bare impurity at $E/E_n = 0$. Additionally, the behavior of the high-frequency tail is compared to an exact analytical solution [137], with excellent agreement.

The observed shift of the peak of the polaron depends explicitly on the impurity-medium interaction strength, $k_n a$. This was described in Ch. 2, where a is the impurity-medium scattering length and $k_n = (6\pi^2 n)^{1/3}$ is the characteristic wavenumber of the medium with atomic density n. Additionally, the characteristic energy, $E_n = \hbar^2 k_n^2 / 2m$, also provides a convenient scaling parameter for the observed energy shift. This way of scaling the system is useful when comparing the results with other experiments and theoretical predictions, including those with a fermionic medium where similar scaling parameters are used [91]. Importantly, if the atomic density is not well known, it can lead to systematic errors between the observed and expected results. Accurately determining the density is therefore critical but non-trivial to calculate in the presence of losses. Experimental methods for probing the spectral function and its connection to the loss processes of the system are presented in the following section.

4.2 Spectroscopy Techniques

The experimental efforts to record the spectrum of the polaron led to the first observations of the Fermi polaron [45, 47] and Bose polaron [51, 52]. This was accomplished using the so-called *injection* protocol, which is a single rf-pulse sequence. This protocol is presented first followed by a more advanced two rf-pulse sequence.

4.2.1 Injection Spectroscopy

For our system [51], the experimental sequence for the injection protocol is as follows: The system starts with a ^{39}K BEC in the hyperfine state $|F=1, m_F=-1\rangle \equiv |1\rangle$, acting as the medium. A rf-pulse is applied, which effectively transfers a fraction of the BEC atoms to the impurity state, $|F=1, m_F=0\rangle \equiv |2\rangle$. This transfer only occurs if the rf-pulse is on resonance with respect to the impurity state. The energy of the impurity is dependent on the impurity-medium interaction strength, which is controlled through the scattering length, a, and tunable by use of a Feshbach resonance (see Ch. 2). The observed shift in the energy of the impurity, as already shown in Fig. 4.1, provides fundamental evidence for the existence of the polaron. The nature of the injection protocol is thus to probe the system through the direct transfer to the impurity state.

Due to loss processes in our system, the impurities are lost before detection is possible. These are expected to consist of three-body recombinations involving an impurity and two medium atoms. Therefore, only the remaining number of medium atoms are detected and this observed loss of medium atoms is taken as the experimental signal, as high losses are observed when the rf-pulse is resonant with the impurity state. This is also called *loss spectroscopy*, given that the rf-spectrum is inferred from the loss of medium atoms. An example of this is shown in Fig. 4.2. Far from the resonance position, a constant atom number is observed. Closer to the resonance, a dip in atom number is observed, with a minimum that is shifted relative to $E/E_n = 0$, which is the measured transition between the $|1\rangle$ and $|2\rangle$ states for thermal atoms. From this signal, the observed spectral function is extracted by flipping and normalizing the signal as also shown in Fig. 4.2. As expected, there is a shifted peak with a tail towards higher energies, which are the fundamental experimental traits of the polaron.

Due to the use of a harmonic trapping potential and a finite rf-pulse duration, the observed spectral function is broadened significantly. For now, the exact modeling of the spectral function and the experimental modific-

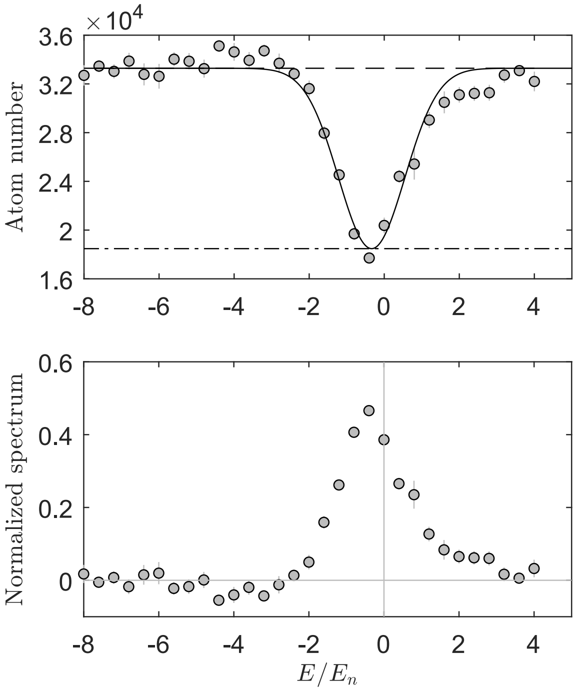

FIGURE 4.2: (top) Observed atom number (gray circles) as a function of the frequency of the rf-pulse in the injection protocol. The data is fitted with a Gaussian function (black solid line), to extract the atom numbers on- (dash-dotted horizontal line) and far off-resonance (dashed horizontal line). Adapted from [3]. (bottom) Normalized spectral response of the impurity with a shifted peak and a tail stretching towards higher energies.

ations are ignored, and instead, we focus on the difference in the observed atom losses, off- and on-resonance. These are extracted by fitting the data with a Gaussian function. This is similar to how the spectral function of the polaron was initially modeled [51]. For the observed atom numbers in Fig. 4.2, the difference in the off- and on-resonance numbers is $\sim 1.5 \times 10^4$.

This number corresponds to the maximal loss of medium atoms in the system when the highest number of impurities are generated. In this specific case, the impurity fraction is 15%, which was measured by performing Rabi oscillations on the $|1\rangle$ to $|2\rangle$ state transition, with thermal atoms. From the off-resonance atom number of $\sim 3.3 \times 10^4$, the average number of medium atoms lost per impurity is calculated to $\frac{1.5\times10^4}{0.15\cdot3.3\times10^4} - 1 \sim 2.03$, fitting well with the expected number of 2 for perfect three-body recombination. This example outlines a method for extracting information on the loss process from the observed spectrum. This is further investigated in the following for a two-pulse spectroscopy sequence.

4.2.2 Ejection Spectroscopy

The injection protocol discussed above is characterized by a single rf-pulse, which attempts to inject directly into the polaron state. A more advanced technique is the so-called *ejection* protocol, which for our system uses a sequence of two rf-pulses and the third Zeeman substate, $|F = 1, m_F = +1\rangle \equiv |3\rangle$. The sequence is illustrated in Fig. 4.3, with the relevant loss channels depicted as well. The sequence starts with an initial rf-pulse that has a duration that is as short as possible and fixed to the transition between the $|1\rangle$ and $|2\rangle$ states, measured for thermal atoms. The short duration of this rf-pulse means that it is very broad in the frequency spectrum, which ensures the population of the impurity state. The system then evolves through the impurity-medium interactions, with three-body recombination processes taking place as well. At the end of the evolution time, the ejection sequence is closed by a final rf-pulse, which attempts to transfer, or *eject*, the impurities to the third state, $|3\rangle$. If this is successful, a peak is observed in the spectrum as explained in the following.

The losses between the medium and impurity state are dominated by three-body recombination. However, for successful transfer of the impurities to the third state, $|3\rangle$, two-body recombination is possible through spin exchange collisions between an impurity and a medium atom. This

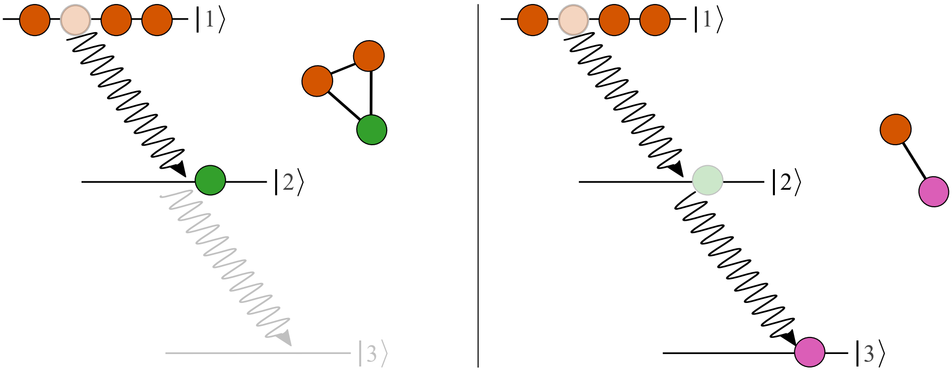

FIGURE 4.3: Illustration of the ejection protocol consisting of two rf-pulses, with the relevant states for our system (see main text). (left) For impurities in the $|2\rangle$ state, the losses are dominated by three-body recombination of one impurity and two medium atoms. (right) For impurities in the $|3\rangle$ state, the losses involve only one impurity and one medium atom. Adapted from [3].

process is much faster and only results in one medium atom lost per impurity. Thus, if the second rf-pulse is resonant with the impurity energy, a lower atom loss due to two-body recombination is observed as a peak in the spectrum, from which the properties of the polaron can be extracted. An example of this is shown in Fig. 4.4, resembling that of the injection protocol in Fig. 4.2. The spectrum consists of a peak and a tail, which now extends towards lower energies.

Just as for the injection spectrum discussed above, the exact form of the spectral function for the ejection protocol is ignored for now, and only the atom numbers off- and on-resonance are considered. The spectrum in Fig. 4.4 is fitted with a Gaussian function to extract the atom number off- and on-resonance, as also indicated in the figure. The atom number off-resonance corresponds to the case where the second rf-pulse has effectively no impact and all impurities remain in the $|2\rangle$ state and are lost

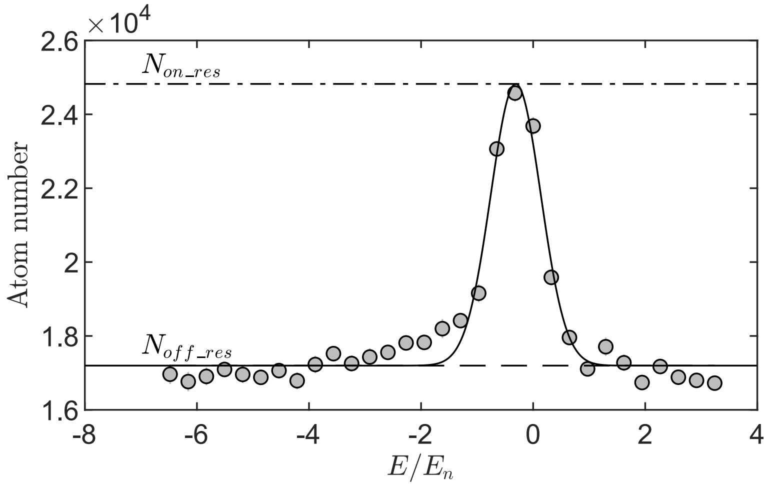

FIGURE 4.4: Observed atom number (gray circles) for the ejection protocol. This spectrum is similar to that observed for the injection protocol in Fig. 4.2 consisting of a peak and a tail, which is now stretching towards lower energies. The data is fitted with a Gaussian function (black solid line) to extract the atom number on- (dash-dotted horizontal line) and far off-resonance (dashed horizontal line). Adapted from [3].

through three-body recombination. From the observed atom number off-resonance, the number of medium atoms lost per impurity, due to three-body recombination, can be estimated. This was exactly the scenario discussed for the injection spectrum at resonance. If the second rf-pulse is resonant, a lower total loss of medium atoms is observed, which is due to a combination of three-body recombinations during the evolution time, and two-body spin-exchange collisions after the rf-pulse. In the limit of very short evolution time, the loss observed at the peak is expected to be purely two-body.

This section has thus introduced the injection and ejection protocols, with examples of typical spectra for both. Besides being of interest in terms of characterizing the properties of the polaron itself, these spectra also contain information regarding the loss processes for an impurity embedded in a Bose-Einstein Condensate. The loss processes are important to characterize such that they can be properly accounted for when investigating polaron physics. This is further discussed in the following section.

4.3 Three-body Recombination

For the case of a pure medium, three-body recombination processes are well described by including an empirical term to the GP equation (see Ch. 2). This leads to a differential equation for the atom number

$$\frac{dN}{dt} = -L_3 \int n(\mathbf{r})^3 d^3\mathbf{r}, \tag{4.1}$$

where L_3 is the three-body loss rate coefficient, and n is the atomic density. For the case of a harmonic trapping potential, the density distribution of the condensate is well described in the Thomas-Fermi approximation as

$$n(\mathbf{r}) = n_0 \left[1 - \left(\frac{r}{R}\right)^2\right]. \tag{4.2}$$

The peak density and spatial extent of the condensate are given by n_0 and $R = (2\mu/m\overline{\omega}^2)^{1/2}$, with the geometric mean of the trapping frequencies $\overline{\omega} = (\omega_x\omega_y\omega_z)^{1/3}$ as well as the chemical potential μ. From this density distribution, the integral in Eq. (4.1) gives the solution

$$\frac{dN}{dt} = -L_3 \frac{7}{6} \frac{15^{4/5}}{(14\pi)^2} \left(\frac{m\overline{\omega}}{\hbar\sqrt{a_B}}\right)^{12/5} N^{9/5}, \tag{4.3}$$

where a_B is the scattering length between the BEC atoms [138]. This equation can be numerically solved and fitted to experimental data in order to extract the three-body loss rate coefficient, L_3. The above procedure only works for repulsive interactions ($a_B > 0$) between the BEC atoms, which collapses for attractive interactions [84]. For this reason, the regime of negative scattering lengths is usually investigated using thermal gases.

For a thermal gas, the density distribution in a harmonic trap is given by a Gaussian distribution, with an explicit dependence on the atom number and temperature. This results in two coupled differential equations for the temperature and atom number, which can be numerically solved by comparing with experimental data, allowing for the extraction of the three-body loss rate coefficient [74, 86]. To compare the results of the condensed and non-condensed systems, the suppression of density fluctuations in a BEC needs to be accounted for [139]. This leads to a suppression of the three-body loss rate for the BEC by a factor of 6, compared to the non-condensed gas.

In the specific case of ^{39}K , the three-body loss rate has been investigated at both positive and negative scattering lengths, for a single component gas in a harmonic trap [74, 140], as well as recently in a box potential [141]. These provide strong experimental evidence for a universal behavior of the three-body loss rate given by, $L_3 \propto a^4$. Note that the scattering length has now been generalized to a, to separate it from the internal scattering length of the BEC, a_B, which appears through the Thomas-Fermi density distribution. In the context of impurity physics, it is the interstate scattering length between the medium and impurity state, a, that the three-body loss rate is expected to show a dependence on. The universal behavior can be qualitatively understood in terms of the two-body scattering cross section (see Eq. (2.4)). The cross section is proportional to a^2 and by introducing a third atom another factor of a^2 is included, giving the a^4 behavior for the three-body recombination.

In the context of this thesis, the system of interest is that of a mixture of the medium and impurity state given by the internal states of ^{39}K, $|F = 1, m_F = -1\rangle \equiv |1\rangle$ and $|F = 1, m_F = 0\rangle \equiv |2\rangle$. The loss of this system is described by a set of coupled differential equations for the number of the medium and impurity atoms, N_B and N_I,

$$\begin{aligned}\frac{dN_B}{dt} =& -\frac{2}{3}L_3^{BBI}\int n_B(\mathbf{r})^2 n_I(\mathbf{r}) d^3\mathbf{r} - \frac{1}{3}L_3^{BII}\int n_B(\mathbf{r}) n_I(\mathbf{r})^2 d^3\mathbf{r} \\ & - L_3^{BBB}\int n_B(\mathbf{r})^3 d^3\mathbf{r},\end{aligned} \tag{4.4}$$

with an equivalent one for N_I, by swapping the indexes [142]. The three terms on the right represent the different three-body recombination channels of the system, which have different dependencies on the atomic densities $n(\mathbf{r})$. The interactions in the system are described by the internal scattering lengths of each component, a_B and a_I, as well as their interstate scattering length, a. Usually, only one of these is tuned through a Feshbach resonance, with the others at relatively constant values.

Previous investigations of ^{39}K in the context of bright solitons and quantum droplets explored the three-body recombination losses of the $|1\rangle$ and $|2\rangle$ states [143–145]. It was found that three-body recombination of three atoms in the $|2\rangle$ state dominated the losses. The losses due to three-body recombination in the $|1\rangle$ state, as well as those between the $|1\rangle$ and $|2\rangle$ states, were found to be comparable to background losses [146]. However, for these investigations, the intrastate and interstate scattering lengths were all below $100a_0$, which is much smaller than those used in this thesis for investigating polaron physics.

In the impurity limit of the above mixture, the system only contains a small fraction of the $|2\rangle$ state. Such a setting allows for excluding the second loss channel term in Eq. (4.4), given that the low density of the impurities significantly decreases their internal scattering probability. Additionally, the interstate scattering length between medium and impurity is typically tuned to very large values. The three-body recombination due to an impurity and two medium atoms is therefore expected to dominate the losses of the system, on the timescales typically considered. Experimental investigations of the medium losses for attractive impurity-medium interactions using the ejection protocol are further discussed in the following section, leading to the paper [3].

As a final comment on three-body physics, it is noted that the existence of three-body bound states, described by Efimov physics as briefly discussed in Ch. 2, are observed as sharp resonances in the three-body loss rate when tuning the scattering length [73]. This effect is enhanced for highly mass-imbalanced systems, where a light atom can more easily mediate interactions between two heavy atoms [78]. This has been experimentally exploited for systems containing ^{6}Li$-^{87}$Rb [147] and ^{6}Li$-^{133}$Cs mixtures [148, 149]. Additionally, for the case of an impurity immersed in a Bose-Einstein Condensate, the effects of Efimov physics have been predicted to significantly affect the attractive polaron energy [79, 80], or even cause a collapse at strong interactions [67]. In our system, the medium and impurity have equal masses and the expected effects of Efimov physics are significantly reduced. In fact, the scattering threshold for the impurity-medium-medium trimer state is $|a_-| = 3 \times 10^5 a_0$ [51], which is orders of magnitude above the scattering lengths we typically use.

4.4 Three-body Physics in the Impurity Limit in ^{39}K

Characterizing the losses of an impurity embedded in a Bose-Einstein Condensate is critical for understanding and analyzing the experimental results. Three-body recombination losses have previously been theoretically investigated for repulsive impurity-medium interactions to account for the observed discrepancies between the theoretical and experimentally extracted energies of the repulsive polaron branch [53]. It has also been experimentally investigated with an ejection protocol at attractive [57] and repulsive [2] impurity-medium interactions and analyzed with a simple empirical model. In the following paper [3], the losses at attractive impurity-medium interactions are re-investigated and analyzed using a new model, which allows for extracting the atom number of the medium at a variable time in the ejection protocol. Such a method is valuable for ejection spectroscopy to estimate the density of the system at the point where it is probed, which is further emphasized in Ch. 5.

4.4.1 Results

The losses in the ejection protocol consist of either three-body recombination during the evolution time or fast two-body spin-exchange collisions after the second rf-pulse has been applied. The decay of the medium is observed by varying the evolution time and generally contains both types of losses. By utilizing the limits of the observed decay, the real decay curve representing only three-body recombinations of one impurity and two medium atoms is obtained. This real decay curve is fitted with a differential equation describing this loss process, for which the density distribution of the BEC in the harmonic trap is specifically utilized. From this fit, the three-body loss rate coefficient is extracted and by varying the impurity-medium scattering length, this coefficient is traced from weak to strong interactions. A good agreement with the expected universal behavior of a^4 is observed, with an eventual saturation at large scattering lengths.

The extracted three-body loss rate coefficients allow for calculating the medium atom number at any point in the ejection protocol. This is important when performing ejection spectroscopy to estimate the atomic density at the point of applying the second rf-pulse, which sets the characteristic scaling parameters E_n and k_n. If these parameters are not accurately known, systematic discrepancies between the extracted and theoretical polaron energies can be expected. It is also shown that the medium atom number can be extracted directly from the observed ejection spectrum, which is compared to the results from applying the three-body loss rate coefficients, with good agreement.

Finally, the number of medium atoms lost per impurity is extracted experimentally as a function of the impurity-medium interaction strength. This is observed to increase at strong interactions, where as many as 3-4 medium atoms are lost per impurity on average. This is interpreted as a result of secondary collisions in the system, after the initial three-body recombination process.

4.4.2 Outlook

In the impurity limit of mixtures, the three-body recombination processes are simpler to model and the observations are easier to interpret. The extracted values of the three-body loss rate coefficients are fairly consistent with those for a single component thermal gas of ^{39}K at similar scattering lengths [74, 140, 150]. However, for a single component gas, the scattering is between three identical bosons, whereas for our results the scattering is between two identical bosons and a third boson. Importantly, the interactions tuned are those between the third boson (the impurity) and the two identical bosons (the medium atoms). Such systems have been predicted to show distinct behavior in terms of the scaling dependence of the scattering length [151] and the dimensionless parameter C [152], although still with a a^4 dependence to leading order.

Compared to the previous investigation of the losses in our system [57], it is clear that the empirical model of the decay will overestimate the three-body recombination losses. At the time, good quantitative agreement between the experimental data and the modified theory was observed, which merited the use of this model.

As discussed in Sec. 4.3, there are important differences between a thermal and condensed gas when investigating three-body recombination losses. In addition to these, the high densities of the BEC may also affect the losses, which have been observed to suppress the three-body recombination [153]. It may therefore be relevant to re-investigate the three-body recombination losses observed here, for thermal gases in the impurity limit.

It is a surprising result that the observed number of medium atoms lost per impurity increases to as much as 4 for strong impurity-medium interactions. Secondary collisions have been quantitatively investigated for repulsive interactions [74], and are understood to be caused by an avalanche effect [154]. For our system, these secondary collisions are assumed to only involve medium atoms such that a consistent behavior for ejection spectroscopy can be expected, even at strong interactions.

It would be natural to extend the above results to the repulsive side of impurity-medium interactions. Much of the theory described here should apply to this side, and a similar overall behavior is expected. However, the response at large scattering lengths may prove difficult to probe given the inherent instability of the repulsive polaron state.

Finally, the results of this paper [3] may also find a use for the multiple experiments that investigate impurity physics through loss spectroscopy with ^{39}K [52, 106], to properly account for these processes. The methods and techniques can of course also be extended to other systems as well.

4.4.3 Publication

For the following paper [3], I was part of conducting the experiment and collecting the experimental data. I also performed the data analysis, including all the figures and I wrote the first draft of the paper.

The paper will be submitted to Physical Review A under the American Physical Society organization, after the submission of this thesis.

Three-body Physics in the Impurity Limit in ^{39}K

A. M. Morgen,[1] S. S. Balling,[1] M. T. Strøe,[1] M. G. Skou,[1] and J. J. Arlt[1]
[1] *Center for Complex Quantum Systems, Department of Physics and Astronomy, Aarhus University, Ny Munkegade 120, DK-8000 Aarhus C, Denmark*

(Dated: August 27, 2024)

Loss spectroscopy is an important tool for investigating systems where intrinsic loss processes prevent direct observation of the constituents. Here, we discuss the use of loss spectroscopy to evaluate the properties of impurities embedded in a Bose-Einstein Condensate (BEC), based on two- and three-body loss processes. The impurity limit of the system allows for the quantitative evaluation of the three-body loss processes including two BEC atoms and one impurity. This loss process is analyzed on a microscopic level, allowing us to extract the associated three-body loss rate coefficient. It enables the extraction of the density of the BEC at a variable point in the experimental sequence, which is of crucial importance for understanding the effects of impurities at strong interactions. Moreover, we demonstrate a method for extracting the density directly from the observed spectrum and compare the results. Both methods allow for an evaluation of the number of lost medium atoms per loss event, which exceeds 2 at strong interactions. These additional losses are interpreted as a consequence of secondary collisions in the medium.

I. INTRODUCTION

Loss processes in ultracold quantum gases often complicate measurements, adding to the complexity of analyzing and interpreting the observed results. One such case is atom interferometry where atomic losses impose additional decoherence on the quantum system [1–5]. However, for a wide range of experiments, the atomic loss is the observable from which exciting physics can be inferred. An example is Efimov physics, where a peak in the observed loss rate of atoms is indicative of three-body bound states [6, 7]. Similarly, Feshbach resonances can also be inferred from the observed losses, which increases as the resonance is approached [8]. Losses may even be used to investigate exotic quantum phase transitions such as the Mott insulator to superfluid transition [9] and nonequilibrium phase transitions in circuit quantum electrodynamics [10].

For an impurity embedded in a Bose-Einstein Condensate (BEC), spectroscopy is the principle tool for probing the spectral response of the emerging quasiparticle state as the interaction between the impurity and medium atoms is tuned [11–14]. Due to three-body recombination, losses of atoms in both the medium and impurity states are expected and often prohibit direct observation of the impurities. Instead, the observed loss of medium atoms is used to infer the properties of the impurity. In addition, they provide insight into the few-body physics characterizing the loss processes. The losses also change the system itself, which is characterized by the atomic density of the system. Accurately modeling the losses is therefore necessary to estimate the density of the system when probing it, in order to interpret the results and avoid systematic discrepancies between experimental results and theoretical predictions.

Loss processes for an impurity immersed in ultracold gases have previously been investigated for $^{87}\mathrm{Rb}-^{133}\mathrm{Cs}$ [15] and $^{41}\mathrm{K}-^{87}\mathrm{Rb}$ [16] mixtures, where the impurity limit allows for isolating the possible three-body recombination processes. This is also exploited for our system, where a BEC of ^{39}K is utilized.

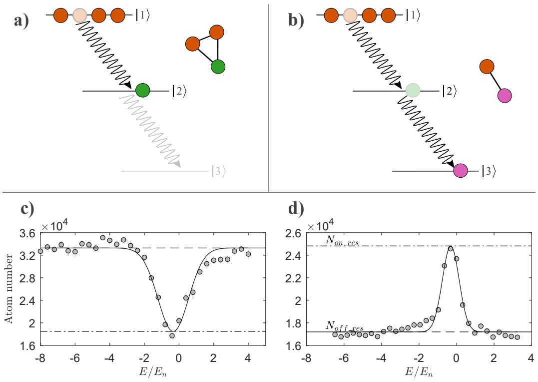

FIG. 1. Illustration of the ejection spectroscopy sequence with the relevant states depicted and loss channels due to **a)** three-body recombination and **b)** two-body spin exchange collisions. **c)** Injection and **d)** ejection spectroscopy signals at inverse interaction strength of $1/k_n a = -1$, fitted with Gaussian functions. For ejection, an increase of medium atoms is observed at the resonance frequency, while for injection a decrease is observed. The dashed line refers to the case of maximal loss for ejection and no loss for injection. The dashed-dotted line shows the maximal gain of medium atoms for ejection and maximal loss in ejection.

In the context of loss spectroscopy, the observed loss of medium atoms is dependent on successfully transferring the medium atoms to the impurity state. This loss is largest when the transfer is largest, which is the case at the resonance frequency between the two states. This single-pulse sequence for spectroscopy is also known as *injection spectroscopy*, due to the nature of injecting into the medium state. Here, we show that a third state can be used in a two-pulse spectroscopy sequence referred to as *ejection spectroscopy* [17], to evaluate the nature of the loss mechanism. In the ejection sequence, the impurities are initially created with a radio frequency (rf) pulse, followed by a variable evolution time until a second rf-pulse probes the system by transferring the impurities out again.

The paper is organized as follows. An introduction to the experimental ejection sequence is provided in Sec. II, with an overall description of our system in Sec. III. The loss channels of our system are considered in Sec. IV, with calculations for the medium density at a variable time in the ejection sequence. The three-body loss rate is analyzed and compared to theoretical predictions in Sec. V, along with previous empirical analysis in Sec. VI. In Sec. VII, the atomic density is calculated and in Sec. VIII the number of medium atoms lost per impurity is investigated. Finally, a conclusion on our results is provided in Sec. IX.

II. LOSS SPECTROSCOPY TECHNIQUE

The ejection spectroscopic measurement is initiated by a short rf-pulse, that creates a superposition of atoms in the medium state, $|1\rangle$, and the impurity state, $|2\rangle$. The system is then allowed to evolve before a second rf-pulse is applied, which transfers the impurity atoms to a third state, $|3\rangle$. This transfer only happens if the frequency of the second rf-pulse matches the energy difference between the $|2\rangle$ and the $|3\rangle$ state. Importantly, only three-body losses are allowed between the $|1\rangle$ and the $|2\rangle$ state, but two-body losses are possible between the $|1\rangle$ and the $|3\rangle$ state, as also illustrated in Fig. 1. The latter occurs faster but results in fewer lost medium atoms. Consequently, the observed loss of atoms in the medium state is lowered if the transfer to state $|3\rangle$ is successful, and a peak of medium atoms is observed at the resonance energy. The ejection spectroscopy sequence together with the different loss channels are illustrated in Fig. 1, with examples of ejection and injection spectra.

Ejection spectroscopy offers the advantage that the system is first prepared and allowed to evolve and settle before it is probed. Conversely, injection spectroscopy directly probes the system with the initial transfer, which generates additional excitations in the system, effectively shifting the observed spectral function [17].

III. EXPERIMENTAL IMPLEMENTATION

Our experiment is performed with BECs of ^{39}K, produced in an optical dipole trap [18] in the ground state $|F=1, m_F=-1\rangle \equiv |1\rangle$, with F and m_F the total angular momentum quantum number and its projection, respectively. The impurity state is the $|F=1, m_F=0\rangle \equiv |2\rangle$ state, with the third state, $|F=1, m_F=+1\rangle \equiv |3\rangle$, used for the ejection sequence. An interstate magnetic Feshbach resonance at 113.8 G, between the medium, $|1\rangle$, and impurity state, $|2\rangle$, [19, 20], allows for tuning of the interactions, characterized by the impurity-medium scattering length, a.

In experiments involving ultracold quantum gases, characteristic parameters associated with the atomic density, are used for convenient scaling of the system. These parameters are the characteristic energy, $E_n = \hbar^2 k_n^2/2m$ and wavenumber, $k_n = (6\pi^2 n)^{1/3}$, which also enters the impurity-medium inverse interaction strength, $1/k_n a$, where n is the atomic density of the medium. In the ejection sequence described above, it is the density at the point of applying the second rf probe pulse that is relevant for calculating the scaling parameters E_n and k_n. However, it is not equal to the observed density at the end of the experimental sequence, which is lower since all impurities are always lost before detection, either through two- or three-body recombination. This makes it necessary to develop a method for reconstructing the atomic density at a variable time in the ejection sequence.

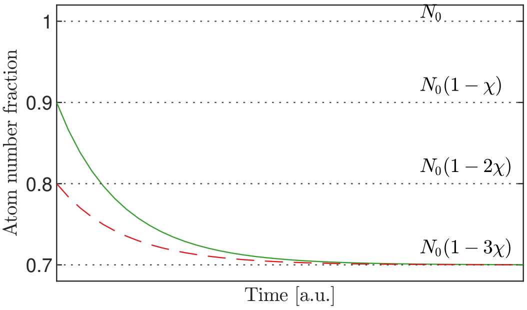

FIG. 2. Illustration of the expected decay of the medium atom fraction, $N(t)/N_0$, with an initial atom number N_0 and impurity fraction $\chi = 10\%$, in terms of the real (green solid line) and observed decay curves (red dashed line). The former of these is the result of pure three-body recombination between medium and impurity atoms, whereas the latter also contains additional two-body losses. The decay curves start at different medium atom fractions, indicated by the horizontal lines.

IV. ATOM NUMBER RECONSTRUCTION

In the following, two approaches for calculating the medium atom number at a variable time in the ejection sequence are presented. The first of these involves recording the loss rate of medium atoms in the presence of impurity atoms. The second utilizes the observed atom number in the ejection spectrum to infer the number of the medium atoms at the point of probing the system.

A. Decay curve reconstruction

To calculate the density of the system at a variable time, the loss process associated with the interaction between atoms in the $|1\rangle$ and $|2\rangle$ states is examined. If this loss rate is known, the density at any point during the ejection sequence can be determined from the initial density.

In order to measure the loss rate, the number of medium atoms as a function of time is observed using the ejection sequence for a chosen initial impurity concentration. Additionally, the probe pulse has a short duration and is fixed with respect to the $|2\rangle$ to $|3\rangle$ transition. The expected outcome of this

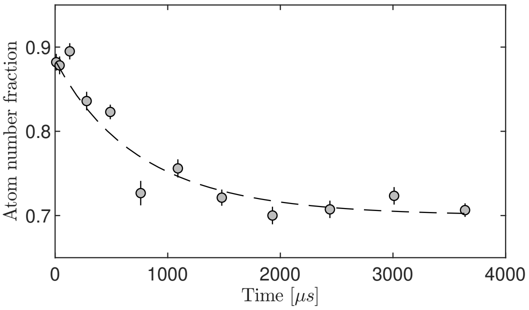

FIG. 3. Example of reconstructed decay $N(t)/N_0$ from the observed decay using Eq. (3), at low scattering length ($-200a_0$). The data is fitted with Eq. (10) (black dashed line) and the three-body loss rate coefficient, L_3, is extracted.

measurement is illustrated in Fig. 2, where two decay curves are plotted. One of these is the real decay curve, representing the loss of medium atoms due to interactions between atoms in the $|1\rangle$ and $|2\rangle$ states, assuming perfect three-body recombination. The second decay curve is the observed decay curve, which lies below the real decay due to the additional two-body losses occurring after the probe pulse.

Assuming a BEC with initial N_0 atoms, the first rf-pulse populates the impurity state with a fraction, χ, of the total atom number. The real decay of the medium atoms starts at $N_0(1-\chi)$ and decreases down to $N_0(1-3\chi)$ for long times. The observed decay always has additional losses due to the transfer to the $|3\rangle$ state in the ejection sequence, which means that it starts at $N_0(1-2\chi)$ and decays to $N_0(1-3\chi)$ for long times. Despite this difference, it is possible to reconstruct the real decay from the more involved observed decay. The reconstructed decay then only reflects the loss process between the medium and impurity state, as desired. Reconstruction requires adding the number of atoms lost after the probe pulse to the observed data points.

This number of atoms is derived by considering the following. During the evolution time, interactions between the impurity and medium atoms lead to losses, and the number of medium atoms at a variable time is given by

$$N(t) = N_0(1-\chi) - \eta_3(N_0\chi - N_i(t)), \tag{1}$$

where η_3 is the number of medium atoms lost per impurity in the $|2\rangle$ state, expected to be equal to 2 for perfect three-body losses, $N_i(t)$ is the remaining number of impurity atoms at time t, N_0 is the initial BEC atom number and χ is the initial impurity fraction. The probe pulse transfers the remaining impurities to the third state, $|3\rangle$, where additional losses decrease the number of observed medium atoms to

$$N_{\text{obs}}(t) = N(t) - \eta_2 N_i(t), \tag{2}$$

where η_2 is the number of medium atoms lost per impurity in the $|3\rangle$ state, expected to be equal to 1 for perfect two-body losses. To obtain $N_i(t)$, the observed atom number for long evolution times is considered. In this case, all impurities are lost before the probe pulse is applied and the observed atom number is $N_\infty \equiv N(t\to\infty) = N_0(1-\chi) - \eta_3 N_0\chi$. The difference between $N_{\text{obs}}(t)$ and N_∞ corresponds to the number of medium atoms "saved" from three-body recombination. This difference is also equal to the number of impurities at time t, $N_i(t)$, times the difference in the loss coefficients η_3 and η_2. Inserting this result into Eq. (2) and rearranging gives

$$N(t) = N_{\text{obs}}(t) + \eta_2 \frac{N_{\text{obs}}(t) - N_\infty}{\eta_3 - \eta_2}. \tag{3}$$

The above equation then allows for reconstructing the real decay, $N(t)$. The coefficient η_2 (η_3) is experimentally measured from the observed decay at short (long) evolution times, where only two-body (three-body) losses are observed. An example of a reconstructed decay curve is shown in Fig. 3, at low impurity-medium scattering length. As expected, the reconstructed decay starts at $0.9N_0$ and decreases to $0.7N_0$ at long times.

B. Spectroscopy reconstruction

In the above derivation, it was the evolution time between the two rf-pulses in the experimental sequence that was varied, with their respective frequencies fixed. For the ejection spectroscopy sequence, the probe pulse has a longer duration (typically ∼ 20 µs for our system) to provide a sufficient energy resolution and its frequency is varied to record the spectrum, as also shown in Fig. 1. In this case, a similar calculation for reconstructing the atom number is possible, as explained in the following. If the probe pulse is off-resonant, all impurities remain in the $|2\rangle$ state and are lost through three-body recombination, and the observed atom number off-resonance is $N_{\text{off-res}} = N_\infty$. If the probe pulse is on resonance, the remaining impurities are transferred to the $|3\rangle$ state, and the observed atom number corresponds to $N_{\text{on-res}} = N_{\text{obs}}$, as given by Eq. (2). The difference between the observed on- and off-resonance atom number is $N_{\text{on-res}} - N_{\text{off-res}} = N_i(t)(\eta_3 - \eta_2)$. This is slightly different compared to the desired term $N_i(t)\eta_3$, which should be added to $N_{\text{off-res}}$ to acquire Eq. (1). However, under the assumption of exact three- and two-body losses, $\eta_3 - \eta_2 = 1$, the atom number at the point of applying the probe pulse is

$$N(t) = N_{\text{off-res}} + \eta_3(N_{\text{on-res}} - N_{\text{off-res}}). \tag{4}$$

The results of Eq. (3) and (4), provide a framework for reconstructing the medium atom number to exclude the additional losses taking place after the probe pulse. Importantly, from the former of these, the decay is reconstructed and the loss processes are examined. The latter is used in the context of ejection spectra, where an accurate determination of the density is necessary for calculating the characteristic scaling parameters, E_n and k_n, to compare the extracted features with theoretical predictions.

V. THREE-BODY LOSS ANALYSIS

In a more microscopic approach, the three-body recombination loss process is examined in this section and compared to the reconstructed decay according to Eq. (3). The starting point is the following differential equation for the number of medium atoms

$$\frac{dN_B}{dt} = -\frac{2}{3}L_3^{BBI}\int n_B^2 n_I d^3r - \frac{1}{3}L_3^{BII}\int n_B n_I^2 d^3r \\ -L_3^{BBB}\int n_B^3 d^3r - N_B/\tau, \tag{5}$$

where the subscripts B and I, refer to the medium and impurities, with atomic densities n_B and n_I [7, 21]. The three-body loss rate coefficient L_3 is specified for the particular loss channel for each of the terms. Losses due to collisions with background atoms are modeled by the term $-N_B/\tau$. Given that only the medium atoms are observed, we set $N_B \equiv N$. The differential equation is simplified by the following considerations. The impurity density is much smaller than the BEC, which means that the second term in Eq. (5) is neglected. Additionally, the scattering length between the BEC atoms is only $10a_0$ and the timescale associated with the measurements is much shorter than those associated with background collisions, such that the third and fourth terms can be neglected as well. These considerations transform Eq. (5) into

$$\frac{dN}{dt} = -\frac{2}{3}L_3\int n_B^2 n_I d^3r, \tag{6}$$

with $L_3 \equiv L_3^{BBI}$. The generated impurities are expected to retain the same distribution as the BEC [13] and we therefore make the approximation, $n_I = \rho n_B$, where ρ is the density fraction of impurities in the system. This corresponds to single-mode approximation. Inserting this into Eq. (6) yields

$$\frac{dN}{dt} = -\frac{2}{3}L_3\rho\int n_B^3 d^3r. \tag{7}$$

Using the Thomas-Fermi approximation for the density distribution of the BEC, the above integral has a well-known solution [22]. The density fraction of impurity atoms in the system is time-dependent and can be written in terms of the medium and impurity atom numbers as

$$\rho(t) = \frac{N_i(t)}{N(t)}, \tag{8}$$

where $N_i(t)$ and $N(t)$ are the number of impurity and medium atoms at time t, respectively. The relation between these is given by Eq. (1), where solving for $N_i(t)$ and inserting into Eq. (8) yields

$$\rho(t) = \frac{N(t)/N_0 + \chi(1+\eta_3) - 1}{N(t)/N_0}. \tag{9}$$

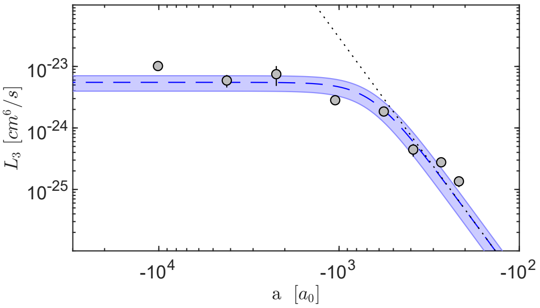

FIG. 4. Extracted three-body loss rate coefficients (gray points) as a function of the impurity-medium scattering length, a. A fit to the data with Eq. (12) (blue dashed line) captures the saturation and the initial a^4 behavior (black dotted line) assuming $n_l = 3$. The error of this fit is indicated by the blue shaded region.

Inserting these results into Eq. (7) gives the following differential equation for the decay of the medium atom number

$$\frac{dN}{dt} = -\frac{1}{2!}\frac{2}{3}L_3\frac{7}{6}\frac{15^{4/5}}{(14\pi)^2}\left(\frac{m\bar{\omega}}{\hbar}\right)^{12/5}\frac{1}{a_B^{6/5}}N^{9/5} \\ \times\frac{N/N_0 + \chi(1+\eta_3) - 1}{N/N_0}, \tag{10}$$

where a_B is the medium-medium scattering length and $\overline{\omega} = (\omega_x\omega_y\omega_z)^{1/3}$ is the average trap frequency. The reduced effect of atom-bunching for a BEC, also means that the observed L_3 is expected to be lower compared to the case of a thermal cloud [23]. For a thermal gas, the probability of finding three atoms close together is 3! times higher compared to an ideal BEC. For our system, this suppression factor of the three-body recombination is expected to be lower, given that only two of the three particles are BEC atoms. As a result, we include a suppression factor of $1/2!$ in Eq. (10) [24, 25].

This differential equation is solved numerically and fitted to the reconstructed decay, as shown in Fig. 3, with L_3 as a free parameter. The three-body loss rate coefficient is investigated at different impurity-medium interactions by repeating this measurement at varying impurity-medium scattering lengths, a. The extracted three-body loss rate coefficients are shown in Fig. 4, which are observed to initially increase as $|a|$ is increased, but start to saturate at large values of $|a|$. The behavior of the three-body loss rate coefficient, L_3, is expected to follow a universal behavior given by

$$L_3 = n_l C\frac{\hbar}{m}a^4, \tag{11}$$

where n_l is the number of atoms in the collision and C is a dimensionless constant, effectively acting as a free fitting parameter [26]. As the scattering length is increased, the three-body loss rate is expected to eventually saturate for a system with a finite temperature [21, 27]. To account for this saturation, the three-body loss rate is modified to

$$L_{\text{eff}} = \left(\frac{1}{L_{\max}} + \frac{1}{L_3} \right)^{-1}, \tag{12}$$

where $L_{\max}$ is a fitted saturation value and L_3 is given by Eq. (11). This effective three-body loss rate is fitted to the experimental data and plotted in Fig. 4, with the universal behavior shown independently. The fit captures the data well, from the universal a^4 behavior for small scattering lengths toward the saturation at large scattering lengths. The fitted value, $C = 7.69(3.33) \times 10^2$, is higher than the expected theoretical prediction of $\sim 1.33 \times 10^2$, for two identical bosons interacting with a third boson [28]. For comparison, the corresponding value for three identical bosons interaction resonantly pairwise is $C = 4.56 \times 10^3$ [29].

The fitted saturation value, $L_{\max} = 5(1) \times 10^{-24}$ cm^6/s, can be compared to the theoretical saturation value of the thermal part of the cloud, for which the temperature can be estimated [30]. This theoretical value is calculated to 1.17×10^{-19} cm^6/s, which is considerably higher than the fitted value. The theoretical calculation is also for the case of three identical bosons which is not necessarily the same as for our system, where only two identical bosons are interacting with a third boson.

Based on the extracted loss rate coefficients in Fig. 4, the atom number for a variable time in the ejection sequence can be evaluated using Eq. (10). This calculation only requires the initial atom number, impurity fraction, and evolution time, all of which are known. This makes it possible to estimate the density before the experimental sequence. This stands in contrast to Eq. (4), where the density is evaluated from the observed atom number on- and off-resonance for the ejection spectrum. Before comparing the results of these two approaches, the method employed for our previous results is briefly examined in the following section.

VI. EMPIRICAL ATOM NUMBER DETERMINATION

An empirical solution for the observed decay of the medium atoms has previously been employed for our system in Ref. [3, 5], where it was approximated as an exponential decay and fitted with

$$N_{\text{obs}}(t) = A e^{-\Gamma t} + B, \tag{13}$$

where Γ is the associated loss rate of the observed decay. A solution in the form of an exponential decay for the differential equation in Eq. (6), requires that the spatial average of the density is constant with respect to time.

In Fig. 5, the observed decay of the medium atoms and the exponential fit are shown, and compared to the numerically solved differential equation in Eq. (10) for the reconstructed decay. The exponential fit is observed to capture the data well, but the two decay curves also clearly represent different interpretations. The conclusion is that the loss rate extracted from the exponential fit to the observed decay typically overestimates the losses between the medium and impurity states.

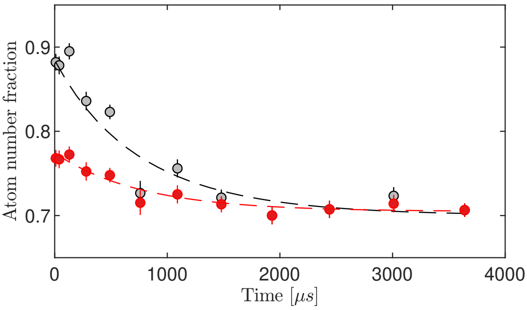

FIG. 5. Observed, N_{obs}/N_0, (red circles) and reconstructed, $N(t)/N_0$, (gray circles) atom number fractions at $a = -200a_0$, fitted with the exponential decay of Eq. (13) (red dashed line) and the differential equation in Eq. (10) (gray dashed line), respectively.

VII. ATOMIC DENSITY DETERMINATION

For experiments investigating impurity effects, the density of the system at the point of applying the probe pulse is the desired parameter, which is calculated from the atom number. The calculation of the medium atom number from the three-body loss rate coefficient in Eq. (10), relies on the assumption that the transferred impurity fraction and evolution time are well known. However, the effect of the finite duration of the probe pulse, effectively increasing the evolution time, is not inherently accounted for. The fraction of atoms transferred to the impurity state also contains some inherent uncertainties, since it is obtained from thermal atoms and not for a BEC. On the contrary, the method encapsulated by Eq. (4) for extraction of the medium atom number directly from the observed ejection spectrum does not require these parameters to be exactly known, as they are incorporated into the observed atom number on- and off-resonance. Calculating the density from the reconstructed atom number for each of these two approaches provides insight into how well they compare, as well as the inherent limitations of the experimental parameters.

The peak density of the system is calculated in the Thomas-Fermi approximation from the observed atom number N,

$$n_0 = \frac{15N}{8\pi} \left(\frac{m}{2\mu} \right)^{3/2} \bar{\omega}^3, \tag{14}$$

with the average trap frequency, $\overline{\omega} = (\omega_x \omega_y \omega_z)^{1/3}$, and chemical potential, μ.

The calculated densities are shown in Fig. 6, as a function of the inverse interaction strength. The measurements have evolution times around the same duration as the probe pulse of 20 µs. The three different calculations agree well with each other for low interaction strengths, whereas some discrepancies are observed at high interaction strengths, where the results from the differential equation lie systematically above the other methods. Calculated densities for a specific interaction strength and varying evolution times are also shown in

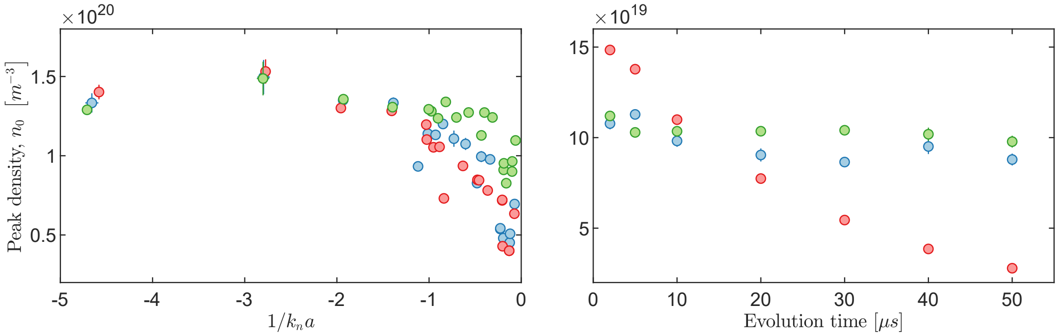

FIG. 6. Calculated peak densities at the point of applying the probe pulse in the ejection spectroscopy sequence using Eq. (4) (blue circles), the differential equation in Eq. (10) (green circles), and the exponential fit in Eq. (13) (red circles), as a function of (left) the inverse impurity-medium interaction strength and (right) the evolution time between the rf-pulses.

Fig. 6. It is clear that the exponential fit overestimates the density of the system at short times and underestimates it for long times, compared to the other methods. For long evolution times, the loss rate is expected to slow down since the density is continuously decreasing, which the exponential fit in Eq. (13) does not account for. On the other hand, this effect is expected to be encapsulated in both the differential equation in Eq. (5) as well as the reconstructed atom number in Eq. (4). Both of these methods show a much slower decrease in the calculated densities. For short evolution times, a substantial part of the losses take place during the probe pulse duration, resulting in an effective longer evolution time. This effect is only expected to be encapsulated in the reconstructed atom numbers from the ejection spectra. Nonetheless, both methods agree well with each other at short evolution times, leading to the conclusion that the effects of the finite duration of the probe pulse are small.

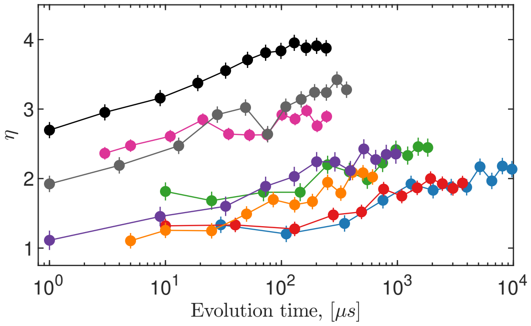

FIG. 7. Extracted general medium loss factor, η, as a function of time for different inverse interaction strengths, $1/k_n a = -4.2$ (blue), -3.2 (red), -2.4 (green), -1.6 (orange), -0.9 (purple), -0.4 (magenta), -0.2 (gray) and -0.1 (black). For weak interaction strengths, we observe the expected loss of 1 and 2 medium atoms per impurity for short and long times, respectively. For large interaction strengths, the losses are heavily increased, even at short times.

VIII. DOMINANT LOSS MECHANISMS IN ATOM NUMBER DETERMINATION

To obtain a more detailed understanding, the loss coefficients η_3 and η_2, defined in Sec. IV, are further examined. The loss coefficients are central for reconstructing the atom number from Eq. (3) and Eq. (4), and for evaluating the atom number through the differential equation in Eq. (10). Nominally, they should be equal to 2 and 1, corresponding to the number of medium atoms lost per impurity in the $|2\rangle$ and $|3\rangle$ state, respectively. In the following, they are extracted experimentally.

The observed decay in Fig. 2 is evaluated for very short and long evolution times. In the former case, the probe pulse is applied immediately after the first rf-pulse, and the observed losses are attributed to two-body processes between the $|1\rangle$ and $|3\rangle$ state. For long evolution times, maximal losses between the $|1\rangle$ and $|2\rangle$ state have already taken place through three-body processes when the probe pulse is applied. Generally, a loss coefficient for all evolution times can be extracted as

$$\eta = \frac{N_0(1-\chi) - N_{\text{obs}}(t)}{N_0 \chi}, \tag{15}$$

from which the loss coefficients η_2 and η_3 are extracted in the limits of short and long evolution times, respectively. For intermediate evolution times, the loss coefficient, η, contains contributions from both loss processes and provides insight into the dominant loss mechanism of the system. This loss coefficient is presented in Fig. 7 as a function of evolution time for different interaction strengths. For weak interaction strengths, the loss coefficient is indeed observed to be close to 1 for short evolution times and increases to 2 for long evolution times, as expected. However, for strong interactions, the losses are heavily increased, and the number of medium atoms lost per impurity increases to $3-4$. In this regime, the losses are also increased even for very short evolution times.

The observed increase of lost medium atoms at large in-

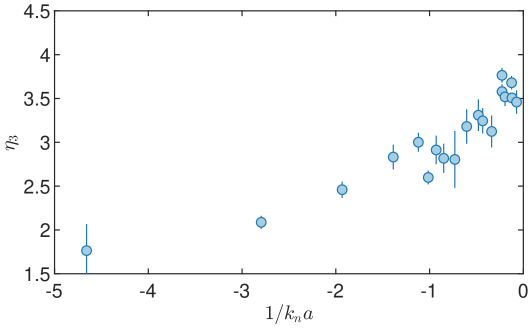

FIG. 8. Extracted η_3 loss factor as a function of the inverse interaction strength, calculated from the observed atom number off-resonance.

teraction strengths in Fig. 7, does not coincide with a sudden increase of the three-body loss rate coefficient in Fig. 4 that would indicate a loss behavior beyond the universal a^4 dependency, as would be expected from higher order Efimov states. This is not surprising given that the scattering threshold for the impurity-medium-medium Efimov trimer is $|a_-| = 3\times 10^5\ a_0$, well above the values used here [11, 31]. Instead, the additional observed loss is attributed to secondary collisions in the system [7, 32].

The results of Fig. 7 can also be compared to the loss coefficient, η_3, calculated from the off-resonance atom number in the ejection spectra. The off-resonance atom number was described in Sec. IV and allows for the calculation of

$$\eta_3 = \frac{N_0(1-\chi) - N_{\text{off-res}}}{N_0\chi}, \tag{16}$$

which is consistent with the form of the general loss coefficient in Eq. (15). The calculation of the loss coefficient η_3, requires input for the impurity fraction, which is estimated by performing Rabi oscillations with thermal atoms on the $|1\rangle$ to $|2\rangle$ transition, in an otherwise identical experimental setting. The obtained loss coefficients are shown in Fig. 8 as a function of inverse interaction strength. A clear increase in the loss coefficient for large interaction strength is observed and it is only for quite weak interaction strengths below $1/k_n a = -2$, that agreement with the expected pure three-body loss of $\eta_3 = 2$, is observed. Both of these limits are in good agreement with the ones observed in Fig. 7, showing the same overall behavior.

IX. CONCLUSION

In summary, we have examined the loss processes for an impurity immersed in a Bose-Einstein Condensate, to determine the atomic density of the BEC at a variable time in the ejection sequence. This was previously analyzed based on an exponential fit to the observed decay of medium atoms as a function of the evolution time [3, 5]. We now provide a microscopic analysis, by reconstructing the decay due to the losses between the medium and impurity state and include a realistic model for the three-body recombination processes. The three-body loss rate coefficient was extracted as a function of the impurity-medium interaction strength and observed to agree well with the expected universal behavior of a^4, with an eventual saturation at large scattering lengths. The density at the end of the ejection sequence was then calculated from the initial density and the extracted three-body loss rate.

Additionally, the density was also calculated directly from the observed ejection spectra using a method that only relies on the observed atom number. A comparison with the three-body calculation showed good agreement, both for varying interaction strength, as well as evolution time. Some discrepancies close to unitarity were observed, highlighting the limitations for modeling the three-body processes in this regime. Although the differences between the models are small, they can lead to systematic uncertainties which are important to account for when performing precision measurements.

Finally, the observed number of medium atoms lost per impurity, as a function of the interaction strength between impurity and medium atoms and the evolution time, is observed to increase when approaching unitarity at $1/k_n a = 0$. This was interpreted as caused by additional collisions between the medium atoms after the initial three-body recombination process.

The presented methods open up new ways to investigate collisional processes in ultracold gases, where the impurity limit of mixtures is specifically exploited to isolate these processes. The intricate loss processes of two identical bosons interacting with a third boson investigated here, show that the extracted three-body loss rate coefficient is lower, compared to investigations of single-component thermal gases of ^{39}K [7, 21], as expected [28]. Additional effects may also be considered when utilizing a BEC, such as the expected suppression of the three-body recombination at high densities [33].

Our results may find usage for systems directly involved with loss spectroscopy of ^{39}K [12, 14], but can also be extended to systems working with solitons and quantum droplets [34–36], Efimov physics [7, 21, 37], and collisional avalanches in BECs [32, 38].

---

[1] A. D. Cronin, J. Schmiedmayer, and D. E. Pritchard, Optics and interferometry with atoms and molecules, Rev. Mod. Phys. **81**, 1051 (2009).

[2] R. Scelle, T. Rentrop, A. Trautmann, T. Schuster, and M. K. Oberthaler, Motional coherence of fermions immersed in a bose gas, Phys. Rev. Lett. **111**, 070401 (2013).

[3] M. G. Skou, T. G. Skov, N. B. Jørgensen, K. K. Nielsen, A. Camacho-Guardian, T. Pohl, G. M. Bruun, and J. J. Arlt, Non-equilibrium quantum dynamics and formation of the Bose polaron, Nature Physics **17**, 731 (2021).

[4] M. G. Skou, K. K. Nielsen, T. G. Skov, A. M. Morgen, N. B. Jørgensen, A. Camacho-Guardian, T. Pohl, G. M. Bruun, and J. J. Arlt, Life and death of the Bose polaron, Physical Review Research **4**, 043093 (2022).

[5] A. M. Morgen, S. S. Balling, K. K. Nielsen, T. Pohl, G. M. Bruun, and J. J. Arlt, Quantum beat spectroscopy of repulsive bose polarons (2023), arXiv:2310.18183 [cond-mat.quant-gas].

[6] T. Kraemer, M. Mark, P. Waldburger, J. G. Danzl, C. Chin, B. Engeser, A. D. Lange, K. Pilch, A. Jaakkola, H.-C. Nägerl, and R. Grimm, Evidence for Efimov quantum states in an ultracold gas of caesium atoms, Nature **440**, 315 (2006).

[7] M. Zaccanti, B. Deissler, C. D'Errico, M. Fattori, M. Jona-Lasinio, S. Müller, G. Roati, M. Inguscio, and G. Modugno, Observation of an Efimov spectrum in an atomic system, Nature Physics **5**, 586 (2009).

[8] C. Chin, R. Grimm, P. Julienne, and E. Tiesinga, Feshbach resonances in ultracold gases, Reviews of Modern Physics **82**, 1225 (2010).

[9] T. Tomita, S. Nakajima, I. Danshita, Y. Takasu, and Y. Takahashi, Observation of the mott insulator to superfluid crossover of a driven-dissipative bose-hubbard system, Science Advances **3**, e1701513 (2017).

[10] M. Fitzpatrick, N. M. Sundaresan, A. C. Y. Li, J. Koch, and A. A. Houck, Observation of a dissipative phase transition in a one-dimensional circuit qed lattice, Phys. Rev. X **7**, 011016 (2017).

[11] N. B. Jørgensen, L. Wacker, K. T. Skalmstang, M. M. Parish, J. Levinsen, R. S. Christensen, G. M. Bruun, and J. J. Arlt, Observation of attractive and repulsive polarons in a Bose-Einstein condensate, Physical Review Letters **117**, 055302 (2016).

[12] M.-G. Hu, M. J. Van de Graaff, D. Kedar, J. P. Corson, E. A. Cornell, and D. S. Jin, Bose polarons in the strongly interacting regime, Physical Review Letters **117**, 055301 (2016).

[13] L. A. Peña Ardila, N. B. Jørgensen, T. Pohl, S. Giorgini, G. M. Bruun, and J. J. Arlt, Analyzing a Bose polaron across resonant interactions, Physical Review A: Atomic, Molecular, and Optical Physics **99**, 063607 (2019).

[14] J. Etrych, G. Martirosyan, A. Cao, C. J. Ho, Z. Hadzibabic, and C. Eigen, Universal quantum dynamics of bose polarons (2024), arXiv:2402.14816 [cond-mat.quant-gas].

[15] N. Spethmann, F. Kindermann, S. John, C. Weber, D. Meschede, and A. Widera, Dynamics of single neutral impurity atoms immersed in an ultracold gas, Physical Review Letters **109**, 235301 (2012).

[16] T. Hewitt, T. Bertheas, M. Jain, Y. Nishida, and G. Barontini, Controlling the interactions in a cold atom quantum impurity system, Quantum Science and Technology **9**, 035039 (2024).

[17] Z. Z. Yan, Y. Ni, C. Robens, and M. W. Zwierlein, Bose polarons near quantum criticality, Science (New York, N.Y.) **368**, 190 (2020).

[18] L. Wacker, N. B. Jørgensen, D. Birkmose, R. Horchani, W. Ertmer, C. Klempt, N. Winter, J. Sherson, and J. J. Arlt, Tunable dual-species bose-einstein condensates of ^{39}K and ^{87}Rb, Phys. Rev. A **92**, 053602 (2015).

[19] M. Lysebo and L. Veseth, Feshbach resonances and transition rates for cold homonuclear collisions between ^{39}K and ^{41}K atoms, Physical Review A: Atomic, Molecular, and Optical Physics **81**, 032702 (2010).

[20] L. Tanzi, C. R. Cabrera, J. Sanz, P. Cheiney, M. Tomza, and L. Tarruell, Feshbach resonances in potassium Bose-Bose mixtures, Physical Review A: Atomic, Molecular, and Optical Physics **98**, 062712 (2018).

[21] L. J. Wacker, N. B. Jørgensen, K. T. Skalmstang, M. G. Skou, A. G. Volosniev, and J. J. Arlt, Temperature dependence of an Efimov resonance in ^{39}K, Physical Review A: Atomic, Molecular, and Optical Physics **98**, 052706 (2018).

[22] J. Söding, D. Guéry-Odelin, P. Desbiolles, F. Chevy, H. Inamori, and J. Dalibard, Three-body decay of a rubidium Bose–Einstein condensate, Applied Physics B **69**, 257 (1999).

[23] E. A. Burt, R. W. Ghrist, C. J. Myatt, M. J. Holland, E. A. Cornell, and C. E. Wieman, Coherence, correlations, and collisions: What one learns about bose-einstein condensates from their decay, Phys. Rev. Lett. **79**, 337 (1997).

[24] N. P. Mehta, S. T. Rittenhouse, J. P. D'Incao, J. von Stecher, and C. H. Greene, General theoretical description of N-body recombination, Phys. Rev. Lett. **103**, 153201 (2009).

[25] M. Mikkelsen, A. S. Jensen, D. V. Fedorov, and N. T. Zinner, Three-body recombination of two-component cold atomic gases into deep dimers in an optical model, Journal of Physics B: Atomic, Molecular and Optical Physics **48**, 085301 (2015).

[26] T. Weber, J. Herbig, M. Mark, H.-C. Nägerl, and R. Grimm, Three-body recombination at large scattering lengths in an ultracold atomic gas, Phys. Rev. Lett. **91**, 123201 (2003).

[27] J. P. D'Incao, H. Suno, and B. D. Esry, Limits on universality in ultracold three-boson recombination, Phys. Rev. Lett. **93**, 123201 (2004).

[28] K. Helfrich, H.-W. Hammer, and D. S. Petrov, Three-body problem in heteronuclear mixtures with resonant interspecies interaction, Phys. Rev. A **81**, 042715 (2010).

[29] E. Braaten and H.-W. Hammer, Efimov physics in cold atoms, Annals of Physics **322**, 120 (2007), january Special Issue 2007.

[30] B. S. Rem, A. T. Grier, I. Ferrier-Barbut, U. Eismann, T. Langen, N. Navon, L. Khaykovich, F. Werner, D. S. Petrov, F. Chevy, and C. Salomon, Lifetime of the bose gas with resonant interactions, Phys. Rev. Lett. **110**, 163202 (2013).

[31] J. Levinsen, M. M. Parish, and G. M. Bruun, Impurity in a Bose-Einstein condensate and the Efimov effect, Physical Review Letters **115**, 125302 (2015).

[32] J. Schuster, A. Marte, S. Amtage, B. Sang, G. Rempe, and H. C. W. Beijerinck, Avalanches in a bose-einstein condensate, Phys. Rev. Lett. **87**, 170404 (2001).

[33] R. Chapurin, X. Xie, M. J. Van de Graaff, J. S. Popowski, J. P. D'Incao, P. S. Julienne, J. Ye, and E. A. Cornell, Precision test of the limits to universality in few-body physics, Phys. Rev. Lett. **123**, 233402 (2019).

[34] S. Lepoutre, L. Fouché, A. Boissé, G. Berthet, G. Salomon, A. Aspect, and T. Bourdel, Production of strongly bound ^{39}K bright solitons, Phys. Rev. A **94**, 053626 (2016).

[35] G. Semeghini, G. Ferioli, L. Masi, C. Mazzinghi, L. Wolswijk, F. Minardi, M. Modugno, G. Modugno, M. Inguscio, and M. Fattori, Self-bound quantum droplets of atomic mixtures in free space, Phys. Rev. Lett. **120**, 235301 (2018).

[36] T. G. Skov, M. G. Skou, N. B. Jørgensen, and J. J. Arlt, Observation of a lee-huang-yang fluid, Phys. Rev. Lett. **126**, 230404 (2021).

[37] J. c. v. Etrych, G. Martirosyan, A. Cao, J. A. P. Glidden, L. H. Dogra, J. M. Hutson, Z. Hadzibabic, and C. Eigen, Pinpointing feshbach resonances and testing efimov universalities in ^{39}K, Phys. Rev. Res. **5**, 013174 (2023).

[38] M.-G. Hu, R. S. Bloom, D. S. Jin, and J. M. Goldwin, Avalanche-mechanism loss at an atom-molecule efimov resonance, Phys. Rev. A **90**, 013619 (2014).

CHAPTER 5

Observation of Deeply Bound Polaronic States

Spectroscopy can be utilized to probe polarons in ultracold quantum gases as presented in the previous chapter. This is further investigated in this chapter, where the focus now lies on accurate modeling of the spectral function of the polaron, to extract its energy as a function of the impurity-medium interaction strength. Additionally, a signal at lower energies than the polaron is observed and interpreted as the bipolaron response of the system.

The chapter is structured as follows: First, the ejection protocol is discussed in Sec. 5.1 in the context of recording the polaron spectrum. The theoretical spectral function of the polaron is described in Sec. 5.2 along with the necessary experimental considerations. In Sec. 5.3, the recorded ejection spectra are presented and the polaron signal is investigated, followed by an interpretation of the observed bipolaron response.

5.1 Ejection Spectroscopy

The ejection protocol used for probing the system has already been outlined in Ch. 4, but a summary is provided here. The protocol, which is illustrated in Fig 5.1, consists of two rf-pulses with a variable evolution time

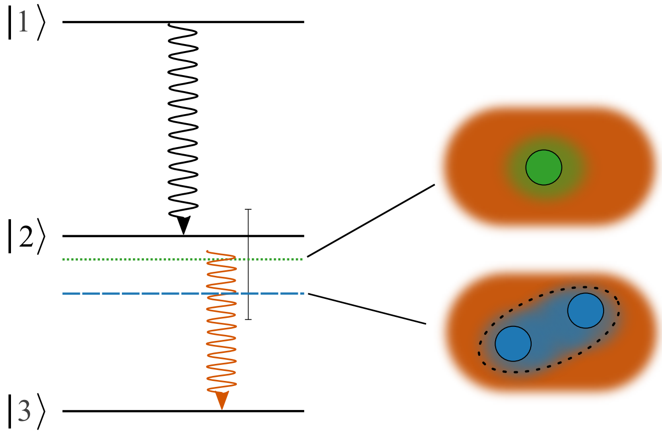

FIGURE 5.1: Overview of the relevant states within the ejection protocol for our system. The scan range of the frequency of the second rf-pulse from $|2\rangle$ to $|3\rangle$ is indicated by the vertical bar. An illustration of the energy shift of the polaron and bipolaron states is also shown. Adapted from [44].

between them. The first rf-pulse is resonant with the $|F=1,m_F=-1\rangle \equiv |1\rangle$, to $|F=1,m_F=0\rangle \equiv |2\rangle$ state transition, and ensures transfer from the medium, $|1\rangle$, to the impurity state, $|2\rangle$. The system is then allowed to evolve before probing it with the second rf-pulse (referred to as the probe pulse) that attempts to transfer the impurities to the third state, $|F=1,m_F=+1\rangle \equiv |3\rangle$. If this secondary transfer is successful, an increase in the remaining number of medium atoms in the $|1\rangle$ state is observed due to the different dominant loss mechanisms for the impurities in the $|2\rangle$ and $|3\rangle$ states (see Ch. 4). By scanning the frequency of the probe pulse across the resonance, the energy shift of the impurity state, relative to the natural transition between the $|2\rangle$ and $|3\rangle$ states, is measured, $E = E_{\text{rf}} - E_{23}$. An example of an ejection spectrum is shown in Fig. 5.2. It consists of a peak that is shifted towards negative energies, relative to the

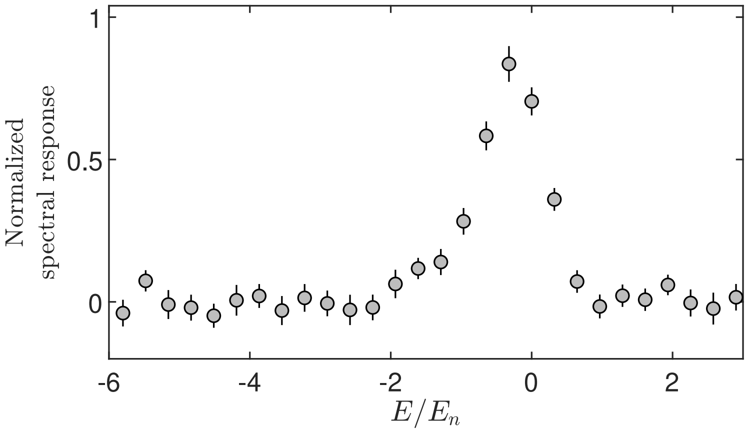

FIGURE 5.2: Ejection spectrum at $1/k_na = -1$, where the energy of the probe pulse is scanned across the resonance, $E = E_{\mathrm{rf}} - E_{23}$. A peak is observed with a clear shift from $E/E_n = 0$, as well as a tail, towards negative energies.

measured transition frequency between the $|2\rangle$ and $|3\rangle$ states for thermal atoms corresponding to $E = 0$. It also has a tail that extends towards negative energies, corresponding to the continuum of excited states.

For attractive impurity-medium interactions, $1/k_na < 0$, mediated interactions between two polarons have been predicted to lead to a bound state known as the bipolaron [58]. Ejection spectroscopy is a promising candidate for investigating such a state, given that the impurities are allowed to evolve and interact before the system is probed. This is not the case for injection spectroscopy, and so far such a state has not been observed in the experimental results using injection spectroscopy [51, 53].

The bipolaron state is also illustrated in Fig. 5.1, and is expected to be more deeply bound than the polaron. However, it is only at strong interactions, $|1/k_na| < 1$, that the binding energy of the bipolaron significantly exceeds the ground state energy of the polaron. For an ejection spectrum, the polaron and bipolaron signals will thus overlap at weak interaction strengths, but start to separate at strong interactions.

In Sec. 5.2, the spectral function for modeling the ejection spectra, such as the one observed in Fig. 5.2, is presented. In the following, the experimental considerations for optimizing the ejection protocol for the observation of bipolarons are discussed.

5.1.1 Experimental Considerations

The two rf-pulses that comprise the ejection protocol provide experimental control of the impurity concentration and evolution time of the system, as well as the spectroscopic resolution of the measurement. Both of the rf-pulses are square pulses in the time domain and thus correspond to sinc-functions in the frequency domain.

Before performing the experimental sequence outlined above, rf-spectroscopy and Rabi oscillations are performed on thermal atoms between the $|1\rangle$ and $|2\rangle$ states, and between the $|2\rangle$ and $|3\rangle$ states. Typical examples of these are shown in Fig. 5.3. The rf-spectroscopy measures the resonances of the natural transitions for an experimentally chosen magnetic field, which can also be solved through the Breit-Rabi formula [126]. This allows for extracting the magnetic field strength which is then used for calculating the impurity-medium scattering length, a, from the Feshbach resonance (see Fig. 2.1). Experimentally, the interaction strength $k_n a$ is varied, through a rather than the density, n, which also enters through $k_n = (6\pi^2 n)^{1/3}$, but is much more inconvenient to control. The Rabi oscillations, also shown in Fig. 5.3, allow for tracing the transferred fraction of atoms between each state as a function of pulse duration. This measurement is used for setting the impurity concentration, controlled by the duration of the first rf-pulse. The frequency of this pulse is set to the measured transition between the $|1\rangle$ and $|2\rangle$ state and has a short duration to keep it broad in frequency space and short with respect to the evolution time.

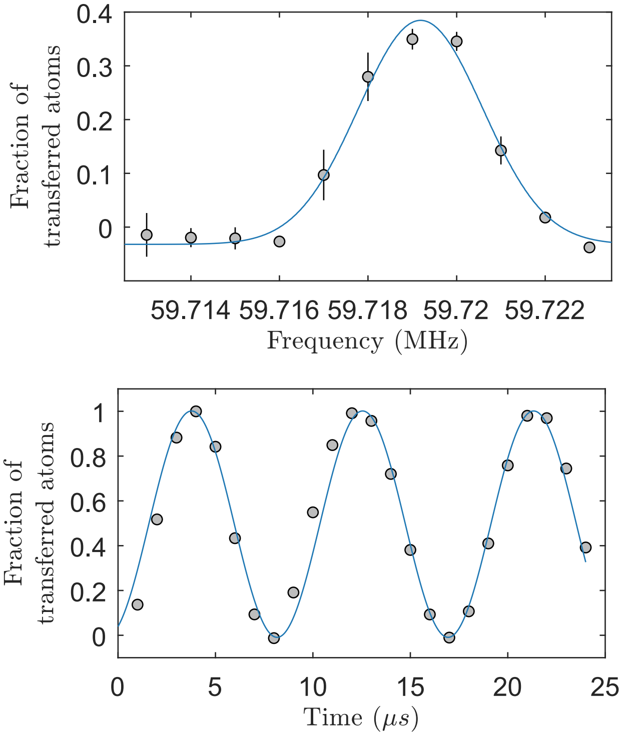

FIGURE 5.3: (top) Spectroscopy with thermal atoms where a Gaussian fit (blue line) on the observed fraction of transferred atoms (gray circles) is used for determining the resonance of the transition from the $|2\rangle$ to $|3\rangle$ states. (bottom) Observed Rabi oscillations as a function of pulse duration, fitted with a Sine (blue line) to extract the frequency. Equivalent measurements for the $|1\rangle$ to $|2\rangle$ transition is also performed.

Given that the polaron peak in the experimental signal is proportional to the number of "ejected" impurities, having a high impurity concentration will further enhance this signal. This is explicitly investigated later, where a high impurity concentration of 20% is observed to give a good signal-to-noise ratio.

During the evolution time, the impurity-medium interactions lead to the formation of polarons and possibly also bipolarons. The formation time of polarons has previously been investigated for our system, which is shortest at strong interactions where it takes 5 – 10 µs [57]. The formation time of bipolarons is unknown but presumably takes longer than for the polarons, which means that evolution times longer than 10 µs should be used. Additionally, the finite lifetime of the polaron poses a natural limit on the allowed evolution times, which at strong interactions is estimated to be around 50 µs for our system [1].

Finally, the duration of the probe pulse, on the $|2\rangle$ to $|3\rangle$ transition, sets the frequency resolution of the measurement $\sigma_f = 1/\pi T$, where σ_f is the "width" of the sinc function and T is the duration of the square pulse. This duration should be as long as possible to optimize the resolution of the polaron and possible bipolaron signals, but it is limited due to the finite lifetime of the system. A compromise between having a good spectroscopic resolution and a sufficient experimental signal is therefore necessary. The power of the rf-pulse is adjusted such that it is close to a π-pulse for the chosen duration, to maximize the transfer of the impurities to the third state $|3\rangle$.

5.2 Spectral Function

Accurate modeling of the spectral function for the polaron is necessary to evaluate the observed spectral response of the system. In particular, a potential bipolaron signal should appear as a feature not accounted for in the polaron model. Previous models for the observed spectral function of the polaron from injection spectroscopy measurements include a Gaussian fit [51] and an empirical model for the peak and many-body continuum [53]. In the case of ejection spectroscopy, the variational (Chevy) ansatz in Ref. [54] (see Ch. 2) for the description of the attractive polaron state, leads to the following rf-spectrum, $A(\omega,n)$, of the polaron

$$\begin{aligned} E_n \cdot A(\omega,n) =& 2\pi Z_\mathrm{P} \delta \left(\frac{\hbar\omega - E_\mathrm{P}}{E_n} \right) \\ &+ \theta \left(\frac{E_\mathrm{P} - \hbar\omega}{E_n} \right) \frac{3\pi}{2\sqrt{2}} Z_\mathrm{P} \left(\frac{E_\mathrm{P}}{\hbar\omega} \right)^2 \sqrt{\frac{E_\mathrm{P} - \hbar\omega}{E_n}}. \end{aligned} \tag{5.1}$$

Here, $E_n = \frac{\hbar^2 k_n^2}{2m}$ is the characteristic energy with wavenumber $k_n = (6\pi^2 n)^{1/3}$ and density n. The frequency of the probe pulse is given by ω and the quasiparticle residue and energy of the polaron are given by Z_P and E_P, respectively. Finally, the functions δ and θ are the Dirac delta and Heaviside step functions. The spectral response given by Eq. (5.1) consists of a peak described by the Dirac delta function, shifted by the polaron energy, and a continuum towards more negative energies matching the qualitative behavior of the spectrum in Fig. 5.2. Note that the tail in the above spectral function is reversed compared to that in Ref. [54]. This is due to the reversed level scheme where the ejection state lies below the impurity state and not above it, as shown in Fig. 5.1.

Based on the spectral function in Eq. (5.1), the polaron spectral response of the system can be predicted. However, due to the harmonic trapping potential, the atoms experience an inhomogenous density distribution. This means that the interaction strength $k_n a$ varies throughout the medium and the impurities are affected accordingly, with the most bound polaron at the center of the trap. Probing this system thus gives a broadened signal due to a response from impurities at different densities.

In the following, modifications to the spectral function in Eq. (5.1) are described. These include averaging the spectral function over the density distribution of the trap and a convolution with the probe pulse shape. Both of these result in a broadening of the spectral function, which can then be compared to the experimental data.

5.2.1 Trap Averaging

The spectral function for the polaron presented in Eq. (5.1) is specified at a single density, which is trap averaged by integrating it over the density distribution, $n(\mathbf{r})$, of the system,

$$\langle E_n \cdot A(E,n) \rangle = \frac{1}{N} \int \mathrm{d}^3\mathbf{r}\, n(\mathbf{r}) \cdot E_n \cdot A(E,n), \tag{5.2}$$

where N is the total atom number and $E = \hbar\omega$ is the energy probed. For a BEC in an external harmonic trapping potential, the Thomas-Fermi approximation discussed in Ch. 2 provides a good description of the density distribution, which is given by

$$n(\mathbf{r}) = n_0 \left[1 - \left(\frac{r}{R} \right)^2 \right], \tag{5.3}$$

where the peak density, n_0, is connected to the atom number through $N = 4\pi R^3 \cdot 2/15 \cdot n_0$, where R is the Thomas-Fermi radius given by Eq. (2.10). The integral variable in Eq. (5.2) is transformed to units of densities, and the trap average of the spectral function is calculated as

$$\langle E_n \cdot A(E,n) \rangle = \frac{15}{4n_0} \int_0^{n_0} dn \frac{n}{n_0} \sqrt{1 - \frac{n}{n_0}} E_n \cdot A(E,n). \tag{5.4}$$

The term, $\frac{15}{4n_0}\frac{n}{n_0}\sqrt{1-n/n_0}$, is then the general probability distribution function of the density in the Thomas-Fermi approximation. In the following, the trap averaging procedure for the polaron peak and continuum are treated separately.

Polaron peak

From Eq. (5.1), the polaron peak $A_\mathrm{P}(E,n)$ has the form

$$A_\mathrm{P}(E,n) = 2\pi Z_\mathrm{P}(n) \delta(E - E_\mathrm{P}(n)), \tag{5.5}$$

where the density dependence of the quasiparticle residue and polaron energy is shown explicitly. The polaron energy can be generalized as a function on the form $f(k_n a) = E_\mathrm{P}/E_n$, which has a dependence on the interaction strength $k_n a$. This function is taken to be the theoretical polaron energy, but it could in principle also be previous experimental results. The theoretical polaron energy is scaled by the characteristic energy E_n, but for the experimental results it is the most bound polaron that is of interest, and therefore the spectral function is scaled with the characteristic energy at the center of the trap E_{n_0},

$$E_{n_0} \cdot A_\mathrm{P}(E,n) = 2\pi Z_\mathrm{P}(n)\delta\left(E/E_{n_0} - f(k_n a)\left(\frac{n}{n_0}\right)^{2/3}\right). \tag{5.6}$$

The Dirac delta function is approximated by $\pi\delta(x) = \lim_{\eta\to 0} = \frac{\eta}{x^2+\eta^2}$, which is numerically calculated using an appropriate small value for η. Inserting the approximation for the Dirac delta function yields

$$E_{n_0} A_\mathrm{P}(E,n) = 2Z_\mathrm{P}(n)\frac{\eta}{\left(E/E_{n_0} - f(k_n a)\left(\frac{n}{n_0}\right)^{2/3}\right)^2 + \eta^2}. \tag{5.7}$$

The trap average for the peak is then performed according to

$$\langle E_{n_0} \cdot A_\mathrm{P}(E,n)\rangle = \frac{15}{4n_0}\int_0^{n_0} dn \frac{n}{n_0}\sqrt{1-\frac{n}{n_0}} E_{n_0} \cdot A_\mathrm{P}(E,n), \tag{5.8}$$

which accounts for the observed responses from the polaron peaks at different densities, each with a continuum that is considered in the following.

Polaron continuum

The continuum of the polaron spectral function $A_\mathrm{cont}(E,n)$ is given by

$$\begin{aligned} E_n \cdot A_{\mathrm{cont}}(E,n) =& \theta\left(f(k_n a) - E/E_n\right) \frac{3\pi}{2\sqrt{2}} Z_{\mathrm{P}}(n) \\ & \times \left(\frac{f(k_n a)}{E/E_n}\right)^2 \sqrt{f(k_n a) - E/E_n}. \end{aligned} \tag{5.9}$$

This is also trap averaged numerically in the same way as the polaron peak,

$$\langle E_n \cdot A_{\mathrm{cont}}(E,n)\rangle = \int_0^{n_0} dn \frac{n}{n_0} \sqrt{1 - \frac{n}{n_0}} E_n \cdot A_{\mathrm{cont}}(E,n). \tag{5.10}$$

As shown in Eq. (5.8), the peak is scaled by the energy at the center of the trap but the continuum is scaled by the energy at the local density, E_n. This means that the total trap averaged spectral function is modified to

$$\begin{aligned} \overline{A}(E) \equiv \langle E_{n_0} \cdot A(E,n)\rangle = \frac{15}{4n_0} \int_0^{n_0} dn \frac{n}{n_0} \sqrt{1 - \frac{n}{n_0}} \Big[& E_{n_0} \cdot A_P(E,n) \\ & + \frac{E_{n_0}}{E_n} E_n \cdot A_{\mathrm{cont}}(E,n) \Big]. \end{aligned} \tag{5.11}$$

Given that the initial spectral function in Eq. (5.1) is normalized, it is numerically verified that the trap averaged result from Eq. (5.11) is as well. This corresponds to the appropriate amount of spectral weight distributed in the polaron peak and continuum, which is essentially determined by the quasiparticle residue.

5.2.2 Convolution

The trap averaged spectral function from Eq. (5.11) is further convolved with the probe pulse shape. As already mentioned, this is a sinc function in frequency space, $A_{\text{sinc}}(\omega) = \sin(\omega)/\omega$. The observable effect on the spectrum is the associated intensity $(A_{\text{sinc}}(\omega))^2$. The convolution is performed numerically in terms of energies as

$$A_{\text{conv}}(E) = \overline{A}(E) * (A_{\text{sinc}}(E))^2. \tag{5.12}$$

Additionally, the spectral function is normalized after the convolution, and a scaling parameter $\mathscr{A}$ is added which is used for fitting,

$$A_{\text{tot}}(E) = \mathscr{A} \frac{A_{\text{conv}}(E)}{\int dE\, A_{\text{conv}}(E)}. \tag{5.13}$$

5.2.3 Density Estimation

The result of Eq. (5.13) can only be used to compare the polaron spectral function at the theoretical energy with the experimental data. This is due to the fact that the trap averaging procedure requires the polaron energy $f(k_n a)$ to be known for all densities. Such a comparison is only correct if the estimated density of the system is accurate.

In Ch. 4, a method for extracting the density of the system at the point of applying the probe pulse in the ejection protocol was discussed. For an ejection spectrum, it gives the number of medium atoms at the time of probing as

$$N = N_{\text{off-res}} + \eta_3 (N_{\text{on-res}} - N_{\text{off-res}}), \tag{5.14}$$

where $N_{\text{off-res}}$ and $N_{\text{on-res}}$ are the observed atom numbers off- and on-resonance. The parameter η_3 is the number of medium atoms lost per impurity due to three-body recombination, which can be extracted from the off-resonance atom number (see Ch. 4). The peak density of the condensate is then calculated in the Thomas-Fermi approximation

$$n_0 = \frac{15N}{8\pi} \left(\frac{m}{2\mu} \right)^{3/2} \overline{\omega}^3, \tag{5.15}$$

with average trap frequency $\overline{\omega} = (\omega_x \omega_y \omega_z)^{1/3}$, chemical potential μ and mass m. Besides being used for the trap average calculation, the peak density is also used for scaling the observed spectrum through the characteristic energy E_n and wavenumber k_n. This corresponds to benchmarking the experimental results against the most bound polaron at the center of the trap where E_n and the interaction strength $k_n a$ are largest.

5.2.4 Fitting Parameters

The polaron spectral function in Eq. (5.13) can now be compared to experimental results by plotting it at the theoretical polaron energy, calculated from the estimated density above. Alternatively, it can also be fitted as explained in the following.

The fitting parameter $\mathscr{A}$ allows for scaling the overall amplitude of the theoretical spectral function to match the experimental results. In order to allow for a discrepancy between the theory and experimental data, the generalized function of the polaron energy is modified to $f(k_n a) \to f(k_n a)\Delta_{E_\text{P}}$, where Δ_{E_P} is a fitting parameter. This does not change the overall scaling dependence of the polaron energy but allows a small deviation from the theoretical polaron energy.

The above modifications to the polaron spectral function, together with the fitting parameters, allow for extracting the polaron energy from the observed ejection spectra.

5.3 Experimental Ejection Spectra

In this section, the experimentally recorded ejection spectra for attractive impurity-medium interactions are presented. The above analysis provides the theoretical prediction for the spectral response of the polaron in our system, which can be used for benchmarking the experimental technique.

Afterward, the observed low-lying signal is analyzed and interpreted as a bipolaron signature.

5.3.1 Polaron Signal

Two examples of ejection spectra fitted with the polaron spectral function are shown in Fig. 5.4. These have probe pulse durations of 20 µs and 40 µs, with evolution times of 30 µs and 10 µs, respectively. The evolution time is not very well defined given that the probe pulse duration is comparable to it. This adds to an effective evolution time, which should be similar for both spectra. The polaron spectral function after only trap averaging is also shown, where both the peak and continuum are plotted separately. Most of the broadening of the signal comes from the convolution with the probe pulse, most prominently observed for the 20 µs probe pulse data. This also means that the shape and form of the peak and continuum are not resolved to a degree where they can be quantitatively described independently. However, after taking these broadening effects into account the data is well captured by the spectral function, which does display a clear shift towards negative energies as expected. Using the fitting parameter Δ_{E_P}, this shift is experimentally extracted and interpreted as the polaron energy. This is investigated as a function of the impurity-medium interaction strength and plotted in Fig. 5.4.

The extracted energies are compared to both the variational calculation for the polaron energy (see Eq. (2.18)), as well as a previous quantum Monte-Carlo (QMC) result [53]. The experimentally extracted energies are observed to follow the variational calculation even at very strong interactions, where the QMC result starts to deviate from this. The extracted polaron energy in Fig. 5.4 corresponds to the most bound polaron at the peak density, which is at the edge of the polaron peak function. After the broadening due to the probe pulse shape, this position is quite close to the maximum of the signal. Extracting the energy as the center of a Gaussian fit is therefore not far off, although, for longer probe pulse duration and/or

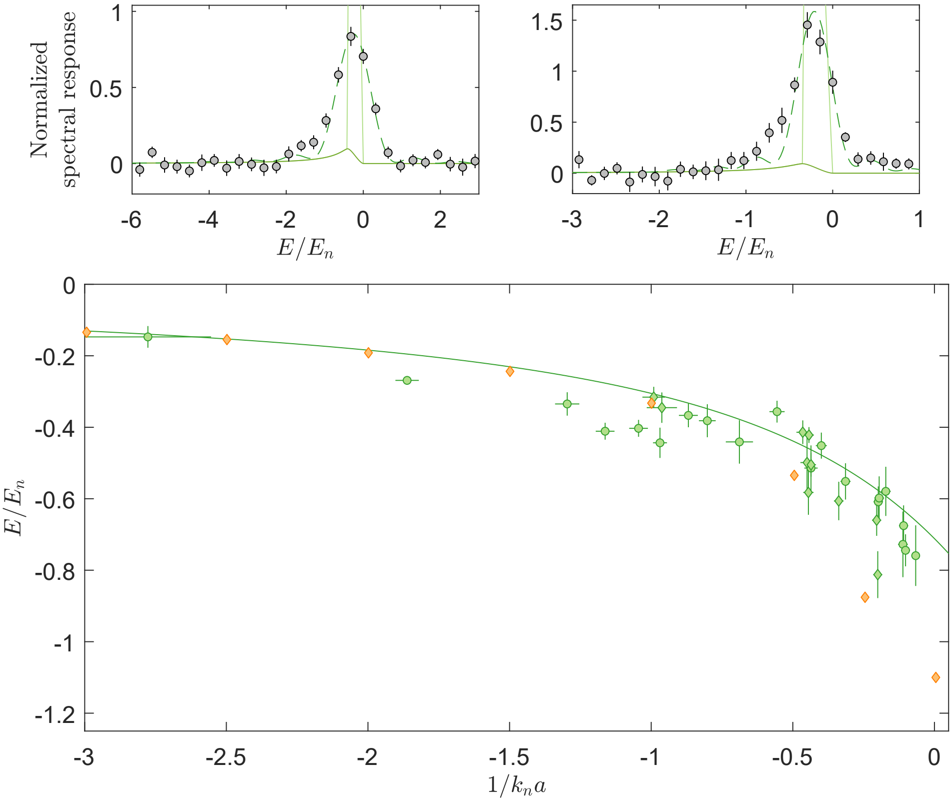

FIGURE 5.4: (top) Ejection spectra at $1/k_n a = -1$ with (left) 20 µs and (right) 40 µs probe pulse duration. The experimentally observed data (gray circles) are fitted with the polaron spectral function after trap averaging and convolution with the probe pulse shape (green dashed line). Additionally, the polaron peak (light green solid line) and continuum (dark green solid line) after only trap averaging are shown. (bottom) Extracted polaron energies from the ejection spectra as a function of the inverse interaction strength (green points), for both 20 µs (circles) and 40 µs (diamonds) probe pulse duration. These are compared to the theoretical polaron energy from Eq. (2.18) (green solid line) and results from a quantum Monte-Carlo simulation (yellow diamonds) [53]. Error bars are 1σ confidence intervals from the fitting together with propagated density uncertainties in E_n and k_n.

stronger interaction strengths, this difference is expected to be significant. Importantly, the first injection spectroscopy measurements used a simple Gaussian model for extracting the energy of the polaron [51]. This is discussed further at the end of the chapter.

Although the 40 µs duration probe pulse data provides much better resolution of the energy, its duration is comparable to the expected finite lifetime of the polaron at $1/k_n a = -1$ [1]. The lifetime further decreases as the interaction strength is increased, which means that impurities are potentially lost from the system before or during the probe pulse. This effect is strongest for the most bound polarons and would lead to a lower observed shift of the polaron peak. However, the extracted energies from both the 40 µs and 20 µs probe pulses are observed to agree with the variational calculation even at strong interactions.

The fitting of the polaron spectral function and extraction of the energy thus provides a good benchmark for modeling of the spectrum. It also builds confidence in the modification of the spectral function in terms of trap averaging, pulse shape convolution, and density estimation.

5.3.2 Bipolaron Signal

As discussed in Ch. 2, multiple theoretical predictions for the polaron at strong attractive interactions exist. In the following, I have chosen to refer to the observed low-lying feature as the bipolaron signal, to provide a consistent analysis.

As mentioned earlier, ejection spectroscopy is a good candidate for investigating mediated interactions between two polarons, due to having a free evolution time where such interactions can take place. The resulting bipolaron is expected to appear in the observed rf-spectrum as a signal at lower energies relative to the polaron signal. Multiple spectra are shown in Fig. 5.5, for both 20 µs and 40 µs probe pulse duration at varying interaction strengths. To reliably resolve both the polaron and bipolaron signal, their overlap needs to be sufficiently small. This is found to be the case

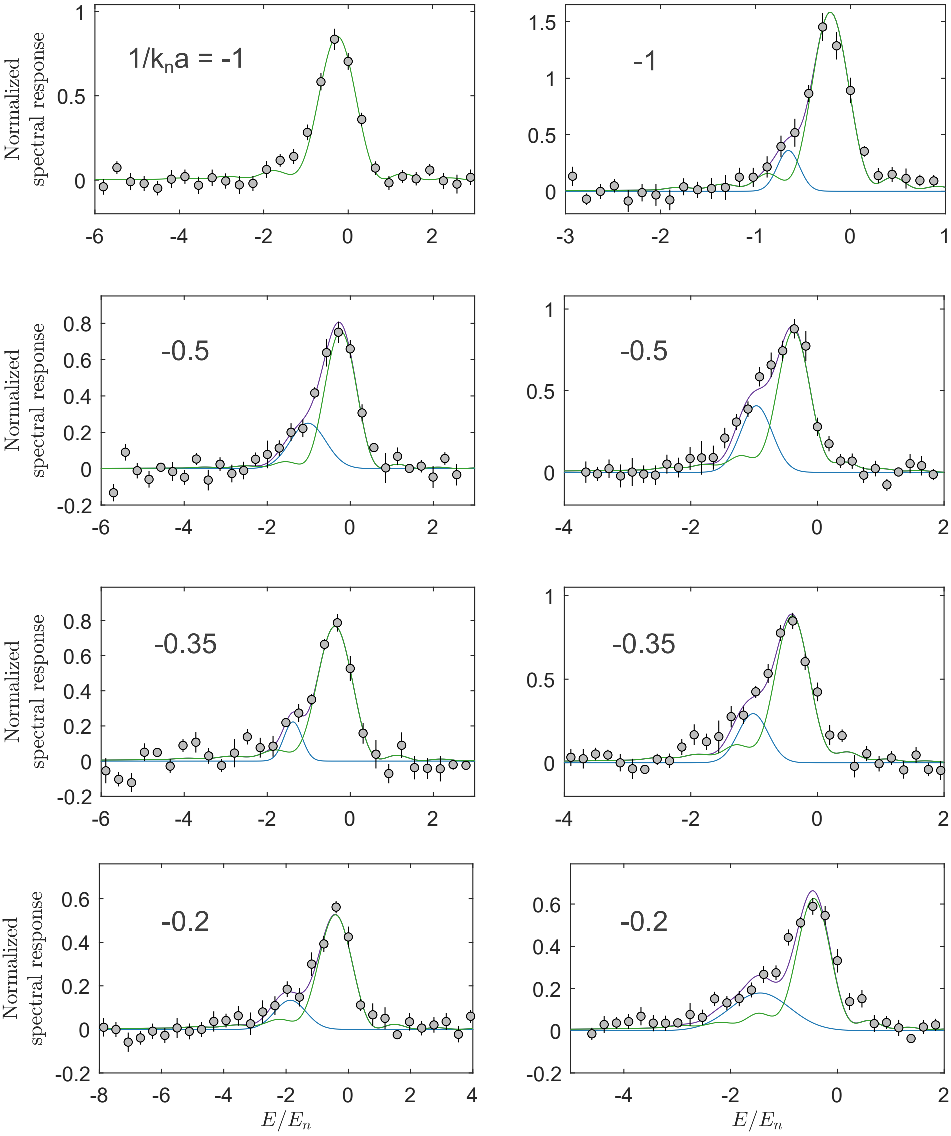

FIGURE 5.5: Ejection spectra at varying inverse interaction strength for (left column) 20 µs and (right column) 40 µs probe pulses. The experimental data points (gray circles) are fitted with the polaron spectral function (green solid line) and a Gaussian fit to the bipolaron signal (blue solid line), with the sum of these also shown (purple solid line).

at large interaction strengths, where the energy difference between the two becomes larger than the broadening of the signals due to the probe pulse duration, and thus provides a cutoff for the datasets where a bipolaron signal can be considered. For 20 µs probe pulse duration, this is found around $1/k_n a \simeq -0.6$, whereas for 40 µs it is around $1/k_n a \simeq -1$.

Throughout all measurements, a signal is constantly observed at large negative energies, which is interpreted as a bipolaron signal and fitted with a Gaussian function. This very simple fitting model is chosen since the bipolaron spectral function is not known. The observed additional spectral weight is particularly visible for the 40 µs data set, presumably as a result of its improved energy resolution.

The fitting procedure for the datasets in Fig. 5.5 consists of an initial fit for the polaron spectral function to determine the energy shift of this signal. This fit is constricted to only the data points at energies higher than $2f(k_n a)$, to avoid the polaron fit being "dragged" out to the observed bipolaron signal. This dragging effect is also considered later. The polaron energy is fixed to the fitted value and only its amplitude is allowed to vary freely, while simultaneously fitting a Gaussian to the bipolaron signal. Additionally, given that the bipolaron signal always appears at lower energies relative to the polaron signal, only the data points at negative energies are included in the fitting procedure for the Gaussian function.

Energy

The center of the fitted Gaussian is used for determining the bipolaron energy. From the discussion for the fitting of the polaron spectral function, it is clear that the extracted bipolaron energy, from the center of the Gaussian fit, is not the most bound bipolaron. However, the width of the polaron signal is primarily due to the convolution with the sinc function, which is set by the probe pulse duration. Assuming the same to be true for the bipolaron signal, this means that its trap averaged spectral function, before the convolution, is much narrower and the contribution to the spectral func-

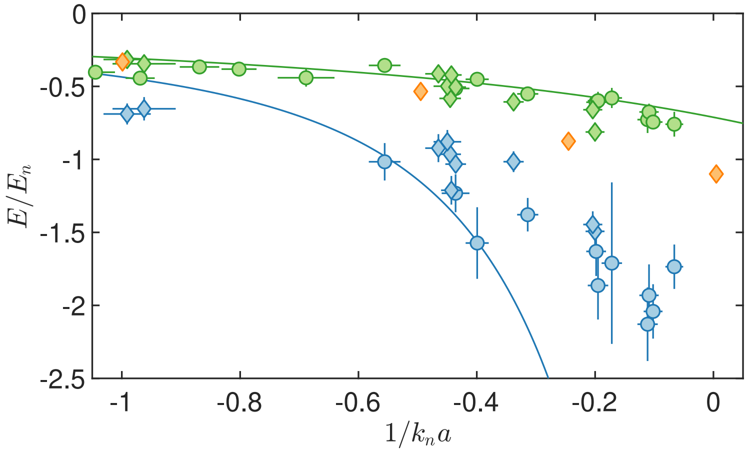

FIGURE 5.6: Extracted polaron (green points) and bipolaron energies (blue points) along with the theoretical polaron and bipolaron energy (solid green and blue line, respectively). Both the results from the 20 µs (circle) and 40 µs (diamond) datasets are shown. The results from a previous quantum Monte-Carlo calculation are also provided (yellow points) [53]. Error bars are 1σ confidence intervals from the fitting together with propagated density uncertainties in E_n and k_n.

tion from the peak density is assumed to be close to the center position of the observed peak.

The extracted bipolaron energies are shown in Fig. 5.6, together with the experimental polaron energies from Fig. 5.4 and theoretical polaron and bipolaron energies. The theoretical bipolaron energy corresponds to its binding energy and the energy of a single impurity such that it converges to the polaron energy for low interaction strengths. This is also our interpretation of the experimental ejection sequence i.e. the probe pulse disassociates the bipolaron state and ejects a single polaron into the $|3\rangle$ state. This is formally stated in terms of the detuning of the probe pulse

$$\delta_{\mathbf{k}} = E_{\mathrm{BP}} - E_{\mathrm{P},\mathbf{k}} - \epsilon_{\mathbf{k}}, \tag{5.16}$$

where $E_{\mathrm{P},\mathbf{k}}$ is the polaron energy of the remaining impurity with momentum $\mathbf{k}$ and $\epsilon_{\mathbf{k}} = \frac{\hbar^2 k^2}{2m}$ is the kinetic energy of the impurity transferred to the $|3\rangle$ state, with momentum $-\mathbf{k}$.

The extracted bipolaron energies are observed to somewhat follow the theoretical prediction for the first few points, but fall off as unitarity is approached at $1/k_n a = 0$. For the two bipolaron energy data points at $1/k_n a = -1$, the spectroscopic resolution is at its limit and some overlap between the two signals is expected, which could explain why the extracted bipolaron energies are overestimated with respect to the theory.

Evolution time

Given the discrepancies between the extracted bipolaron energies and the theoretical prediction, the signal is probed further by considering the relative spectral weight of the observed signals. This relative spectral weight is obtained from the area under the Gaussian fit relative to the sum of this and the polaron spectral function. The bipolaron spectral weight is expected to show a dependence on multiple parameters such as the evolution time, interaction strength, and impurity concentration.

The evolution time is considered first, which is varied at a fixed inverse interaction strength of $1/k_n a = -0.4$, an impurity concentration of 20%, and 20 µs probe pulse duration. The observed relative spectral weight of the bipolaron signal is shown in Fig. 5.7, where an increase for short times is observed with a slow decrease for longer times. This is indeed the overall expected behavior, i.e. the bipolarons take time to form and then eventually decays. For short evolution times the probe pulse duration is much longer than the evolution time, which results in a longer effective evolution time than depicted in Fig. 5.7. This is interpreted as the reason for the high constant signal at very short evolution times. It is also important to note

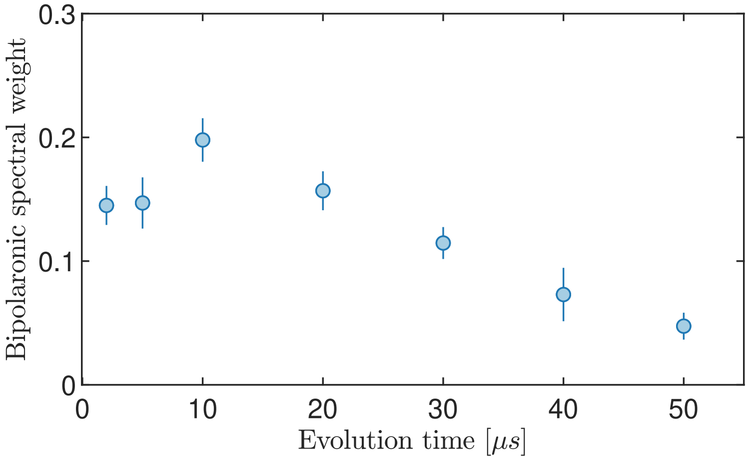

FIGURE 5.7: Relative spectral weight of the extracted bipolaron signal (blue points) as a function of evolution time of the system at fixed interaction strength of $1/k_n a = -0.4$. Error bars are 1σ confidence intervals from the fitting.

that the decrease of the observed bipolaron signal does not coincide with an equal loss of the polaron signal, which is well-defined for all the evolution times considered here.

Interaction strength

The next parameter considered is the impurity-medium interaction strength. This needs to be sufficiently high for the bipolarons to form and be experimentally distinguishable from the polaron signal. As the interaction strength is further increased, the impurities are expected to rapidly accumulate medium atoms. This increases the mediated interaction between the impurities and a larger bipolaron signal is expected to be observed. How-

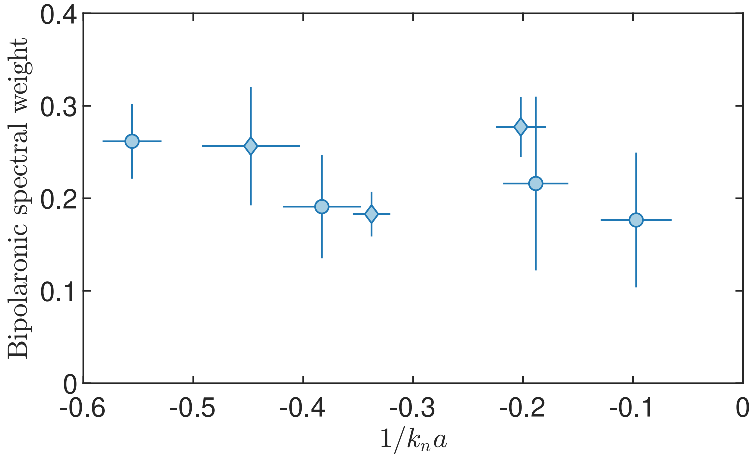

FIGURE 5.8: Relative spectral weight of the bipolaron signal for the (blue circles) 20 µs and (blue diamonds) 40 µs probe pulse data points, as a function of the inverse interaction strength between the impurity and medium atoms. For clarity, the extracted spectral weights at similar interaction strengths have been averaged (see Fig. 5.6). Error bars are 1σ confidence intervals from the fitting, together with propagated density uncertainties in k_n.

ever, plotting the extracted relative spectral weight of the bipolaron signal as a function of the inverse interaction strength in Fig. 5.8 does not provide a clear picture of this dependence, as the extracted relative spectral weights fluctuate around 0.2 and 0.3. The observed statistical uncertainties of the extracted relative spectral weights partly reflect this observed variability, but more than this it shows that the Gaussian fit is likely to over- or underestimate the bipolaron signal. This highlights the lack of fully resolving the observed bipolaron signal, as a consequence of the finite lifetime of the impurities leading to a compromise between the probe pulse duration and signal quality. The three-body losses are also increased at high interaction

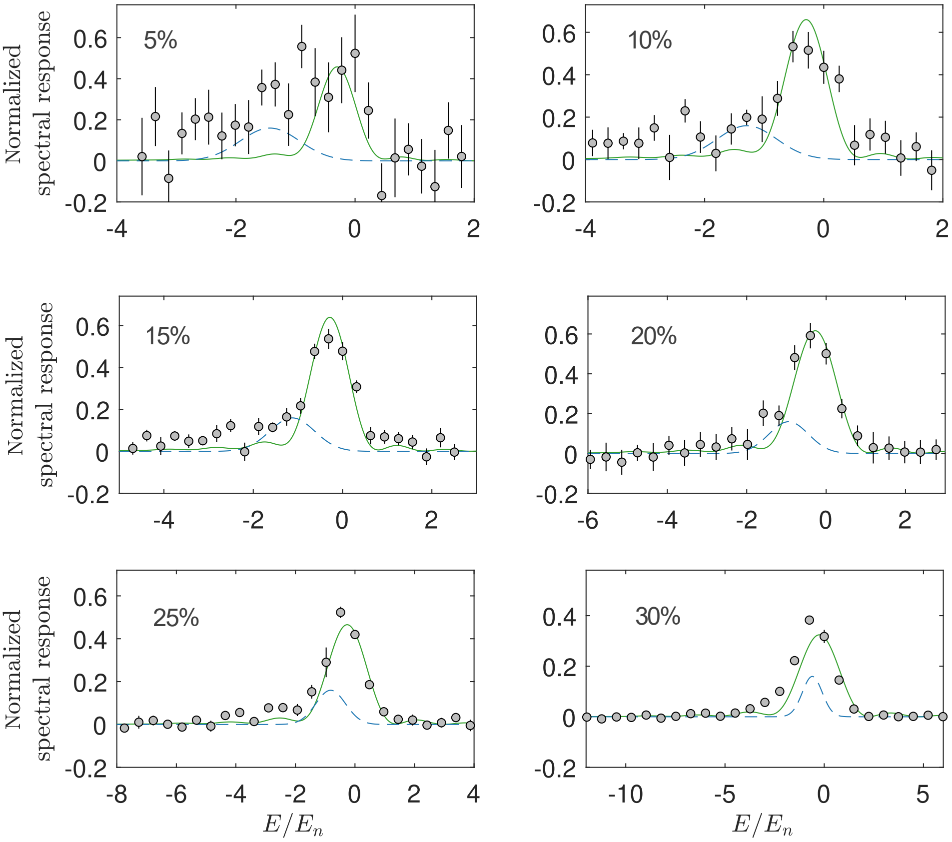

FIGURE 5.9: Ejection spectra at varying impurity concentrations and as a consequence also varying interaction strengths, ranging from $1/k_n a = -0.4$ at 5% to -0.8 at 30%. The evolution time is fixed to 20 µs for all the data sets. The polaron spectral function at the theoretical energy (green line) is fitted to the data, and the expected position of the bipolaron signal is indicated as a Gaussian centered at the theoretical bipolaron energy (blue dashed line). Note the varying x-axis scaling due to varying E_n as the impurity concentration is increased.

strengths, further affecting a possible interaction strength dependence.

Impurity concentration

Finally, the bipolaron signal dependence for varying impurity concentrations is investigated. The impurity concentration is of special interest as it is expected to strongly affect the probability of bipolaron formation. It is, therefore, a good candidate for verifying that the observed signal truly stems from a bipolaron state and is not just the result of an exotic effect from the single polaron state. However, as mentioned earlier this parameter also determines the data quality for our system. In Fig. 5.9, data sets for varying impurity concentrations from 5% to 30% are shown. The most striking effect of increasing the impurity concentration is the improvement of the quality of the data, reflected in the uncertainty of each data point. For small impurity concentrations of 5-10%, the noise in the data is significant but gets noticeably smaller as the concentration is increased and a consistent signal emerges for impurity concentrations at 15% and above. Additionally, it is seemingly improved even further towards 30%, which may prove beneficial for future investigations, although it is also close to a total loss of observed medium atoms due to three-body recombination. Additionally, at 30% one might wonder if the notion of 'impurity' starts to lose its meaning as the system approaches a balanced mixture.

Varying the impurity concentration also has the effect of varying the medium density. For the data sets in Fig. 5.9 this means that the measurements have the same impurity-medium scattering length but varying densities, resulting in different inverse interaction strengths ranging from $1/k_n a = -0.4$ at 5% to -0.8 at 30%. A direct comparison between these datasets of the extracted polaron or bipolaron features is therefore not appropriate. However, they are individually fitted with the polaron spectral function, at the theoretical polaron energy given the good agreement observed in Fig. 5.6. A Gaussian at the theoretical bipolaron energy is also plotted to indicate the expected position of the bipolaron signal. For the

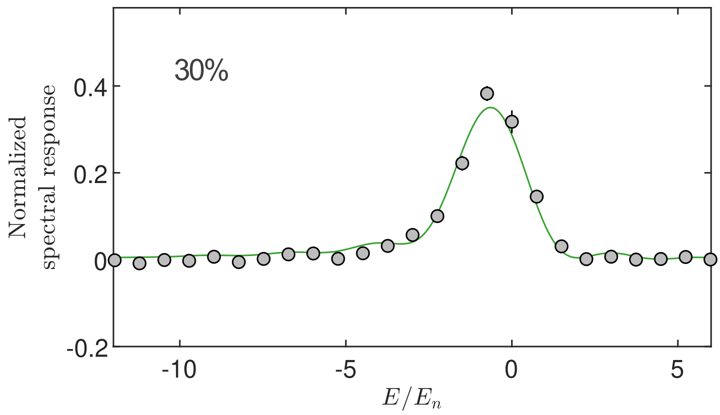

FIGURE 5.10: Ejection spectra at 30% impurity concentration, fitted with the polaron spectral function (green line) with the energy as a free parameter.

datasets below 20% concentration, the bipolaron signal should be separated from the polaron signal. For higher concentrations, the lower interaction strength means that a possible bipolaron signal significantly overlaps with the polaron signal. At the high impurity concentrations of 25% and 30%, the data also shows a clear shift in the position of the peak which coincides well with the expected position of the bipolaron signal. This specific analysis thus shows that the data can in principle accommodate a bipolaron interpretation when varying the impurity concentration.

If the energy of the polaron is chosen as a free parameter, the polaron spectral function can qualitatively describe the data alone, as shown in Fig. 5.10. To do this, the fit has to significantly shift the energy of the polaron, which is shown in Fig. 5.11 as a function of the impurity concentration. The spectrum at 5% is excluded from this analysis given the large observed noise. The energies are plotted relative to their individual theoretical polaron energies at peak density, E/E_{P}. The observed energy shift is more than twice the theoretical polaron energy for the highest impurity

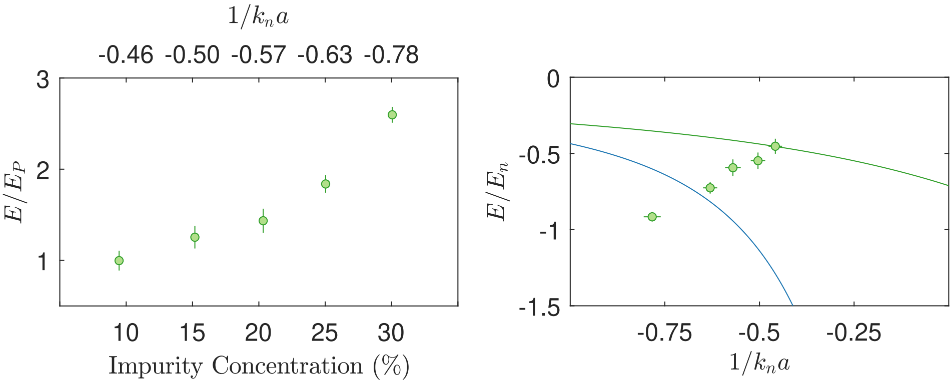

FIGURE 5.11: (left) Extracted energies for the polaron fit as a function of the impurity concentration. The extracted energies are scaled relative to their respective theoretical polaron energies. The varying interaction strength is also indicated as a secondary x-axis on top. (right) Comparison of the fitted polaron energies (green circles) and the theoretical polaron (green line) and bipolaron (blue line) energies, as a function of the inverse interaction strength. The varying impurity concentrations can be read off the left figure.

concentration. The actual fitted polaron energies are also plotted and compared to the theoretical polaron and bipolaron energies. Considering that the interaction strength decreases with increasing impurity concentration, it would be remarkable if the observed energy shift of the polaron is due to the increased impurity concentration. Thus, for the data sets in Fig. 5.5, a simple shift of the polaron energy cannot account for the observed signal. Therefore, the increase in the extracted polaron energies is attributed to an increasing overlap between the polaron and bipolaron signals, which effectively ’drags’ the polaron fit out. Recently, a shift of the polaron energy due to mediated interactions between the impurities was observed in a Fermi gas [68]. The observed shift here is much larger, which could be due to the higher compressibility of the BEC [115].

The data sets in Fig. 5.9 show that our system must utilize an impurity fraction between 15% and 30% to ensure an appropriate signal. A systematic investigation of the effect of the impurity concentration on the extracted signal at very low impurity concentrations is not feasible, as the experimental noise washes it out. Additionally, to vary the impurity concentration at fixed interaction strength, a simultaneous tuning of the scattering length is required, further complicating these measurements. Such measurements may provide further information to fully resolve the observed discrepancies regarding the impurity concentration and bipolaron signal.

Probe pulse duration

The effect of varying the probe pulse duration has already been shown in the case of 20 µs and 40 µs. For the data presented in Fig. 5.5, a more resolved bipolaron signal was observed when increasing the probe pulse duration. Here, the use of a very short probe pulse is considered instead, where the opposite behavior is expected. Ejection spectra for probe pulse durations of 10 µs, 20 µs and 40 µs, are presented in Fig. 5.12. The fitted polaron spectral function captures the width of the experimental data very well for all probe pulse durations. The changing scale of the x-axis also clearly demonstrates the improved resolution for the longer pulse durations. It is also clear that the convolution with the probe pulse shape is the dominating effect for the width of the experimental data. However, if the probe pulse duration were to be increased even further, it would become potentially longer than the lifetime of the bipolaron at high impurity-medium interactions, as observed in Fig. 5.7.

This short investigation shows that the experimental effect of the probe pulse is well understood and accounted for. It is included by convolution of the spectral function with the probe pulse shape, which provides the necessary modification for a consistent comparison with the experimental data.

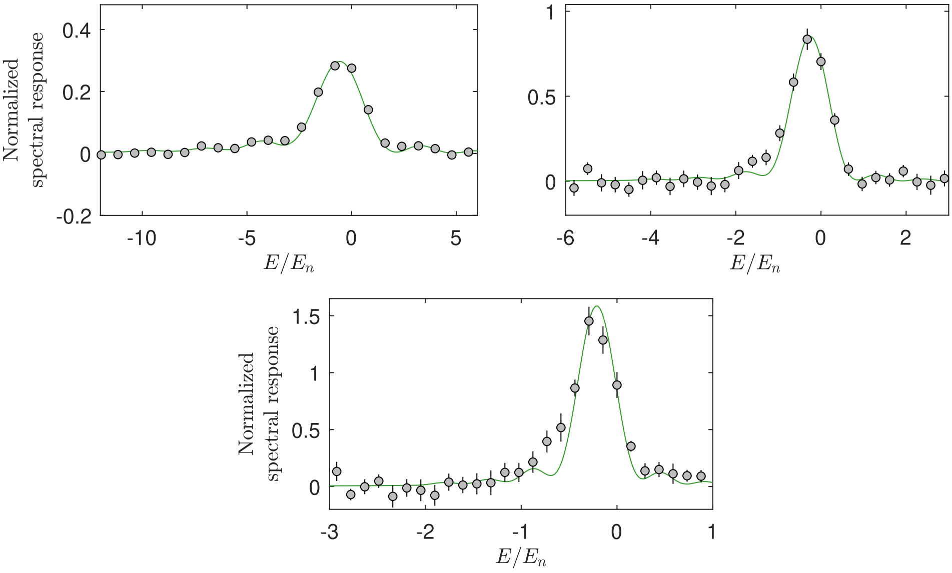

FIGURE 5.12: (top left to bottom, clockwise) Data sets with 10 µs, 20 µs, and 40 µs probe pulse duration, fitted with the polaron spectral function (green line). The changing scale of the x-axis shows how the spectroscopic resolution improves by increasing the pulse duration.

5.4 Conclusion

In this chapter, the spectroscopic results using the ejection protocol were presented for attractive impurity-medium interactions. The expected polaron spectral response was described and the experimental modifications of this signal were explored to model the experimental data. The trap averaging of the spectral function and convolution with the probing pulse led to a significant broadening. Good agreement between the calculated polaron spectral function and the experimental data was observed for all impurity-medium interaction strengths. Compared with previous injection spectro-

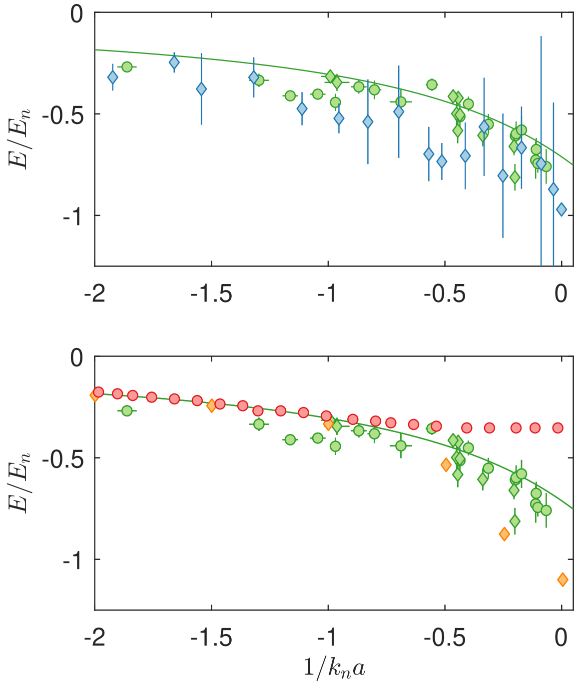

FIGURE 5.13: (top) Comparison of the extracted polaron energies for the ejection spectra presented in this thesis (green circles/diamonds) with our previous experimental injection spectroscopy results (blue diamonds) [53]. (bottom) Comparison is now made with the results of injection spectroscopy in a box potential (red circles) [106] as well as the result from the variational calculation (green solid line) and QMC results [53] (yellow diamonds).

scopy measurements [51, 53], the ejection spectroscopy results presented here offer a higher precision of the polaron energy, as is shown in Fig. 5.13. The extracted polaron energies agree with the theoretically predicted values from the variational calculation, even as unitarity is approached, although lying somewhat systematically below it. This is similar to the previous QMC results [53], which start to deviate from the variational calculation close to unitarity by as much as $-0.35E_n$. This comparison is shown in Fig. 5.13, along with recent results from Ref. [106], where injection spectroscopy on Bose polarons was performed using a box potential. The use of a box potential for trapping the atoms has the advantage that the density distribution is in principle homogeneous. This eliminates the need for trap averaging the spectral function, which is much narrower as there is only a single density in the system. The energies were extracted using a Gaussian fitting model. However, large discrepancies are observed at strong interactions, where the box potential results fall off the theoretical polaron energy around $1/k_n a = -1$ and goes to a more constant value around $-0.4E_n$. Further investigations of the Bose polaron include measuring its quasiparticle residue, which can be inferred from Rabi oscillations on the polaron [47, 104], eliminating the need for estimating it from the area of the observed spectral response. The ejection technique used here exclusively for attractive impurity-medium interactions may also be extended to repulsive interactions. This case is more complicated due to the presence of both an attractive and repulsive polaron branch, which is further investigated in Ch. 6.

For the ejection spectra in Fig. 5.5, a consistent signal at lower energies than the polaron was observed, which was interpreted as a bipolaron signal. Interpreting the spectral response of this signal is difficult since its spectral function is not known and a simple Gaussian model was applied. This analysis allowed for the extraction of the energy, which was compared to the theoretical prediction of the bipolaron in Fig. 5.6. Investigating the spectral weight of the bipolaron signal as a function of evolution time showed the expected dependence, while it was more inconclusive when varying the impurity-medium interaction strength. Finally, when varying the impurity concentration the observed behavior agreed with the bipolaron interpretation, assuming the theoretical bipolaron energy is correct. A systematic investigation of this parameter with constant interaction strength, would be the natural next step to verify the results. Another interesting parameter to vary is the medium-medium interaction strength, which is $\sim 10a_0$ for the Feshbach resonance utilized. This low value may allow for a very large accumulation of medium atoms around the impurity, compared to the case of higher repulsive medium-medium interactions.

As a final comment, it was discussed at the end of Ch. 4 that the impurity-medium-medium trimer state has an expected scattering threshold at $-3 \times 10^5 a_0$ [51, 80], which is much larger than those considered here. Theoretical work on the impact of these effects regarding an impurity immersed in a BEC has shown that the formation of large clusters of a single impurity and BEC atoms is possible [67]. Additional work has further highlighted the relation between a possible bound bipolaron state and Efimov trimers, although for the case of an impurity-impurity-medium state [59]. Importantly, these assume a large mass difference between the impurity and medium atoms, to enhance the Efimov physics. For our system, these effects are highly suppressed and can therefore not account for the observed experimental signals.

CHAPTER 6

Impurity Dynamics with Repulsive Interactions

In this chapter, results for the initial dynamics of an impurity immersed in a medium are presented. To resolve the interactions between the impurity and medium atoms at short timescales, an interferometric sequence is utilized. First, the concept of the coherence function is briefly described in Sec. 6.1. The interferometric sequence is then described in Sec 6.2 and has previously been used to investigate the Fermi polaron [55, 56], as well as the Bose polaron for attractive impurity-medium interactions [1, 57]. The results for the Bose polaron with attractive impurity-medium interactions are presented in Sec. 6.3, followed by a discussion on the theoretical description for the case of repulsive interactions. Finally, the publication for the experimental investigations of the Bose polaron for repulsive impurity-medium interactions is introduced and presented in Sec. 6.4.

6.1 Coherence Function

Many-body correlations are a central concept for the formation of polarons. In ultracold dilute gases, the equilibration of an impurity suddenly immersed in a medium is studied through the coherence function, $C(t)$. This function is connected to the time-dependent Green's function of the impurity

$$G(t) = -iC(t) = -i\langle \Psi_{\mathrm{BEC}} | \hat{c}(t) \hat{c}^{\dagger}(0) | \Psi_{\mathrm{BEC}} \rangle, \tag{6.1}$$

where Ψ_{BEC} is the wavefunction of the BEC and $\hat{c}^{\dagger}$ ($\hat{c}$) is the creation (annihilation) operator for the impurity [155]. The coherence function describes the overlap between the initial state and the time-evolved impurity state. As the system evolves, this overlap is reduced due to the scattering processes between the impurity and medium atoms, and the system is said to decohere.

The extraction of the coherence is possible through the use of an interferometric sequence, which is presented in the following section.

6.2 Interferometric Sequence

The experimental sequence starts with a ^{39}K BEC, in the $|F = 1, m_F = -1\rangle \equiv |1\rangle$ state, acting as the medium. The impurity state is given by the $|F = 1, m_F = 0\rangle \equiv |2\rangle$ state. A Ramsey-like interferometric sequence is used for the experimental observation of the coherence. It consists of two short radiofrequency (rf) pulses with a variable time between. In the original work of Ramsey [156], the rf-pulses are $\pi/2$ pulses, which results in a balanced mixture. In the context of impurity physics, only a small fraction in the impurity state is wanted and thus $\pi/7$ pulses are utilized. The general idea of the sequence is shown in Fig. 6.1: The first rf-pulse creates a superposition between the medium and the impurity state, with roughly 5% in the impurity state. The system is then allowed to evolve, during which scattering and loss processes occur. The Bloch vector starts to precess resulting in a phase, ϕ_c, and an overall shrinkage of the Bloch sphere is expected. The final rf-pulse closes the interferometric sequence and has a variable phase, ϕ, relative to the first rf-pulse, that is scanned to match the precession.

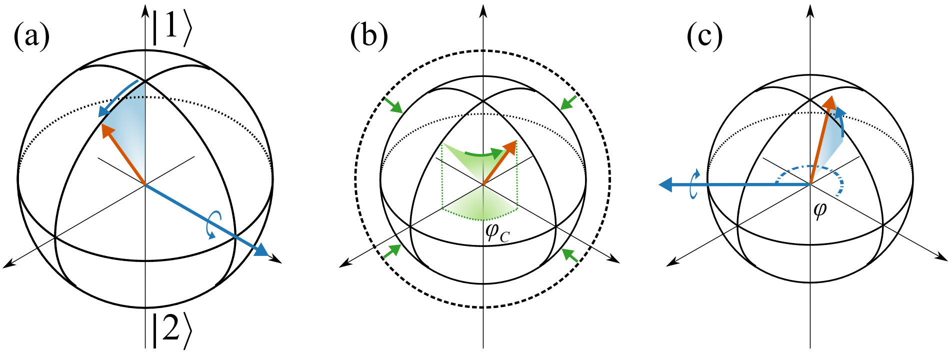

FIGURE 6.1: The interferometric sequence used in the experiment is illustrated using the Bloch sphere. The north and south poles represent the $|1\rangle$ (medium) and $|2\rangle$ (impurity) states, respectively. **a)** A short rf-pulse creates a superposition with 5% in the impurity state. **b)** During the free evolution time, the Bloch vector precesses with a phase ϕ_C due to interactions in the system and causes a shrinkage of the Bloch sphere in addition to losses. **c)** A final rf-pulse closes the interferometric sequence, with a variable phase relative to the first rf-pulse to track the precession. Adapted from [57].

The impurities that are not transferred back to the medium state after the second rf-pulse, eventually undergo three-body recombination with the medium atoms. The observable is then the number of remaining medium atoms after these losses. Examples of raw datasets are presented in Fig. 6.2, where the observed atom number shows a clear sinusoidal dependence on the phase of the second rf-pulse, as expected for the interferometric sequence. A decrease in amplitude, which is a sign of decoherence, as well as a phase shift is observed for increasing evolution times. The evolution time is scaled by the characteristic time of the system, $t_n = \hbar/E_n$, connecting it to the characteristic energy, $E_n = \hbar^2 k_n^2/2m$, and the wavenumber, $k_n = (6\pi^2 n)^{1/3}$, which are determined by the medium density, n. The sinusoidal behavior in Fig. 6.2 is modeled by $N(\phi) = N_0 - \mathscr{A}\cos(\phi - \phi_c)$,

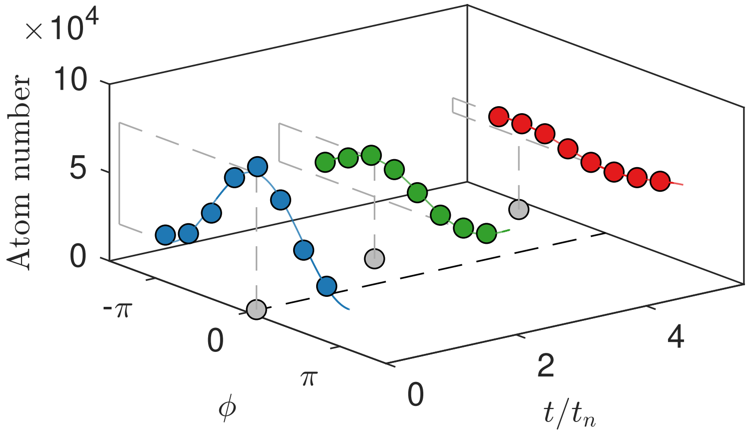

FIGURE 6.2: Observed medium atom number as a function of the phase of the second rf-pulse in the Ramsey-like sequence for three different evolution times. With increasing evolution time the amplitude of the sinusoidal signals decreases as well as acquires a phase shift, which is marked by the gray points.

which is fitted to the data to extract the amplitude $\mathscr{A}$ and phase ϕ_c. From this fit, the normalized coherence function is extracted as

$$C(t) = |\mathscr{A}(t)/\mathscr{A}(0)|e^{i\phi_c(t)}. \tag{6.2}$$

The above procedure highlights the method for tracing the amplitude and phase of the coherence function to observe the decoherence of the system as a function of time. The theoretical characteristic dynamical regimes governing the decoherence of the system are examined in the following section.

6.3 Characteristic Dynamical Regimes

The interferometric sequence described above has already been used to investigate the Bose polaron for attractive impurity-medium interactions [57]. The theoretical framework developed for understanding these results can, with some modifications, be successfully extended to the repulsive side. The results for the attractive side are therefore briefly summarized, before turning to the case of repulsive interactions.

Generally, the theoretical description of the decoherence of the system is obtained from the Fourier transform of the spectral function $A(\omega)$ of the polaron

$$C(t) = \frac{1}{2\pi} \int_{-\infty}^{+\infty} A(\omega) e^{-i\omega t} d\omega. \tag{6.3}$$

This equation can be evaluated at short times by the use of special sum rules as well as the exact result for the high-frequency tail of the spectral function [137]. Additionally, by using a diagrammatic prediction for the full spectral function, the coherence function in Eq. (6.3) can be evaluated for all times [57].

6.3.1 Attractive Interactions

For the case of attractive impurity-medium interactions, a single polaron branch exists. Distinct dynamical regimes were found in Ref. [57] that describe the decoherence of the system when the impurity is introduced to the medium. These dynamical regimes are shown in Fig. 6.3, where the vertical axis shows the evolution time and the horizontal axis shows the inverse impurity-medium interaction strength, $1/k_n a$, with the impurity-medium scattering length a. The early dynamics of the system are generally governed by two-body interactions which are dominated by the high-frequency components of the system, given by the tail of the polaron spectral function. A short-time expansion of the coherence function provides

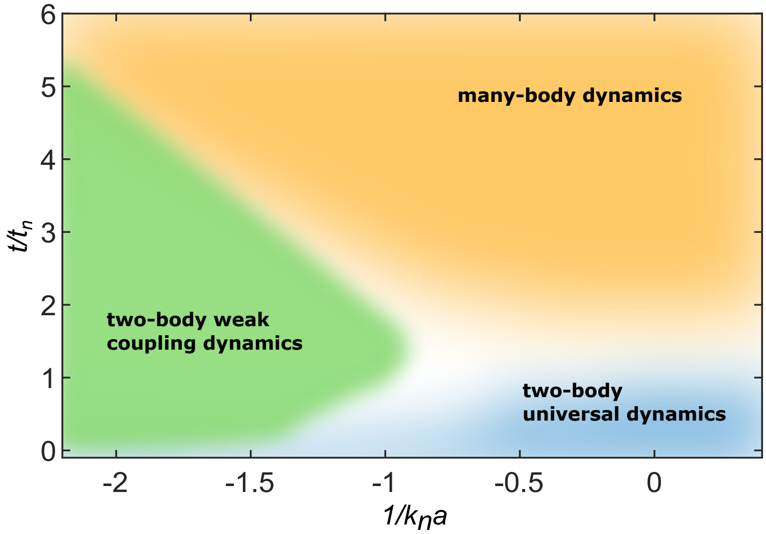

FIGURE 6.3: Dynamical regimes for the attractive Bose polaron as a function of both the inverse interaction $1/k_n a$, as well as the evolution time t/t_n. Adapted from [57].

the behavior for the two-body universal regime as [57]

$$C(t) \simeq 1-(1-i)16/9\pi^{3/2}\left(\frac{t}{t_n}\right)^{3/2}. \tag{6.4}$$

It has a characteristic scaling of $t^{3/2}$ and shows a universal behavior with no dependence on the scattering length, defining a unitarity-limited dynamical regime in Fig. 6.3. For weak interaction strengths, the dynamics transition into a two-body weak coupling regime, described by mean-field interactions. The decoherence in this regime is given by

$$C(t) \simeq 1 - iE_{\mathrm{mf}}t/\hbar - (1+i)\left(\frac{t}{t_w}\right)^{1/2}, \tag{6.5}$$

where $E_{\mathrm{mf}} = 4\pi\hbar^2 na/m$ is the mean field energy and characteristic time scale $t_w = m/32\pi\hbar n^2 a^4$.

Eventually, the dynamics enter the many-body regime, which is described by the full spectral function of the polaron, containing a peak as well as a continuum of excitations (see Chap. 2). In Ref. [57], this was calculated from a nonpertubative diagrammatic approach in the so-called ladder approximation, which yielded the following spectral function

$$A(\omega) = Z_{\mathrm{P}} 2\pi\delta(\omega - \omega_{\mathrm{P}}) + 8\pi\frac{\hbar^{3/2} n}{m^{3/2}\omega^{5/2}} \frac{\Theta(\omega - \omega_{\mathrm{P}})}{1 + \frac{\hbar}{ma^2\omega}(1 - \frac{4\pi\hbar na}{m\omega})^2}. \tag{6.6}$$

Here, Z_{P} is the quasiparticle residue, $\hbar\omega_{\mathrm{P}}$ is the polaron energy, and δ is the Dirac delta function. It is similar to the spectral function from the variational calculation presented in Chap. 5. The first term corresponds to the ground state of the polaron and the second term is the continuum of high-momentum impurity states and Bogoliubov excitations. The step function $\Theta(\omega - \omega_{\mathrm{P}})$ is introduced to move the continuum above the polaron peak to make it self-consistent. The spectral function has a high energy tail scaling as $\omega^{-5/2}$, which connects to the $t^{3/2}$ decay of the coherence function in the universal dynamical regime. For weak interactions the second term in the denominator becomes relevant, resulting in the transition from the universal to weakly interacting two-body dynamics. For strong interactions, this transition is suppressed, as also illustrated in Fig. 6.3.

The decoherence in the two-body dynamical regimes, as well as in the many-body regime, are thus fully encapsulated in Eq. (6.6). In Ref. [57], it was compared to the extracted coherence amplitudes from the interferometric sequence and observed to capture the decoherence for all times as shown in Fig. 6.4, for both strong and weak interactions. By comparing it

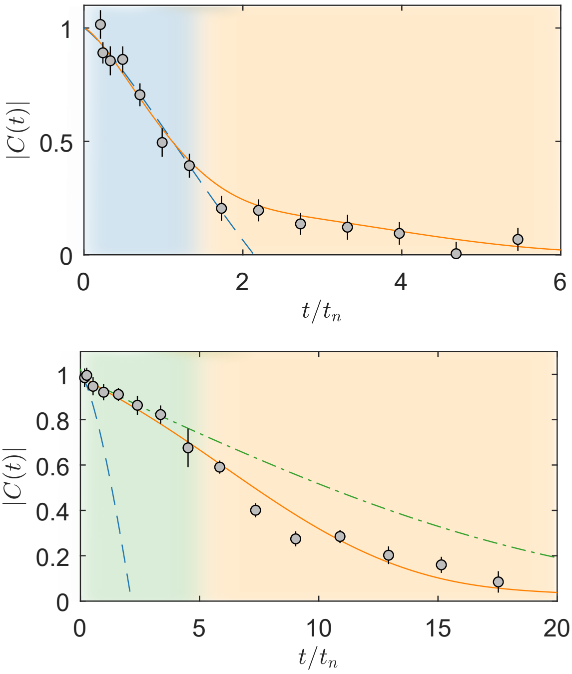

FIGURE 6.4: Coherence amplitude as a function of time for (top) strong ($1/k_na = -0.01$) and (bottom) weak ($1/k_na = -2$) interactions. The two-body universal regime is given by the blue dashed line along with the blue-shaded region. The weak two-body dynamical regime is given by the green dot-dashed line and green-shaded region. The many-body regime is given the orange line and orange-shaded region. Adapted from [57].

with the two-body universal and weak predictions in Eq. (6.4) and (6.5), the crossover times between the dynamical regimes were extracted.

For comparing the models with the experimental data in Fig. 6.4, the density distribution due to the harmonic trapping potential has to be accounted for. The harmonic potential induces an inhomogeneous density distribution which modifies the observed decoherence of the system. This is accounted for by trap averaging the coherence function similar to how the spectral function was trap averaged in Chap. 5, Eq. (5.4). Additionally, three-body recombination losses are included through an empirical exponential decay model as also discussed in Chap. 4. This leads to a global loss of coherence, modeled as $C(t) \to C(t)\exp(-\Gamma t)$, where Γ is the loss rate [57]. In light of the results in Chap. 4, it would be more appropriate to describe the losses through the three-body loss rate coefficient K_3. However, good quantitative agreement between theory and experiment is still observed using the empirical model.

For attractive interactions, the dynamical regimes are thus well understood and the extracted experimental coherences match the theoretical predictions quantitatively.

6.3.2 Repulsive Interactions

In the case of repulsive impurity-medium interactions, the system is inherently more complicated. Two distinct quasiparticle states exist, referred to as the attractive and repulsive polaron branches (see Chap. 2). To probe the system, the interferometric sequence described in Sec. 6.2 is again utilized and both branches are initially populated. Upon closing the sequence, an interference effect between the two polaron states is expected. This is observed as a quantum beat effect in the extracted coherence function, which contains information of both branches. Such a quantum beat effect has been observed for the case of the Fermi polaron [56], but not for the Bose polaron until now.

The two-body universal regime described in Eq. (6.4) for attractive interactions, is also expected to be valid for repulsive interactions. However, the presence of the attractive polaron state is accounted for by utilizing a second-order expansion of the coherence function

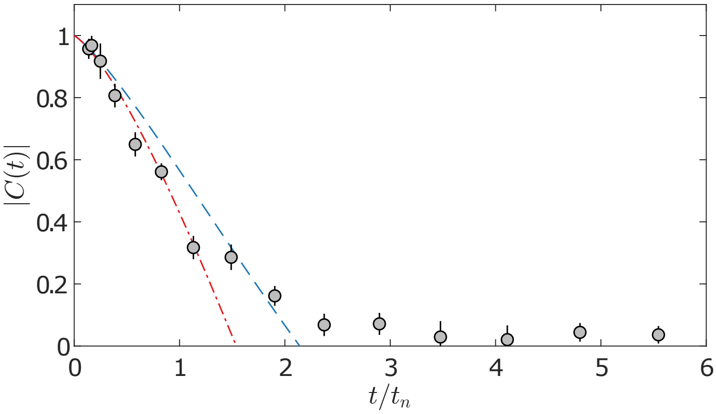

FIGURE 6.5: Observed coherence amplitude, $|C(t)|$, (gray circles) at an inverse interaction strength of $1/k_n a = +0.3$. The universal behavior (blue line) described by Eq. (6.4), gives a slower decoherence compared to Eq. (6.7) which has the second-order corrections (red line). Adapted from [1].

$$C(t) \simeq 1 - (1-i)k_{3/2}\left(\frac{t}{t_n}\right)^{3/2} - k_2\left(\frac{t}{t_n}\right)^2, \tag{6.7}$$

with $k_{3/2} = 16/9\pi^{3/2}$ and $k_2 = Z_{\mathrm{P}}(E_{\mathrm{P}}/E_n)^2/2 - 4/(3\pi k_n|a|)$ [1]. The former of these represents the universal behavior, while the latter is the second-order contribution from the peak and tail of the attractive polaron, with quasiparticle residue Z_{P} and energy E_{P}. This correction is entirely real and therefore only affects the coherence amplitude. The coherence function is also trap averaged and three-body losses are included similar to the case for attractive interactions. The second-order expansion is observed to account for the faster initial decoherence observed at strong repulsive interactions, as shown in Fig. 6.5.

For the weak-coupling regime, the full form of the coherence function

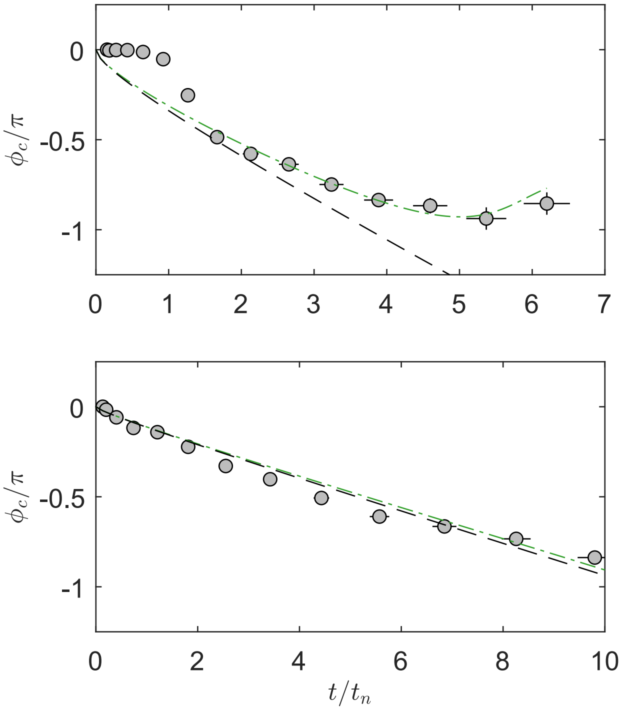

FIGURE 6.6: Extracted experimental data points for the phase evolution (gray circles) for both (top) intermediate and (bottom) weak interaction strengths at $1/k_n a = +0.7$ and $+1.5$. The data is compared with the coherence function in the weak-coupling regime given by Eq. (6.8) (green line), and the first-order expansion (black line).

is utilized [155],

$$C(t) = e^{-iE_{\mathrm{mf}}t/\hbar} e^{-(1+i)(t/t_w)^{1/2}}. \tag{6.8}$$

The first-order expansion of this equation is equal to Eq. (6.5), which captured the observed decoherence in the weak-coupling regime for attractive interactions. For repulsive interactions, the full exponential form given above is found to be essential for describing the phase evolution of the coherence function. This is highlighted in Fig. 6.6 at intermediate and weak interaction strengths. For intermediate interaction strengths, the upswing observed in the extracted phase evolution is exactly captured only by the full form provided by Eq. (6.8). For weaker interaction strengths, the phase evolution is observed to agree with the first-order expansion.

In contrast to the case of attractive interactions, the diagrammatic prediction that led to the spectral function in Eq. (6.6) does not give a good quantitative description when applied to the repulsive side. Presumably, the reason for this is that it does not describe the repulsive polaron adequately. However, it is still expected to give a qualitative description of the system, which merits the use of an empirical model to account for the presence of the two quasiparticle states,

$$C(t) \simeq Z_g \exp(-iE_g t/\hbar) + Z_r \exp(-i(E_r/\hbar - i\Gamma_r/2)t). \tag{6.9}$$

The first and second terms describe the attractive and repulsive polaron, respectively, each with a residue and energy. Additionally, due to the inherently unstable nature of the repulsive polaron, a damping term, $\exp(-\Gamma_r/2t)$, is introduced. This model is only expected to describe the system beyond the universal regime, given by the timescale $t_a = ma^2/\hbar$. Additionally, at strong interaction strengths the repulsive polaron is no longer well defined and the above model breaks down.

This section has thus introduced the models describing the decoherence of our system. Importantly, the similarities and differences in the case of attractive and repulsive impurity-medium interaction strengths were highlighted. This connects to the following section, where repulsive interactions are investigated further.

6.4 Quantum Beat Spectroscopy of Repulsive Bose Polarons

The publication presented in the following [2] investigates the early dynamics of the Bose polaron for repulsive interactions between the impurity and medium. The system is investigated using the Ramsey-like interferometric sequence described in Sec. 6.2. A single dataset has previously been recorded at strong repulsive interactions where no quantum beat was observed [1].

6.4.1 Results

In the following publication [2], the interferometric sequence is used to extract the coherence function of the system as a function of time. The behavior of both the coherence amplitude and phase, are well captured by the early universal dynamics and observed to transition into the weak-coupling regime. The crossover time associated with this transition is extracted as a function of impurity-medium interaction strength and excellent agreement with a theoretical prediction is observed.

For intermediate to weak interactions, a clear quantum beat signal is observed in the coherence amplitude. The energy difference between the two polaron branches is extracted by applying a phenomenological model for the coherence function. Additionally, the energy of the repulsive branch is independently extracted from the observed linear evolution of the coherence phase in the weak-coupling regime. Putting these together, the energies of both branches are extracted and compared to theoretical predictions. In the case of the attractive branch, the extracted energies do not allow for a distinction between the attractive polaron state and the molecular state. The extracted energies for the repulsive branch lie systematically above the mean-field prediction and fluctuate around a quantum Monte-Carlo (QMC) simulation.

6.4.2 Outlook

The interaction strengths investigated in this publication [2] are primarily focused on intermediate to weak interactions. This is due to the increased decoherence effects for the repulsive branch when approaching unitarity at $1/k_n a = 0$, where full decoherence is reached before the quantum beat signal is expected to appear. From the depicted dynamical regimes in Fig. 3 of the manuscript, a transition from the weak-coupling dynamics is expected for sufficiently long times. Such a transition occurs due to the inherent instability of the repulsive polaron branch, which can decay down into the attractive branch. This transition is expected to manifest itself in the phase evolution at long times, where it should go to positive values.

The quantum beat signal is also only visible for the coherence amplitude, although expected to appear in the phase evolution as well. However, the oscillations for the phase are predicted to be much smaller than those for the amplitude, requiring a high-precision measurement for observation. Such features may be more prominent when confining the atoms in a box potential [106].

The discrepancies of the repulsive polaron branch discussed in Chap. 2 are still not fully resolved. Although the results presented here agree with the QMC results, the difference between the theoretical predictions is small, and high-precision measurements are necessary.

6.4.3 Publication

For the following publication [2], I was part of designing and planning the experiment. I also performed the data analysis, made the figures, and wrote the first draft of the article. For the experimental part of the data analysis section in the supplementary information, I performed the data analysis, wrote the draft, and made the figures.

This article has been submitted to Physical Review Letters under the American Physical Society organization and is currently under review.

Quantum beat spectroscopy of repulsive Bose polarons

A. M. Morgen,[1] S. S. Balling,[1] K. Knakkergaard Nielsen,[2] T. Pohl,[1,3] G. M. Bruun,[1] and J. J. Arlt[1]
[1]*Center for Complex Quantum Systems, Department of Physics and Astronomy, Aarhus University, Ny Munkegade 120, DK-8000 Aarhus C, Denmark*
[2]*Max-Planck Institute for Quantum Optics, Hans-Kopfermann-Str. 1, D-85748 Garching, Germany*
[3]*Institute for Theoretical Physics, Vienna University of Technology, Wiedner Hauptstraße 8-10, 1040 Vienna, Austria*
(Dated: June 28, 2024)

The physics of impurities in a bosonic quantum environment is a paradigmatic and challenging many-body problem that remains to be understood in its full complexity. Here, this problem is investigated for impurities with strong repulsive interactions based on Ramsey interferometry in a quantum degenerate gas of ^{39}K atoms. We observe an oscillatory signal that is consistent with a quantum beat between two co-existing coherent quasiparticle states: the attractive and repulsive polarons. The interferometric signal allows us to extract the polaron energies for a wide range of interaction strengths, complimenting earlier spectroscopic measurements. We furthermore identify several dynamical regimes towards the formation of the Bose polaron in good agreement with theory. Our results improve the understanding of quantum impurities interacting strongly with a bosonic environment, and demonstrate how quasiparticles as well as short-lived non-equilibrium many-body states can be probed using Ramsey interferometry.

As famously argued by Landau, a bare impurity particle smoothly evolves into a quasiparticle as the interaction with a surrounding quantum environment is adiabatically increased. Whereas the concept of quasiparticles was originally developed to understand the motion of electrons in solids [1], it now has a much broader scope and forms an incredibly successful platform for understanding strongly interacting quantum many-body systems [2–6].

Ultracold quantum gas experiments have in recent years improved our understanding of quasiparticles, as they allow one to perform Landau's gedanken experiment by tuning the interaction strength between an impurity atom and a surrounding quantum gas. This has led to the observation of the Fermi polaron [7–9], whose low-temperature properties are now well understood theoretically [10–12]. Furthermore, its non-equilibrium formation dynamics [13, 14] and mediated interactions between two Fermi polarons [15] have been observed. There is also strong experimental evidence for the Bose polaron with an energy [16–19] and formation dynamics [20, 21] that matches theoretical predictions well for attractive interactions. For repulsive interactions, the spectroscopic measurements are generally complicated with broader signals due to damping, the possible presence of few-body bound states, and a many-body continuum. Except in the perturbative regime [22, 23], there are indeed many different theoretical predictions, reflecting the richness of the problem [24–35].

In this Letter, we use Ramsey interferometry to probe the non-equilibrium dynamics of impurities in a weakly interacting Bose-Einstein condensate (BEC) for repulsive interactions. The underlying method is illustrated in Fig. 1. We observe a fast initial decay and a revival in the amplitude of the oscillatory interferometric signal. This revival corresponds to a quantum beat, indicating the presence of two states, which we refer to as the repulsive and attractive branches. The interferometric measurements allow for a characterization of the energy of these branches as a function of interaction strength. Based on the initial decay, several non-equilibrium dynamical regimes are identified and explained theoretically. These interferometric results provide valuable information on impurity dynamics and the energy of the Bose polaron for strong and repulsive interactions, complimenting previous spectroscopic measurements [16, 19].

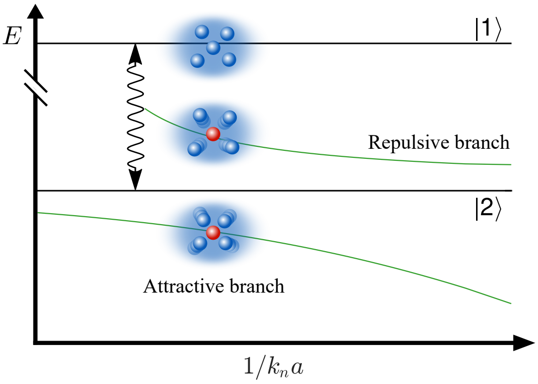

FIG. 1. Illustration of the employed Ramsey interferometry method and a simplified energy landscape of the system as a function of inverse interaction strength $1/(k_n a)$. A first radio frequency (rf) pulse (black arrow) is applied to a Bose-Einstein condensate (BEC) in the initial electronic state $|1\rangle$ (blue dots), which generates a small admixture in the impurity state $|2\rangle$ (red dots). Its interaction with the background BEC results in attractive and repulsive Bose polaron branches (green lines). A second rf pulse closes the interferometric sequence. The presence of two polaronic branches leads to the observation of a beat signal in the amplitude of the oscillatory interferometer output.

The experiment is performed with ^{39}K atoms in an optical dipole trap [36] and follows the same procedure as the investigations for attractive impurity-medium interactions [20]. The medium is a BEC in the $|F = 1, m_F = -1\rangle \equiv |1\rangle$ hyperfine state, where F and m_F denote the total angular momentum quantum number and its projection, respectively. The $|F=1,m_F=0\rangle \equiv |2\rangle$ hyperfine state constitutes the impurity state. The interaction between atoms in these two states is characterized by the scattering length, a, which can be controlled with a magnetic Feshbach resonance at $113.8G$ [37, 38]. As a result, the interaction strength $k_n a$ can be tuned at will from attractive, $k_n a < 0$, to repulsive, $k_n a > 0$, interactions, where $k_n = (6\pi^2 n_B)^{1/3}$ is determined by the average density, n_B, of the BEC. The typical energy scale of the system is given by $E_n = \hbar^2 k_n^2/(2m)$, with the mass m of ^{39}K, which also provides the characteristic timescale $t_n = \hbar/E_n$.

The interferometric sequence is initiated by a radio frequency (rf) pulse on resonance with the atomic transition between the $|1\rangle$ and $|2\rangle$ states [39], which produces a small 5% coherent admixture of the impurity state. Subsequently, the system evolves at the chosen interaction strength $k_n a$ for a variable time, t, until a second rf pulse with a variable phase ϕ between $-\pi$ and π is applied. We extract the signal from the loss of atoms due to three-body recombination, involving two condensate atoms and one impurity. The final number of atoms in the BEC has a sinusoidal dependence on the phase of the second rf pulse, which we parametrize as $N(\phi) = N_0 - \mathscr{A}\cos(\phi - \phi_c)$. The normalized coherence function is then given by, $C(t) = |\mathscr{A}(t)/\mathscr{A}(0)|\, e^{i\phi_c(t)}$, which corresponds to the time-dependent Green's function of the impurity, $G(t) = -iC(t) = -i\langle\Psi_{\mathrm{BEC}}|\,\hat{c}(t)\hat{c}^\dagger(0)\,|\Psi_{\mathrm{BEC}}\rangle$, with the state of the BEC $|\Psi_{\mathrm{BEC}}\rangle$, and the creation operator for the impurity, $\hat{c}^\dagger$ [14, 20].

The observed coherence amplitude and phase evolution are shown in Fig. 2 for three interaction strengths on the repulsive side of the resonance, displaying a number of striking features. The coherence amplitude shows a fast initial decay and a clear revival for intermediate and weak interaction strengths in Figs. 2 (c) and 2 (e). The phase initially increases and then reverses on a characteristic timescale, in Fig. 2 (d), indicating the crossover between different dynamical regimes.

Importantly, the dynamics entails the population of a continuum of states, which together with decoherence effects in the system, leads to a decrease in the coherence amplitude. On top of this, the energy difference between the attractive and repulsive branches (see Fig. 1) leads to a quantum beat signal. In the following, the results shown in Fig. 2 are discussed in detail, and the energies of the attractive and repulsive branches are inferred from the signal.

Theoretically, the coherence function can be obtained from a Fourier transform of the spectral function. At short times, an expansion in orders of t/t_n yields

$$C(t) = 1 - (1-i)k_{3/2}\left(\frac{t}{t_n}\right)^{3/2} - k_2\left(\frac{t}{t_n}\right)^2, \qquad (1)$$

valid for times $t \ll t_a = ma^2/\hbar$. The second term is a consequence of unitarity-limited two-body interactions [41] with the universal constant $k_{3/2} = 16/(9\pi^{3/2})$ [20, 42]. The third term is an approximate second-order correction with $k_2 = \left(Z_g\,(E_g/E_n)^2/2 - 4/(3\pi k_n|a|)\right)$, which takes the attractive polaron with energy E_g and residue Z_g, as well as the high-frequency tail of the spectral function [21] into account.

The measured coherence function in Figs. 2 (a) and 2 (b) for strong repulsive interactions $1/(k_n a) = 0.4$ indeed agrees well with Eq. (1) at short times, as was also observed for attractive interactions [21]. We are, thus, able to quantitatively account for both the fast initial decay of the coherence amplitude as well as the initial positive phase evolution [43]. At intermediate interaction strengths of $1/(k_n a) = 0.7$ in Figs. 2 (c) and 2 (d), similarly good agreement is obtained for short times, showing the presence of a universal regime, where Eq. (1) is valid, also in this case. For weak interactions at $1/(k_n a) = 1.5$, shown in Figs. 2 (e) and 2 (f), the universal regime contains only a few data points, since $t_a = 0.2t_n$.

For intermediate to weak interactions, the attractive polaron state lies close to the molecular state, whose energy to first order is given by $-\hbar^2/ma^2$. Therefore, the quantum beat signal between the two branches enters the dynamics on the same timescale, $t_a = ma^2/\hbar$, as the system exits the unitarity-limited regime [40]. As a result, we expect a dynamical regime described by weak coupling dynamics superimposed with quantum beats after $t = t_a$, which is qualitatively different from the case of attractive interactions, $1/(k_n a) < 0$, where no beating is observed. The weak coupling dynamics is to a good approximation described by

$$C(t) = e^{-iE_{\mathrm{mf}}t/\hbar}e^{-(1+i)(t/t_w)^{1/2}}. \qquad (2)$$

In this case the dynamics is governed by the mean-field phase evolution with $E_{\mathrm{mf}} = \frac{4\pi\hbar^2 a n_B}{m}$, and the coherence decays on an interaction strength dependent timescale $t_w = \frac{m}{32\pi\hbar n_B^2 a^4}$ [44], following a stretched-exponential form.

For longer times, the measured coherence amplitude and phase in Figs. 2 (c) and 2 (d) both agree well with this prediction, without, however, capturing the crossover from the initial dynamics or the beat signal. This is expected since Eq. (2) does not include the low-lying attractive polaron branch.

To examine the crossover in detail, the associated crossover time is extracted from the coherence phase [45]. We pinpoint the time at which the experimentally extracted coherence phase becomes closer to the result of Eq. (2) rather than Eq. (1). The crossover time is identified with the time between this and the previous data point. The extracted times are presented in Fig. 3, along with the expected dynamical regimes. The extracted crossover timescale is in very good agreement with the transition between unitarity-limited dynamics (blue region) and weak-coupling beating dynamics (orange region), set by the timescale $t_a = ma^2/\hbar$ for $1/(k_n a) > 0.5$. This shows the existence of universal behavior at short times for all interaction strengths, extending the result in Ref. [20] to repulsive interactions.

For strong interactions, there is no regime where Eq. (2) is accurate. Instead, the short-time unitarity-limited dynamics given by Eq. (1) is expected to transition directly to many-body dynamics for later times, consistent with the case of strong attractive interactions [20]. Theoretically, it is expected

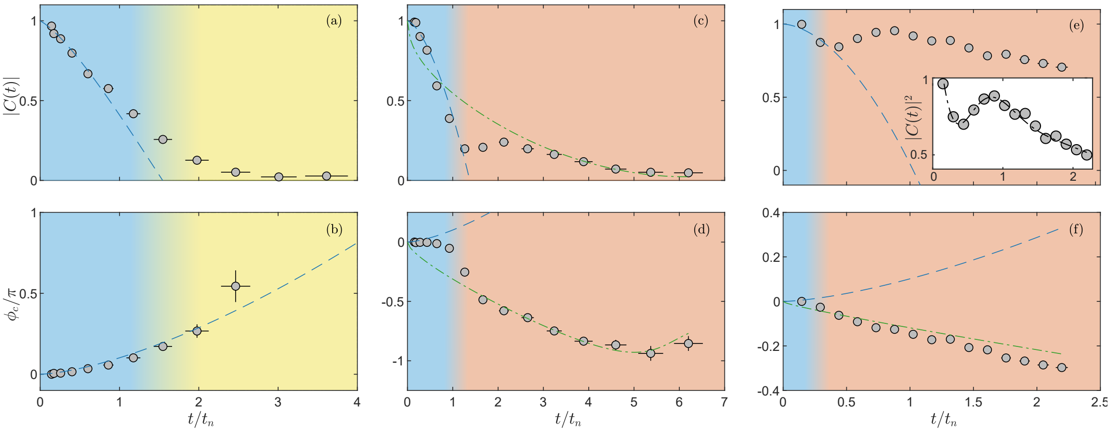

FIG. 2. Impurity dynamics at three characteristic interaction strengths. The coherence function is given for (a,b) strong $1/(k_n a) = 0.4$, (c,d) intermediate $1/(k_n a) = 0.7$, and (c,f) weak $1/(k_n a) = 1.5$ interaction strengths. For comparison, theoretical results for the unitarity-limited case in Eq. (1) (blue dashed line) and for weak two-body interaction Eq. (2) (green dash-dotted line) are shown, without any free fitting parameters. Additional decoherence effects in the system due to three-body losses and the inhomogeneous density distribution, beyond Eqs. (1) and (2), are accounted for in the theoretical description [40].

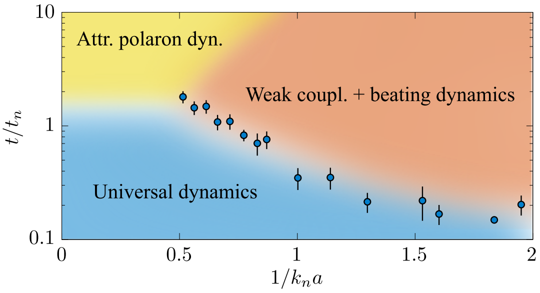

FIG. 3. Dynamics of impurity evolution for repulsive interactions. The characteristic dynamical regimes are indicated as a function of inverse interaction strength $1/(k_n a)$ and evolution time t/t_n. The experimentally extracted crossover times (blue dots) indicate the transition from universal (blue region) to weak coupling and beating dynamics (orange region). For strong interactions and long times, the repulsive polaron decays, and the system is expected to transition into another dynamical regime (yellow region), in which the attractive polaron dominates the dynamics.

that the repulsive polaron eventually dampens out, resulting in the attractive polaron dominating the dynamics, at which point the system enters a new dynamical regime (Fig. 3 yellow region). Experimentally, however, we did not observe signatures of this crossover. This is expected, since we theoretically observe that trap-induced density inhomogeneities significantly delay the crossover in the diagrammatic prediction [40].

We now turn to analyze the quantum beat signal, clearly visible in Figs. 2 (c) and 2 (e), and present throughout the orange region in Fig. 3. Importantly, such a signal is not present for attractive interactions of $1/(k_n a) < 0$, but a similar feature was observed in interferometric investigations of the Fermi polaron [14]. In close analogy, the signal stems from the quantum interference of the repulsive and attractive branches, as demonstrated in the following. We apply a phenomenological model for the coherence function

$$C(t) = Z_g\, e^{-iE_g t/\hbar} + Z_r\, e^{-iE_r t/\hbar} e^{-\Gamma_r t/2}, \tag{3}$$

which we expect to give a good description for weak to intermediate coupling strengths, where the repulsive polaron is well-defined. Indeed, this describes two states; a ground state at energy E_g, and a damped excited state with energy $E_r > E_g$ and damping rate Γ_r, corresponding to the attractive and repulsive polarons with residues Z_g and Z_r, respectively. This implies two main features of the coherence function for weak-coupling beating dynamics. The slope of the phase corresponds to the energy of the repulsive branch since it is expected to have the largest residue, i.e. $\phi_C \approx -E_r t/\hbar$. For sufficiently strong coupling, $Z_g > Z_r$, the above argument no longer holds and the repulsive polaron energy cannot be extracted. In addition, the squared amplitude of the coherence function contains a sinusoidal oscillation at a frequency corresponding to the energy difference between the two branches.

Based on this approach, the experimental coherence amplitude squared and phase are fitted with the functions

$$|\mathscr{C}(t)|^2 = A\, e^{-t/\tau_1} \cos\omega t + B\, e^{-t/\tau_2}, \tag{4}$$

$$\varphi_c = A_\varphi - B_\varphi\, t. \tag{5}$$

This corresponds to the modulus squared of Eq. (3) with an additional exponential decay of the oscillation amplitude to model three-body decay and other loss mechanisms. This is in line with previous interferometric investigations, where three-body losses were introduced as a global loss of coherence [20, 21]. Conversely, we expect the linear behavior of the phase evolution to be more robust and any small effect should be encapsulated in the fitting parameters, A_ϕ and B_ϕ. The energy difference can be extracted from the fitting parameters as $E_r - E_g = \hbar\omega$. An example of the coherence amplitude fit is shown in the inset of Fig. 2 (e). Generally, a single revival is resolved, due to the decoherence effects and losses in the experiment discussed above [40]. Furthermore, the repulsive branch is expected to be damped, such that the beat signal, even in an ideal setting, attenuates in time.

Additionally, the fit directly yields the energy of the repulsive branch, $E_r = \hbar B_\varphi$. This technique, however, can only be used when the phase evolution shows a linear evolution for long times. This is the case for the phase evolution in Fig. 2 (f) but not for Fig. 2 (d), where the last data point shows an increase. This limits our analysis to $1/(k_n a) > 0.85$. To avoid the influence of the unitary regime, the linear fit is, additionally, restricted to $t > t_a$. Figure 4 (upper panel) shows the obtained energies for the repulsive branch for this range of interaction strengths. These energies lie consistently higher than the simple mean-field expectation and agree with a Monte-Carlo prediction [19]. Moreover, they lie systematically higher than our diagrammatic calculation based on the ladder approximation [40]. In fact, we find that the diagrammatic approach only qualitatively describes the dynamics at repulsive interactions, in constrast to what was observed for attractive interactions, where it compares quantitatively well with experiments [20, 21]. We attribute the discrepancy at repulsive interactions to the lacking ability of the diagrammatic approach to accurately describe the repulsive polaron branch in this regime.

Based on these results, the energy of the attractive branch is obtained by subtracting the extracted energy difference from the repulsive branch energy $E_g = E_r - \hbar\omega$ as shown in Fig. 4 (lower panel). The energies agree with both the attractive polaron energy, obtained from diagrammatic calculations, and the molecular energy with an effective range given by the Van der Waals length of our medium, $R^* = 60a_0$ [16, 40]. Experimentally, we cannot distinguish between these two results. However, the rf response of the molecular state is expected to be very small compared to the attractive polaron state, as has been previously measured for the Fermi polaron [8]. In particular, since the molecular state does not have a plane wave component, we expect such a signal to scale with the density of generated impurities. This is indeed much weaker than the response from the attractive polaron state scaling with the density of the entire BEC. With this in mind, the above agreement confirms our interpretation of the beat signal arising from an interference between the two polaron states. Furthermore, the simple linear fitting for the repulsive branch energy yields a robust measurement beyond the accuracy obtained spectroscopically [16]. Note that we see no evidence of the recently predicted presence of meta-stable states at intermediate energies between the two branches [35].

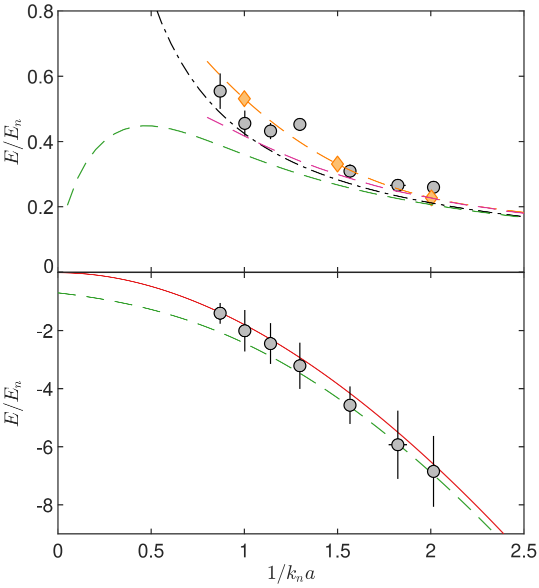

FIG. 4. Energies of the repulsive and attractive branches as a function of the inverse interaction strength. The measured energies are shown as gray points and the result of our diagrammatic calculation is indicated by green dashed lines [40]. (top panel) The repulsive branch energies lie clearly above the simple mean-field expectation (black dash-dotted line) and is consistent with a quantum Monte-Carlo prediction (yellow dashed line, diamonds) as well as a variational truncated basis method calculation (magenta dashed line) [19]. (bottom panel) The attractive branch energies do not allow for a distinction between the diagrammatic result and the molecular energy (red line).

In conclusion, we have performed Ramsey interferometry on a BEC of ^{39}K to investigate the physics of Bose polarons in a wide range of repulsive interactions. The observed quantum beat signal is consistent with a repulsive and attractive quasiparticle branch that form and exist in a coherent superposition. From the beat frequency and the slope of the coherence phase, we determine the energy of these branches. The repulsive branch lies systematically above the simple mean-field expectation and are consistent with a quantum Monte-Carlo prediction [19]. Furthermore, the initial dynamics is seen to agree very well with the exact unitarity-limited behavior with the non-analytical time-dependence of $t^{3/2}$ [20, 42], and the crossover to a weak-coupling regime closely follows the expected $t = ma^2/\hbar$ behavior for $1/(k_n a) > 0.5$. At even stronger interactions of $1/(k_n a) < 0.5$, the dynamics follows the unitarity-limited behavior for long times. This, along with the quantitative discrepancy from the diagrammatic calculations, calls for further theoretical analyses, especially at intermediate to strong repulsive interactions of $0 < 1/(k_n a) < 1$.

The authors thank Ragheed Alhyder for valuable discussions and Adam Chatterley for the careful review of the manuscript. This work was supported by the Danish National Research Foundation through the Center of Excellence “CCQ” (Grant no. DNRF156), by the Novo Nordisk Foundation NERD grant (Grant no. NNF22OC0075986), and by the Independent Research Fund Denmark (Grant no. 0135-00205B). KKN acknowledges support from the Carlsberg Foundation through a Carlsberg Internationalisation Fellowship.

[1] L. D. Landau and S. I. Pekar, Effective mass of a polaron, J. Exp. Theor. Phys. **18**, 419 (1948).
[2] G. Baym and C. Pethick, *Landau Fermi-Liquid Theory: Concepts and Applications* (Wiley-VCH, 1991).
[3] E. Nakano, K. Iida, and W. Horiuchi, Quasiparticle properties of a single α particle in cold neutron matter, Phys. Rev. C **102**, 055802 (2020).
[4] N. Mannella, W. L. Yang, X. J. Zhou, H. Zheng, J. F. Mitchell, J. Zaanen, T. P. Devereaux, N. Nagaosa, Z. Hussain, and Z.-X. Shen, Nodal Quasiparticle in Pseudogapped Colossal Magnetoresistive Manganites, Nature **438**, 474 (2005).
[5] M. Baggioli and O. Pujolàs, Electron-Phonon Interactions, Metal-Insulator Transitions, and Holographic Massive Gravity, Phys. Rev. Lett. **114**, 251602 (2015).
[6] P. A. Lee, N. Nagaosa, and X.-G. Wen, Doping a Mott insulator: Physics of high-temperature superconductivity, Reviews of Modern Physics **78**, 17 (2006).
[7] A. Schirotzek, C.-H. Wu, A. Sommer, and M. W. Zwierlein, Observation of Fermi polarons in a tunable Fermi liquid of ultracold atoms, Physical Review Letters **102**, 230402 (2009).
[8] C. Kohstall, M. Zaccanti, M. Jag, A. Trenkwalder, P. Massignan, G. M. Bruun, F. Schreck, and R. Grimm, Metastability and Coherence of Repulsive Polarons in a Strongly Interacting Fermi Mixture, Nature **485**, 615 (2012).
[9] F. Scazza, G. Valtolina, P. Massignan, A. Recati, A. Amico, A. Burchianti, C. Fort, M. Inguscio, M. Zaccanti, and G. Roati, Repulsive Fermi Polarons in a Resonant Mixture of Ultracold ^{6}Li Atoms, Physical Review Letters **118**, 083602 (2017).
[10] P. Massignan, M. Zaccanti, and G. M. Bruun, Polarons, Dressed Molecules and Itinerant Ferromagnetism in Ultracold Fermi Gases, Reports on Progress in Physics **77**, 034401 (2014).
[11] R. Schmidt, M. Knap, D. A. Ivanov, J.-S. You, M. Cetina, and E. Demler, Universal many-body response of heavy impurities coupled to a Fermi sea: A review of recent progress, Reports on Progress in Physics **81**, 024401 (2018).
[12] F. Scazza, M. Zaccanti, P. Massignan, M. M. Parish, and J. Levinsen, Repulsive fermi and bose polarons in quantum gases, Atoms **10**, 10.3390/atoms10020055 (2022).
[13] M. Cetina, M. Jag, R. S. Lous, J. T. M. Walraven, R. Grimm, R. S. Christensen, and G. M. Bruun, Decoherence of Impurities in a Fermi Sea of Ultracold Atoms, Physical Review Letters **115**, 135302 (2015).
[14] M. Cetina, M. Jag, R. S. Lous, I. Fritsche, J. T. Walraven, R. Grimm, J. Levinsen, M. M. Parish, R. Schmidt, M. Knap, *et al.*, Ultrafast Many-Body Interferometry of Impurities Coupled to a Fermi Sea, Science (New York, N.Y.) **354**, 96 (2016).
[15] C. Baroni, B. Huang, I. Fritsche, E. Dobler, G. Anich, E. Kirilov, R. Grimm, M. A. Bastarrachea-Magnani, P. Massignan, and G. Bruun, Mediated interactions between Fermi polarons and the role of impurity quantum statistics (2023), arXiv:2305.04915 [cond-mat.quant-gas].
[16] N. B. Jørgensen, L. Wacker, K. T. Skalmstang, M. M. Parish, J. Levinsen, R. S. Christensen, G. M. Bruun, and J. J. Arlt, Observation of Attractive and Repulsive Polarons in a Bose-Einstein Condensate, Physical Review Letters **117**, 055302 (2016).
[17] M.-G. Hu, M. J. Van de Graaff, D. Kedar, J. P. Corson, E. A. Cornell, and D. S. Jin, Bose Polarons in the Strongly Interacting Regime, Physical Review Letters **117**, 055301 (2016).
[18] Z. Z. Yan, Y. Ni, C. Robens, and M. W. Zwierlein, Bose Polarons near Quantum Criticality, Science (New York, N.Y.) **368**, 190 (2020).
[19] L. A. Peña Ardila, N. B. Jørgensen, T. Pohl, S. Giorgini, G. M. Bruun, and J. J. Arlt, Analyzing a Bose Polaron across Resonant Interactions, Physical Review A: Atomic, Molecular, and Optical Physics **99**, 063607 (2019).
[20] M. G. Skou, T. G. Skov, N. B. Jørgensen, K. K. Nielsen, A. Camacho-Guardian, T. Pohl, G. M. Bruun, and J. J. Arlt, Non-Equilibrium Quantum Dynamics and Formation of the Bose Polaron, Nature Physics **17**, 731 (2021).
[21] M. G. Skou, K. K. Nielsen, T. G. Skov, A. M. Morgen, N. B. Jørgensen, A. Camacho-Guardian, T. Pohl, G. M. Bruun, and J. J. Arlt, Life and death of the Bose polaron, Phys. Rev. Res. **4**, 043093 (2022).
[22] W. Casteels and M. Wouters, Polaron formation in the vicinity of a narrow Feshbach resonance, Physical Review A: Atomic, Molecular, and Optical Physics **90**, 043602 (2014).
[23] R. S. Christensen, J. Levinsen, and G. M. Bruun, Quasiparticle Properties of a Mobile Impurity in a Bose-Einstein Condensate, Physical Review Letters **115**, 160401 (2015).
[24] S. P. Rath and R. Schmidt, Field-Theoretical Study of the Bose Polaron, Physical Review A: Atomic, Molecular, and Optical Physics **88**, 053632 (2013).
[25] W. Li and S. Das Sarma, Variational Study of Polarons in Bose-Einstein Condensates, Physical Review A: Atomic, Molecular, and Optical Physics **90**, 013618 (2014).
[26] J. Levinsen, M. M. Parish, and G. M. Bruun, Impurity in a Bose-Einstein Condensate and the Efimov Effect, Physical Review Letters **115**, 125302 (2015).
[27] Y. E. Shchadilova, R. Schmidt, F. Grusdt, and E. Demler, Quantum Dynamics of Ultracold Bose Polarons, Physical Review Letters **117**, 113002 (2016).
[28] N.-E. Guenther, P. Massignan, M. Lewenstein, and G. M. Bruun, Bose Polarons at Finite Temperature and Strong Coupling, Physical Review Letters **120**, 050405 (2018).
[29] S. M. Yoshida, S. Endo, J. Levinsen, and M. M. Parish, Universality of an Impurity in a Bose-Einstein Condensate, Physical Review X **8**, 011024 (2018).
[30] M. Drescher, M. Salmhofer, and T. Enss, Theory of a Resonantly Interacting Impurity in a Bose-Einstein Condensate, Physical Review Research **2**, 032011 (2020).
[31] P. Massignan, N. Yegovtsev, and V. Gurarie, Universal Aspects of a Strongly Interacting Impurity in a Dilute Bose Condensate, Phys. Rev. Lett. **126**, 123403 (2021).
[32] J. Levinsen, L. A. Peña Ardila, S. M. Yoshida, and M. M. Parish, Quantum Behavior of a Heavy Impurity Strongly Coupled to a Bose Gas, Phys. Rev. Lett. **127**, 033401 (2021).
[33] R. Schmidt and T. Enss, Self-stabilized Bose polarons, SciPost Phys. **13**, 054 (2022).
[34] A. Christianen, J. I. Cirac, and R. Schmidt, Phase diagram for strong-coupling Bose polarons (2023), arXiv:2306.09075 [cond-mat.quant-gas].

[35] N. Mostaan, N. Goldman, and F. Grusdt, A unified theory of strong coupling Bose polarons: From repulsive polarons to non-Gaussian many-body bound states (2023), arXiv:2305.00835 [cond-mat.quant-gas].

[36] L. Wacker, N. B. Jørgensen, D. Birkmose, R. Horchani, W. Ertmer, C. Klempt, N. Winter, J. Sherson, and J. J. Arlt, Tunable Dual-Species Bose-Einstein Condensates of ^{39}K and ^{87}Rb, Physical Review A: Atomic, Molecular, and Optical Physics **92**, 053602 (2015).

[37] M. Lysebo and L. Veseth, Feshbach Resonances and Transition Rates for Cold Homonuclear Collisions between ^{39}K and ^{41}K Atoms, Physical Review A: Atomic, Molecular, and Optical Physics **81**, 032702 (2010).

[38] L. Tanzi, C. R. Cabrera, J. Sanz, P. Cheiney, M. Tomza, and L. Tarruell, Feshbach Resonances in Potassium Bose-Bose Mixtures, Physical Review A: Atomic, Molecular, and Optical Physics **98**, 062712 (2018).

[39] R. J. Fletcher, R. Lopes, J. Man, N. Navon, R. P. Smith, M. W. Zwierlein, and Z. Hadzibabic, Two-and three-body contacts in the unitary Bose gas, Science (New York, N.Y.) **355**, 377 (2017).

[40] See Supplementary Material [url], for further details.

[41] E. Braaten, D. Kang, and L. Platter, Short-Time Operator Product Expansion for Rf Spectroscopy of a Strongly Interacting Fermi Gas, Physical Review Letters **104**, 223004 (2010).

[42] M. M. Parish and J. Levinsen, Quantum Dynamics of Impurities Coupled to a Fermi Sea, Physical Review B **94**, 184303 (2016).

[43] Interestingly, we find that this behaviour of the phase persists for relatively long times beyond $t \simeq 1.4 t_n$ for $1/(k_n a) \lesssim 0.5$ as exemplified in Fig. 2(b), where a direct crossover to the many-body regime was observed for attractive interactions [20].

[44] K. K. Nielsen, L. A. Peña Ardila, G. M. Bruun, and T. Pohl, Critical Slowdown of Non-Equilibrium Polaron Dynamics, New Journal of Physics **21**, 043014 (2019).

[45] The beat signal has a very minor impact on the coherence phase at short times [40], consistent with the good agreement in Fig. 2(d).

SUPPLEMENTARY INFORMATION FOR “QUANTUM BEAT SPECTROSCOPY OF REPULSIVE BOSE POLARONS”

A. M. Morgen,[1] S. S. Balling,[1] K. Knakkergaard Nielsen,[2] T. Pohl,[1,3] G. M. Bruun,[1] and J. J. Arlt[1]
[1]*Center for Complex Quantum Systems, Department of Physics and Astronomy, Aarhus University, Ny Munkegade 120, DK-8000 Aarhus C, Denmark*
[2]*Max-Planck Institute for Quantum Optics, Hans-Kopfermann-Str. 1, D-85748 Garching, Germany*
[3]*Institute for Theoretical Physics, Vienna University of Technology, Wiedner Hauptstraße 8-10, 1040 Vienna, Austria*

(Dated: June 28, 2024)

SI. EXPERIMENTAL DATA ANALYSIS

A. Extracted energy differences

The quantum beat signal observed for the coherence amplitude in the main manuscript was fitted with a phenomenological model and the energy difference between the repulsive and attractive branches was extracted. In combination with the linear fit of the phase evolution, this was used to find the energy of the attractive and repulsive branches.

Figure S1 shows all extracted energy differences as a function of the inverse interaction strength. Additional energy differences at high interaction strengths are included, where the linear fit of the phase evolution fails but a quantum beat is still observed in the coherence amplitude, as is the case for $1/k_n a = 0.7$ in Fig. 2 (c) and (d) in the main manuscript. The extracted energy differences show a general increase from strong to weak interactions, which is primarily due to the large negative energy of the attractive branch. For large interaction strengths and consequently small values of $1/(k_n a) < 0.7$, no quantum beat signals are observed. We attribute this to the rapid damping of the repulsive polaron along with the universal decay of the coherence function and rapid decoherence processes in our experiment.

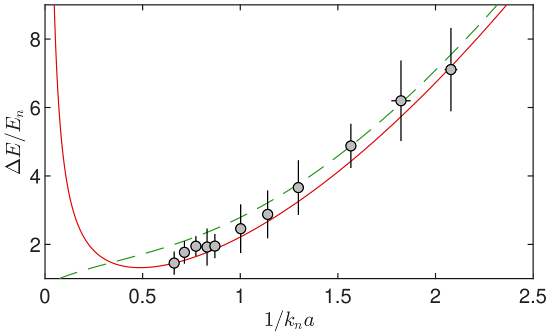

FIG. S1. **Energy differences.** Energy differences between the attractive and repulsive branches extracted from the beat signal in the coherence amplitude (gray points). For comparison, the energy difference between the attractive and repulsive polaron energy obtained from the diagrammatic calculation in Sec. SII B (green dashed line) is shown. Moreover, the energy difference between the mean-field energy and the molecular energy (red line) is indicated.

Figure S1 also compares the data with, the energy difference between the attractive and repulsive polaron energy calculated in Sec. SII B and with the energy difference between the mean-field energy and the molecular energy. The data is in good agreement with both predictions but does not allow for a distinction between them.

B. Decoherence from impurity losses

The loss of impurity atoms leads to faster decoherence of the system and is mainly caused by three-body losses with medium atoms, which has to be accounted for. The lifetime of impurity atoms was previously investigated for attractive interactions between the impurity and the medium [1] and the same approach is used here for repulsive interactions. In brief, the experimental sequence starts with a Bose-Einstein condensate (BEC) in the $|F = 1, m_F = -1\rangle$ medium state. An initial radio frequency pulse produces a 10% admixture in the $|F = 1, m_F = 0\rangle$ impurity state, as opposed to the 5% used in the experimental sequence described in the main manuscript. This is to increase the extracted signal, as well as being the maximal impurity admixture for the sequence in the main manuscript after both pulses. Following the initial pulse, impurity atoms are lost due to three body collisions, where two medium atoms are lost for each impurity atom. After a variable wait time the remaining impurities are transferred to the third state, $|F=1, m_F=1\rangle$, using a π-pulse. In this state the impurity atoms are quickly lost due to two-body collisions with medium atoms. The final atom number in the medium state is then observed as a function of the waiting time for various interaction strengths. Since the two loss processes lead to a different number of lost medium atoms, this sequence allows for a measurement of the impurity lifetime by measuring the number of medium atoms. An exponential fit of the form $\sim \exp(-\Gamma_{\text{loss}} t)$ is applied for each data set, to extract the loss rate Γ_{loss}. The observed loss rates for repulsive interactions (green points) are shown as a function of inverse interaction strength in Fig. S2. For comparison, Fig. S2 also includes the previously measured loss rates for attractive interactions (red points) [1]. An empirical fit of the form, $\beta_1 + \beta_2 \exp(\beta_3/k_n a)$ was performed to extract the loss rate at arbitrary interaction strengths. The theoretically calculated coherence function is then modified according to $C(t) \to C(t)\exp(-\Gamma_{\text{loss}} t)$, before comparison with the experimental results in Fig. 2 of the main manuscript.

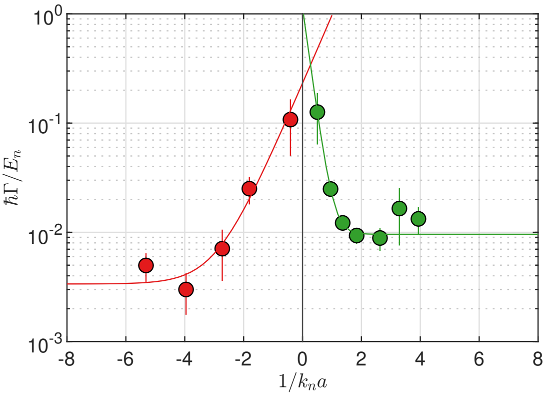

FIG. S2. **Loss rates**. Measured loss rates of impurity atoms embedded in a Bose-Einstein condensate as a function of the inverse interaction strength. The measured loss rates for repulsive interactions (green points) are shown together with previous experimental data for attractive interactions [1] (red points). The solid lines indicate fits to the data (see text).

C. Decoherence from density inhomogeneity

The harmonic trap used in the experiment leads to an inhomogeneous density distribution of the atomic clouds. This causes additional decoherence of the system since the impurities at high medium density at the center of the cloud evolve differently compared to those at the edge.

It is therefore necessary to perform a local density approximation of the theoretical coherence function [1]. This corresponds to an integration of the coherence function over its density dependent terms according to

$$\langle C(t)\rangle = \frac{15}{4n_0}\int_0^{n_0} dn \frac{n}{n_0}\sqrt{1-\frac{n}{n_0}}C(t), \tag{S1}$$

in the Thomas-Fermi approximation. The theoretically calculated coherence function is then modified according to $C(t) \to \langle C(t)\rangle$, for comparison with the experimental results in Fig. 2 of the main manuscript.

SII. THEORETICAL ANALYSIS

A. Exact short-time dynamics at weak coupling

Here, we derive the exact short-time dynamics for repulsive interactions at weak coupling $1/k_n a \gg 1$. The analysis is similar to the one described in the Supplementary Material of ref. [1]. The coherence dynamics is in general calculated from the Fourier transformation of the zero momentum spectral function, $C(t)=\int_{-\infty}^{+\infty} d\omega e^{-i\omega t}A(\omega)/2\pi$. We may decompose this as

$$C(t) = \int_{-\infty}^{+\infty} \frac{d\omega}{2\pi} e^{-i\omega t} A(\omega)$$
$$= \int_{-\infty}^{+\infty} \frac{d\omega}{2\pi}(1-i\omega t)A(\omega) + \int_{0}^{+\infty} \frac{d\omega}{2\pi}\left[e^{-i\omega t}-(1-i\omega t)\right]A(\omega) + \int_{-\infty}^{0} \frac{d\omega}{2\pi}\left[e^{-i\omega t}-(1-i\omega t)\right]A(\omega). \tag{S2}$$

In refs. [1, 2] it is shown that $\int_{-\infty}^{+\infty} \frac{d\omega}{2\pi}\omega A(\omega) \propto 4\pi\hbar a_B/m$, where a_B is the medium-medium scattering length. Hence, this term can safely be omitted. An exact expression for the second term at short times was also previously determined [1] from the exact high-frequency tail of the spectral function [2] to yield the contribution

$$C_{\text{tail}}(t) = \int_{0}^{+\infty} \frac{d\omega}{2\pi}\left[e^{-i\omega t}-(1-i\omega t)\right]A_{\text{tail}}(\omega) = \frac{2}{3\pi}(k_n|a|)^3\left[1+\frac{it}{t_a}-\frac{2}{\sqrt{\pi}}\Gamma\left(\frac{3}{2},\frac{it}{t_a}\right)\right], \tag{S3}$$

with $t_a = ma^2/\hbar$, and $\Gamma(\nu,x)=\int_x^\infty ds\, s^{\nu-1}e^s$ the upper incomplete gamma function. This calculation, hereby, fully accounts for the exact high-frequency tail. The third term in Eq. (S2) can be omitted only at times shorter than $\hbar/|E_g|$, where E_g is the energy of the attractive polaron. For $1/k_n a \ll -1$, this coincides with the mean field timescale, whereas at unitarity $E_g \simeq -E_n$, such that $C(t)=1+C_{\text{tail}}(t)$ up to times of order t_n. For positive scattering lengths, the attractive polaron, however, eventually approaches the energy $E_m=-\hbar^2/ma^2$ of a universal Feshbach molecule. Since the associated timescale of this state coincides with t_a, $\hbar/|E_m|=t_a$, it will have a considerable contribution for times $t>t_a$. At weak coupling, this may be evaluated exactly, because the ladder approximation in this limit provides the correct perturbative description. In particular, as the energy approaches $E_m=-\hbar^2/ma^2$, the residue can be computed from the expression [3]

$$Z_g = \frac{1}{1+\frac{3\pi}{8\sqrt{2}}\left(\frac{|E_g|}{E_n}\right)^{3/2}} \to \frac{1}{1+\frac{3\pi}{4}\frac{1}{(k_n a)^3}} \to \frac{4}{3\pi}(k_n a)^3. \tag{S4}$$

The first equality here is obtained by combining Eqs. (S13) and (S14) in the Supplementary Material of Ref. [3]. In this regime, $A(\omega)=2\pi Z_g\delta(\omega-E_m/\hbar)$ for $\omega<0$. As a result, the third term in Eq. (S2) at weak coupling is given by

$$C_g(t) = \int_{-\infty}^{0} \frac{d\omega}{2\pi}\left[e^{-i\omega t}-(1-i\omega t)\right]A(\omega) \to \frac{4}{3\pi}(k_n a)^3\left[e^{it/t_a}-\left(1+\frac{it}{t_a}\right)\right] \tag{S5}$$

The total short-time coherence function is then

$$C(t) = 1+C_{\text{tail}}(t)+C_g(t) = 1-\frac{2}{3\pi}(k_n a)^3\left[1+\frac{it}{t_a}+2e^{it/t_a}\left(\frac{1}{\sqrt{\pi}}\Gamma\left(\frac{3}{2},\frac{it}{t_a}\right)-1\right)\right]. \tag{S6}$$

For $t \ll t_a$, this yields the same unitarity-limited behavior as for negative scattering lengths,

$$C(t) = 1-(1-i)k_{3/2}\left(\frac{t}{t_n}\right)^{3/2}, \tag{S7}$$

with $k_{3/2}=16/(9\pi^{3/2})$. On the other hand, the dynamics for times $t>t_a$ is now qualitatively different from the one found for negative scattering lengths. In particular, comparing Eq. (S6) to the weak coupling behavior

$$C_w(t) = 1-\frac{2}{3\pi}(k_n a)^3-\frac{iE_{\text{mf}}t}{\hbar}-(1+i)\sqrt{\frac{t}{t_w}}, \tag{S8}$$

with $t_w=\frac{m}{32\pi\hbar n_B^2 a^4}$ in Fig. S3 demonstrates that the full dynamics shows oscillations around the behavior described by Eq. (S8) at a frequency given by $1/t_a=\hbar/ma^2$. The modification of the coherence phase is, however, seen to be minor.

B. Polaron energies in the ladder approximation

Here, we briefly outline the calculation of the attractive and repulsive polaron energies in the ladder approximation [4]. In the experiment, the medium-medium scattering length is $k_n a_B \simeq 0.01$. We, therefore, assume that the relevant physics can be explained by assuming an ideal BEC. The impurity Green's function $G^{-1}(\omega)=\omega+i\eta-\Sigma(\omega)$ (evaluated at zero momentum

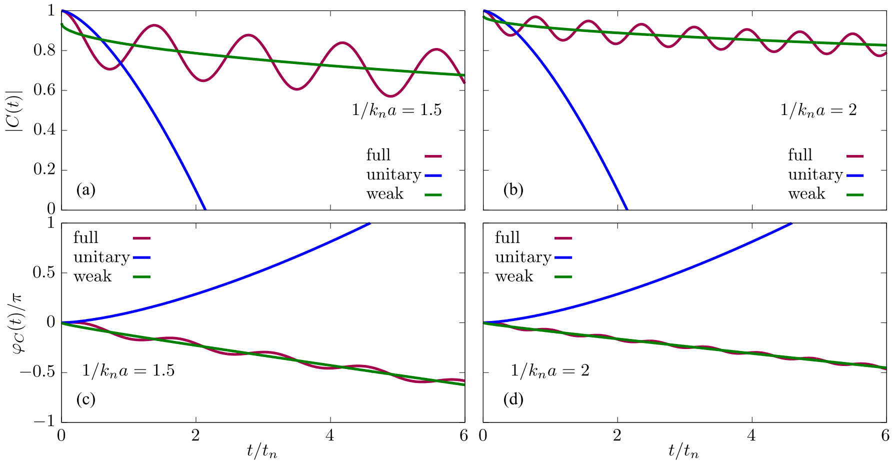

FIG. S3. **Short-time dynamics at weak coupling**. The coherence amplitude (a), (b) and phase (c), (d) at indicated interaction strengths. The blue line describes unitary behavior valid for $t \ll t_a$ (Eq. (S7)), the green line is described by Eq. (S8), while the full dynamics in red is described by Eq. (S6).

and equal masses), is expressed in terms of the self-energy $\Sigma(\omega)$, which in the ladder approximation may additionally be written as $\Sigma(\omega) = n_B\mathscr{T}(\omega)$. Here,

$$\mathscr{T}(\omega) = \frac{1}{\frac{m}{4\pi\hbar^2\tilde{a}(\omega)} - \Pi(\omega)} \tag{S9}$$

is the $\mathscr{T}$-matrix, and $1/\tilde{a}(\omega) = 1/a + R^* m\omega$ includes the effect of the finite range parameter R^* [5]. For the Feshbach resonance in question the range parameter is estimated to be $R^* = 60a_0$ [6]. We find this to be important to quantitatively capture the attractive polaron energy in the regime $1/k_na > 0.5$. Finally, $\Pi(\omega) = -im^{3/2}(\omega + i\eta)^{1/2}/(4\pi\hbar^{5/2})$ is the pair propagator, and η is a positive infinitesimal. The attractive polaron energy is then determined by the equation $E_g/\hbar = \Sigma(E_g/\hbar)$, while the repulsive polaron energy satisfies $E_r/\hbar = \mathrm{Re}[\Sigma(E_r/\hbar)]$ for $E_r > 0$. We find that these equations can equivalently be expressed as

$$\begin{aligned} \frac{E_g}{E_n} &= \frac{4}{3\pi} \frac{1}{\frac{1}{k_na} + k_nR^*\frac{E_g}{2E_n} - \sqrt{\frac{|E_g|}{2E_n}}}, \\ \frac{E_r}{E_n} &= \frac{4}{3\pi} \frac{\frac{1}{k_na} + k_nR^*\frac{E_g}{2E_n}}{\left(\frac{1}{k_na} + k_nR^*\frac{E_r}{2E_n}\right)^2 + \frac{E_r}{2E_n}}. \end{aligned} \tag{S10}$$

Using $k_nR^* \simeq 0.06$, the numerical solution of these equations leads to the results in Fig. 4 of the main text.

C. Phase evolution with and without trap averaging

Using the ladder approximation, we, here, provide strong theoretical evidence that the initial evolution of the coherence phase follows the repulsive polaron energy. We also show that trap averaging leads to a severe delay or even prevention of the crossover into the dynamical regime dominated by attractive polaron dynamics.

The coherence function is calculated as the Fourier transform of the zero momentum spectral function, $C(t) = \int_{-\infty}^{+\infty} d\omega e^{-i\omega t}A(\omega)/2\pi$. The spectral function $A(\omega) = -2\mathrm{Im}G(\omega)$ is evaluated within the ladder approximation described in the previous subsection. In particular, $G^{-1}(\omega) = \omega + i\eta - \Sigma(\omega)$, is evaluated from the self-energy

$$\frac{\Sigma(\omega)}{E_n} = \frac{4/3\pi}{\frac{1}{k_na} + k_nR^*\frac{\hbar\omega}{2E_n} + i\sqrt{\frac{\hbar\omega}{2E_n}}}. \tag{S11}$$

In Fig. S4, we show the resulting phase evolution $\varphi_C(t) = \arg(C(t))$. This is shown both for a homogeneous system and in a harmonic trap. For the latter, we use a local density approximation to evaluate the trap-averaged coherence function $\langle C(t)\rangle = \frac{15}{4n_0}\int_0^{n_0} dn \frac{n}{n_0}\sqrt{1-\frac{n}{n_0}}C(n,t)$, as described previously in Sec. SI C. The key insights of this calculations are the following. (1) The initial behavior of the phase follows the one corresponding to the repulsive polaron: $-iE_r t/\hbar$, and not the mean-field energy. This is also the case for the system in a trap. Experimentally, this allows us to extract the repulsive polaron energy from the short-time linear slope of the phase. (2) For a homogeneous system, as the repulsive polaron dampens out, the phase rapidly switches behavior and starts following the attractive polaron phase evolution $-iE_g t/\hbar$. (3) In the harmonic trap, this crossover is either severely delayed as in Fig. S4(right), or entirely washed out as in Fig. S4(left).

We find, however, that the ladder approximation does not quantitatively describe the phase evolution. It seems to overestimate the overall amplitude of the beat signal between the repulsive and attractive polarons. Furthermore, the repulsive polaron energies extracted in the experiment lie systematically above the ones found in the ladder approximation.

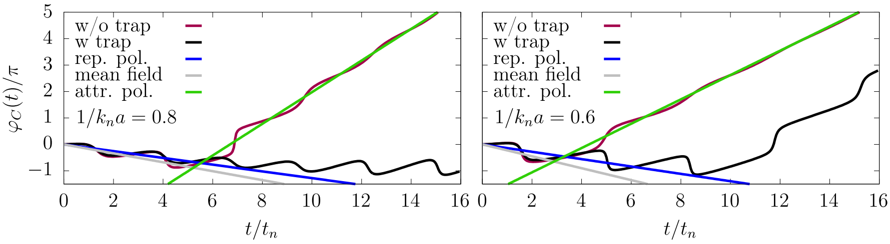

FIG. S4. **Phase evolution in the ladder approximation**. The coherence phase is shown for two indicated interaction strengths for a homogeneous system (red line) as well as in a harmonic trap (black line). We also show the phase evolution corresponding to repulsive and attractive polarons (blue and green lines, respectively), as well as the mean field phase evolution in grey.

---

[1] M. G. Skou, T. G. Skov, N. B. Jørgensen, K. K. Nielsen, A. Camacho-Guardian, T. Pohl, G. M. Bruun, and J. J. Arlt, Non-Equilibrium Quantum Dynamics and Formation of the Bose Polaron, Nature Physics **17**, 731 (2021).

[2] E. Braaten, D. Kang, and L. Platter, Short-Time Operator Product Expansion for Rf Spectroscopy of a Strongly Interacting Fermi Gas, Physical Review Letters **104**, 223004 (2010).

[3] Z. Z. Yan, Y. Ni, C. Robens, and M. W. Zwierlein, Bose Polarons near Quantum Criticality, Science (New York, N.Y.) **368**, 190 (2020).

[4] S. P. Rath and R. Schmidt, Field-Theoretical Study of the Bose Polaron, Physical Review A: Atomic, Molecular, and Optical Physics **88**, 053632 (2013).

[5] I. Fritsche, C. Baroni, E. Dobler, E. Kirilov, B. Huang, R. Grimm, G. M. Bruun, and P. Massignan, Stability and breakdown of Fermi polarons in a strongly interacting Fermi-Bose mixture, Phys. Rev. A **103**, 053314 (2021).

[6] N. B. Jørgensen, L. Wacker, K. T. Skalmstang, M. M. Parish, J. Levinsen, R. S. Christensen, G. M. Bruun, and J. J. Arlt, Observation of Attractive and Repulsive Polarons in a Bose-Einstein Condensate, Physical Review Letters **117**, 055302 (2016).

CHAPTER 7

Conclusion & Outlook

In this thesis, multiple aspects of impurity physics were investigated for the particular case of the Bose polaron. This included both attractive and repulsive impurity-medium interactions and allowed for a detailed comparison with theoretical models.

In Chap. 4, three-body recombination processes for an impurity immersed in a BEC were investigated for attractive impurity-medium interactions. Accurate modeling of the losses allowed for extracting the three-body loss rate coefficient as a function of the impurity-medium scattering length. From this, the density of the system was estimated at a variable time in the ejection protocol. This was compared to an entirely experimental method, with good agreement between the two. Finally, it was found that the loss processes resulted in more medium atoms lost per impurity than expected. This was interpreted as the result of secondary collisions in the systems.

In Chap. 5, spectroscopy results using the ejection protocol were presented, for attractive impurity-medium interactions. A polaron signal was observed and compared to the theoretical prediction with good agreement after taking experimental modifications into account. Additionally, experimental evidence for the observation of the bipolaron state was presented and analyzed.

In Chap. 6, an interferometric sequence was utilized for probing the short-time dynamics of an impurity immersed in a BEC, with repulsive impurity-medium interactions. The results revealed distinct dynamical regimes, as well as a quantum beat effect arising from the interference of the repulsive and attractive polaron states. Finally, the energies of these states were extracted and compared to theoretical predictions.

Outlook

The results for the Bose polaron presented in this thesis are readily extended to other interesting features of impurity physics. These include applying ejection spectroscopy for repulsive impurity-medium interactions to capture both the attractive and repulsive branches and varying the impurity concentration at fixed attractive interaction strengths to investigate the bipolaron signal further. In the following, select research directions for impurity physics are discussed.

Ramsey measurements

In Chap. 6, the Bose polaron was investigated by varying the phase of the second rf-pulse in the interferometric sequence for different evolution times. The repulsive polaron energies were then extracted from the linear behavior of the phase evolution. These were observed to lie systematically above the mean field result, fluctuating around the quantum Monte-Carlo results. This result prompted the need for a higher precision measurement of the repulsive polaron energy, to better distinguish between the theoretical predictions. The preliminary results of this investigation are briefly presented here.

First, an alternative method for investigating the energy of the repulsive state is proposed. In the standard Ramsey measurement, the frequencies of both interferometric pulses are varied together and the relative phase between the pulses is fixed to π. Additionally, a sufficiently long evolution time is used to ensure the formation of polarons. The sequence is illustrated

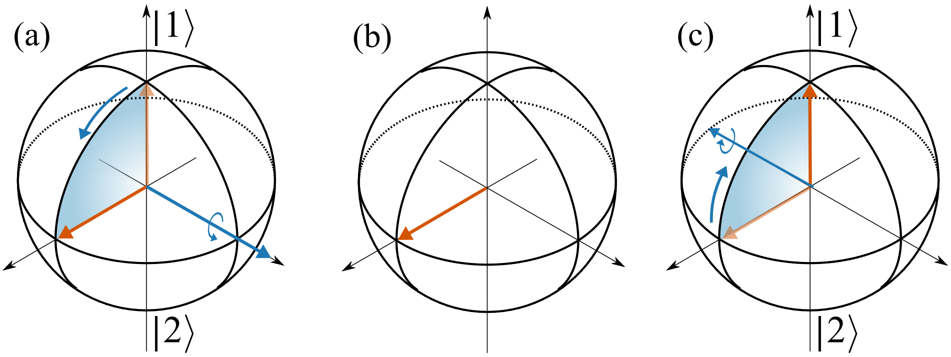

FIGURE 7.1: Ramsey measurement illustrated on the Bloch sphere, when the frequencies of both rf-pulses are exactly resonant to the $|1\rangle$ to $|2\rangle$ transition. a) The initial rf-pulse creates the superposition of the $|1\rangle$ and $|2\rangle$ states. b) During the evolution time, the Bloch vector does not precess since the rf-pulses have zero detuning. c) The final rf-pulse has a π-shift relative to the first rf-pulse and the atoms are transferred back to the $|1\rangle$ state. If the rf-pulses are not resonant, the Bloch precesses in b), and the final rf-pulse will not have an ideal transfer back to the $|1\rangle$ state.

using the Bloch sphere picture in Fig. 7.1, where the medium and impurity states are at the top and bottom, respectively. The initial rf-pulse creates a superposition of the impurity and medium state, with only a small fraction in the former. During the evolution time, the precession of the Bloch vector is given by the detuning of the rf-pulse to the polaron state. If this is on resonance, the Bloch vector remains stationary and the second rf-pulse has the optimal conditions for transferring the impurities back to the medium state. If the frequency of both rf-pulses are varied, the Bloch vector precesses during the evolution time and characteristic Ramsey fringes are observed in the medium atom number according to

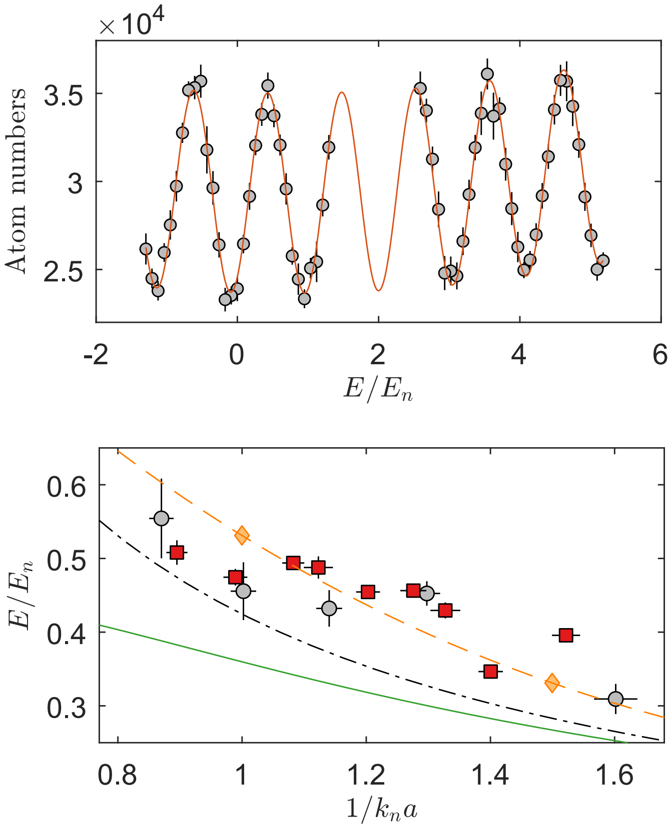

FIGURE 7.2: (top) Example of a Ramsey measurement at $1/k_n a = +1.3$, where a shifted maximum of atom numbers, with respect to $E = 0$, is observed. (bottom) Extracted energies of the repulsive polaron state (red squares) as a function of inverse interaction strength. These are compared to the results from the phase evolution analysis (grey points) in Chap. 6, as well as the quantum Monte-Carlo results (yellow diamonds), mean-field energy (black dash-dotted) and diagrammatic prediction (green solid line).

$$N(\delta) = A\left[\frac{\sin(\delta\tau_p/2)}{\delta\tau_p/2}\right]^2 \cos^2\left(\frac{\delta T}{2}\right). \tag{7.1}$$

Here the detuning and duration of the rf-pulses are given by δ and τ_p, respectively. The evolution time of the system is T and A is an amplitude, used for fitting to the experimental signal. The duration of the rf-pulses is much shorter than the evolution time and the sinc function is slowly varying compared to the cosine. An example of this is shown for $1/k_na = +1.3$ in Fig. 7.2, where clear oscillations of the atom number are observed as a function of varying the rf-pulse frequency. A maximum is observed close to $E = 0$ at positive energies. This shifted peak is taken as the shift of the energy of the repulsive polaron. The measurement is then repeated for different interaction strengths, with the extracted polaron energies shown in Fig. 7.2. These energies are compared to those already presented in Chap. 6 along with the theoretical predictions. Similar to the energies extracted from the phase evolution, the energies are observed to fluctuate around the quantum Monte-Carlo calculation. The extracted energies represent a higher precision measurement as reflected in their small vertical error bar, but they have roughly the same fluctuation as the phase evolution results. is is attributed to some underlying systematic uncertainty that is not accounted for and these measurements are still being investigated.

Orthogonality catastrophe

The medium-medium interaction strength is expected to affect the stability of the polaron and if tuned to zero, the so-called orthogonality catastrophe has been predicted to occur [157, 158]. As this zero crossing is approached the quasiparticle residue approaches zero and the polaron becomes ill-defined. Investigating the medium-medium interaction thus provides insight into the stability of the system by changing the compressibility of the BEC. For our system, the Feshbach resonance at 114 G utilized in

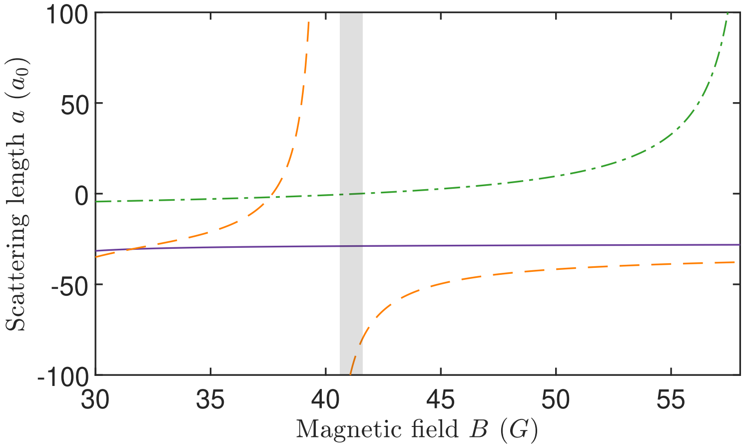

FIGURE 7.3: Intrastate scattering lengths for the $|F=1,m_F=0\rangle$ state (green line) and the $|F=1,m_F=1\rangle$ state (purple line), as a function of the magnetic field. An interstate Feshbach resonance between these is located around 40 G (orange line). Additionally, a zero crossing for the $|F=1,m_F=0\rangle$ state appears at $\approx$ 41 G (gray area).

this thesis gives a constant medium-medium scattering length around $10a_0$, which is relatively low.

However, around 40 G the internal scattering length for the $|F=1,m_F=0\rangle$ state can be tuned through a zero crossing as shown in Fig. 7.3. Additionally, a Feshbach resonance between the $|F=1,m_F=0\rangle$ and $|F=1,m_F=+1\rangle$ states is present at a magnetic field in the close vicinity. The $|F=1,m_F=0\rangle$ state could then be used as the medium state and the $|F=1,m_F=+1\rangle$ as the impurity state. The production of a BEC in the medium state should be simple, as it has a Feshbach resonance at slightly larger magnetic fields, which could be utilized to ensure effective evaporative cooling.

Alternatively, multiple Feshbach resonances exist at high magnetic fields > 400 G, which would require several modifications to the existing apparatus to realize.

Quantum engine

A final example of future prospects for experiments lies beyond impurity physics and explores the area of thermodynamics. A classical engine is characterized by a cycle where heat and work are transferred in and out of the system by a working fluid. Multiple cycles exist that seek to optimize the efficiency of this transfer by expanding and compressing the working fluid under specific conditions. In the context of ultracold quantum gases, one can design a cycle where the gas is compressed and expanded while varying the scattering length of the atoms. This results in an energy transfer between the magnetic and optical fields. Such a cycle was investigated in Ref. [159] using ^{7}Li, both in the case of a thermal and condensed gas, where the latter was observed to have a higher efficiency in terms of the released energy after a full cycle.

However, the tuning range of the scattering length of the medium was only considered in the range of $100-250a_0$, for which our system can be extended considerably further. This tuning, along with the different possible cycles [160–163], opens up new interesting physics to explore, with very few modifications to our current experimental setup.

Final remarks

With the conclusion of this thesis, my contributions to the field of impurity physics have been laid out and the stage is now set for our system to continue exploring this field as well as new exciting physics. Although the scientific achievements were highlighted, the biggest advancement has been the technical skills and personal development I have acquired along the way. I now look forward to a new chapter in my life, where new challenges await.

Bibliography

[1] M. G. Skou, K. K. Nielsen, T. G. Skov, A. M. Morgen, N. B. Jørgensen, A. Camacho-Guardian, T. Pohl, G. M. Bruun and J. J. Arlt, 'Life and death of the Bose polaron', Physical Review Research **4**, 043093 (2022).

[2] A. M. Morgen, S. S. Balling, K. K. Nielsen, T. Pohl, G. M. Bruun and J. J. Arlt, 'Quantum beat spectroscopy of repulsive bose polarons', arXiv:2310.18183 (2023).

[3] A. M. Morgen, S. S. Balling, M. T. Strøe, M. G. Skou and J. J. Arlt, 'Three-body Physics in the Impurity Limit in ^{39}K', In preparation (2024).

[4] A. M. Morgen, S. S. Balling, M. T. Strøe, K. K. Nielsen, T. Pohl, G. M. Bruun and J. J. Arlt, 'Observation of Deeply Bound Polaronic States', In preparation (2024).

[5] M. K. E. L. Planck, 'Zur theorie des gesetzes der energieverteilung im normalspectrum', **2**, 237 (1900).

[6] A. Einstein, 'Über einen die erzeugung und verwandlung des lichtes betreffenden heuristischen gesichtspunkt', Annalen der Physik **322**, 132–148 (1905).

[7] N. Bohr, 'On the constitution of atoms and molecules', The London, Edinburgh, and Dublin Philosophical Magazine and Journal of Science **26**, 1–25 (1913).

[8] W. Gerlach and O. Stern, 'Der experimentelle Nachweis der Richtungsquantelung im Magnetfeld', Zeitschrift für Physik **9**, 349–352 (1922).

[9] J. S. BELL, ‘On the problem of hidden variables in quantum mechanics’, Rev. Mod. Phys. **38**, 447–452 (1966).

[10] J. F. Clauser, M. A. Horne, A. Shimony and R. A. Holt, ‘Proposed experiment to test local hidden-variable theories’, Phys. Rev. Lett. **23**, 880–884 (1969).

[11] A. Aspect, P. Grangier and G. Roger, ‘Experimental realization of einstein-podolsky-rosen-bohm gedankenexperiment: a new violation of bell’s inequalities’, Phys. Rev. Lett. **49**, 91–94 (1982).

[12] G. Weihs, T. Jennewein, C. Simon, H. Weinfurter and A. Zeilinger, ‘Violation of bell’s inequality under strict einstein locality conditions’, Phys. Rev. Lett. **81**, 5039–5043 (1998).

[13] S. N. Bose, ‘Plancks gesetz und lichtquantenhypothese’, Zeitschrift Fur Physik **26**, 178–181 (1924).

[14] A. Einstein, ‘Quantentheorie des einatomigen idealen Gases, zweite Abhandlung’, **1**, 3–14 (1925).

[15] M. H. Anderson, J. R. Ensher, M. R. Matthews, C. E. Wieman and E. A. Cornell, ‘Observation of Bose-Einstein condensation in a dilute atomic vapor’, Science (New York, N.Y.) **269**, 198–201 (1995).

[16] K. B. Davis, M. .-. Mewes, M. R. Andrews, N. J. van Druten, D. S. Durfee, D. M. Kurn and W. Ketterle, ‘Bose-Einstein condensation in a gas of sodium atoms’, Physical Review Letters **75**, 3969–3973 (1995).

[17] B. DeMarco and D. S. Jin, ‘Onset of Fermi degeneracy in a trapped atomic gas’, Science (New York, N.Y.) **285**, 1703–1706 (1999).

[18] T. H. MAIMAN, ‘Stimulated Optical Radiation in Ruby’, Nature **187**, 493–494 (1960).

[19] J. Bardeen and W. H. Brattain, ‘The transistor, A semi-conductor triode’, Physical Review **74**, 230–231 (1948).

[20] A. G. J. MacFarlane, J. P. Dowling and G. J. Milburn, ‘Quantum technology: the second quantum revolution’, Philosophical Transactions of the Royal Society of London. Series A: Mathematical, Physical and Engineering Sciences **361**, 1655–1674 (2003).

[21] R. P. Feynman, ‘Simulating physics with computers’, International Journal of Theoretical Physics **21**, 467–488 (1982).

[22] I. Bloch, J. Dalibard and S. Nascimbène, ‘Quantum simulations with ultracold quantum gases’, Nature Physics **8**, 267–276 (2012).

[23] I. Bloch, J. Dalibard and W. Zwerger, ‘Many-body physics with ultracold gases’, Rev. Mod. Phys. **80**, 885–964 (2008).

[24] C. Chin, R. Grimm, P. Julienne and E. Tiesinga, ‘Feshbach resonances in ultracold gases’, Reviews of Modern Physics **82**, 1225–1286 (2010).

[25] T. Fukuhara, S. Sugawa and Y. Takahashi, ‘Bose-Einstein condensation of an ytterbium isotope’, Physical Review A: Atomic, Molecular, and Optical Physics **76**, 051604 (2007).

[26] M. Lu, N. Q. Burdick, S. H. Youn and B. L. Lev, ‘Strongly dipolar Bose-Einstein condensate of dysprosium’, Physical Review Letters **107**, 190401 (2011).

[27] K. Aikawa, A. Frisch, M. Mark, S. Baier, A. Rietzler, R. Grimm and F. Ferlaino, ‘Bose-einstein condensation of erbium’, Phys. Rev. Lett. **108**, 210401 (2012).

[28] E. T. Davletov, V. V. Tsyganok, V. A. Khlebnikov, D. A. Pershin, D. V. Shaykin and A. V. Akimov, ‘Machine learning for achieving bose-einstein condensation of thulium atoms’, Phys. Rev. A **102**, 011302 (2020).

[29] S. Levy, E. Lahoud, I. Shomroni and J. Steinhauer, ‘The a.c. and d.c. Josephson effects in a Bose–Einstein condensate’, Nature **449**, 579–583 (2007).

[30] C. G. Böhmer and T. Harko, 'Can dark matter be a bose–einstein condensate?', Journal of Cosmology and Astroparticle Physics **2007**, 025 (2007).

[31] M. Bashkanov and D. P. Watts, 'A new possibility for light-quark dark matter', Journal of Physics G: Nuclear and Particle Physics **47**, 03LT01 (2020).

[32] L. J. Garay, J. R. Anglin, J. I. Cirac and P. Zoller, 'Sonic analog of gravitational black holes in bose-einstein condensates', Phys. Rev. Lett. **85**, 4643–4647 (2000).

[33] M. Greiner, O. Mandel, T. Rom, A. Altmeyer, A. Widera, T. Hänsch and I. Bloch, 'Quantum phase transition from a superfluid to a mott insulator in an ultracold gas of atoms', Physica B: Condensed Matter **329-333**, Proceedings of the 23rd International Conference on Low Temperature Physics, 11–12 (2003).

[34] N. S. Ginsberg, S. R. Garner and L. V. Hau, 'Coherent control of optical information with matter wave dynamics', Nature **445**, 623–626 (2007).

[35] F. HOYLE and N. C. WICKRAMASINGHE, 'Impurities in Interstellar Grains', Nature **214**, 969–971 (1967).

[36] P. M. Pizzochero, F. Barranco, E. Vigezzi and R. A. Broglia, 'Nuclear impurities in the superfluid crust of neutron stars: quantum calculation and observable effects on the cooling', The Astrophysical Journal **569**, 381 (2002).

[37] H. Tamura, 'Impurity nuclear physics', The European Physical Journal A - Hadrons and Nuclei **13**, 181–187 (2002).

[38] C. Dong, S. Morita, M. Goto and H. Zhou, 'Space-resolved extreme ultraviolet spectrometer for impurity emission profile measurement in Large Helical Device', Review of Scientific Instruments **81**, 033107 (2010).

[39] S. J. Urwin, G. Levilain, I. Marziano, J. M. Merritt, I. Houson and J. H. Ter Horst, ‘A Structured Approach To Cope with Impurities during Industrial Crystallization Development’, Organic Process Research & Development **24**, 1443–1456 (2020).

[40] K. Yasui, ‘Critical roles of impurities and imperfections in various phases of materials’, Materials **16**, `10.3390/ma16041612` (2023).

[41] E. Fritsch and G. R. Rossman, ‘An update on color in gems. part 1: introduction and colors caused by dispersed metal ions’, Gems & Gemology **23**, 126–139 (1987).

[42] B. J. Murray, D. O’Sullivan, J. D. Atkinson and M. E. Webb, ‘Ice nucleation by particles immersed in supercooled cloud droplets’, Chem. Soc. Rev. **41**, 6519–6554 (2012).

[43] L. D. Landau and S. I. Pekar, ‘Effective mass of a polaron’, J. Exp. Theor. Phys. **18**, 419 (1948).

[44] M. G. Skou, ‘Quantum impurity dynamics and formation of polarons and bipolarons in bose-einstein condensates’, PhD thesis (Aarhus University, 2021).

[45] A. Schirotzek, C.-H. Wu, A. Sommer and M. W. Zwierlein, ‘Observation of Fermi polarons in a tunable Fermi liquid of ultracold atoms’, Physical Review Letters **102**, 230402 (2009).

[46] S. Nascimbène, N. Navon, K. J. Jiang, L. Tarruell, M. Teichmann, J. McKeever, F. Chevy and C. Salomon, ‘Collective oscillations of an imbalanced Fermi gas: Axial compression modes and polaron effective mass’, Physical Review Letters **103**, 170402 (2009).

[47] C. Kohstall, M. Zaccanti, M. Jag, A. Trenkwalder, P. Massignan, G. M. Bruun, F. Schreck and R. Grimm, ‘Metastability and coherence of repulsive polarons in a strongly interacting Fermi mixture’, Nature **485**, 615–618 (2012).

[48] M. Koschorreck, D. Pertot, E. Vogt, B. Fröhlich, M. Feld and M. Köhl, ‘Attractive and repulsive Fermi polarons in two dimensions’, Nature **485**, 619–622 (2012).

[49] F. Scazza, G. Valtolina, P. Massignan, A. Recati, A. Amico, A. Burchianti, C. Fort, M. Inguscio, M. Zaccanti and G. Roati, ‘Repulsive Fermi polarons in a resonant mixture of ultracold ^{6}Li atoms’, Physical Review Letters **118**, 083602 (2017).

[50] Z. Yan, P. B. Patel, B. Mukherjee, R. J. Fletcher, J. Struck and M. W. Zwierlein, ‘Boiling a unitary Fermi liquid’, Physical Review Letters **122**, 093401 (2019).

[51] N. B. Jørgensen, L. Wacker, K. T. Skalmstang, M. M. Parish, J. Levinsen, R. S. Christensen, G. M. Bruun and J. J. Arlt, ‘Observation of attractive and repulsive polarons in a Bose-Einstein condensate’, Physical Review Letters **117**, 055302 (2016).

[52] M.-G. Hu, M. J. Van de Graaff, D. Kedar, J. P. Corson, E. A. Cornell and D. S. Jin, ‘Bose polarons in the strongly interacting regime’, Physical Review Letters **117**, 055301 (2016).

[53] L. A. Peña Ardila, N. B. Jørgensen, T. Pohl, S. Giorgini, G. M. Bruun and J. J. Arlt, ‘Analyzing a Bose polaron across resonant interactions’, Physical Review A: Atomic, Molecular, and Optical Physics **99**, 063607 (2019).

[54] Z. Z. Yan, Y. Ni, C. Robens and M. W. Zwierlein, ‘Bose polarons near quantum criticality’, Science (New York, N.Y.) **368**, 190–194 (2020).

[55] M. Cetina, M. Jag, R. S. Lous, J. T. M. Walraven, R. Grimm, R. S. Christensen and G. M. Bruun, ‘Decoherence of impurities in a Fermi sea of ultracold atoms’, Physical Review Letters **115**, 135302 (2015).

[56] M. Cetina, M. Jag, R. S. Lous, I. Fritsche, J. T. M. Walraven, R. Grimm, J. Levinsen, M. M. Parish, R. Schmidt, M. Knap and E. Demler, ‘Ultrafast many-body interferometry of impurities coupled to a fermi sea’, Science **354**, 96–99 (2016).

[57] M. G. Skou, T. G. Skov, N. B. Jørgensen, K. K. Nielsen, A. Camacho-Guardian, T. Pohl, G. M. Bruun and J. J. Arlt, ‘Non-equilibrium quantum dynamics and formation of the Bose polaron’, Nature Physics **17**, 731–735 (2021).

[58] A. Camacho-Guardian, L. A. Peña Ardila, T. Pohl and G. M. Bruun, ‘Bipolarons in a Bose-Einstein condensate’, Physical Review Letters **121**, 013401 (2018).

[59] P. Naidon, ‘Two impurities in a Bose–Einstein condensate: From yukawa to efimov attracted polarons’, Journal of the Physical Society of Japan **87**, 043002 (2018).

[60] M. Will, G. E. Astrakharchik and M. Fleischhauer, ‘Polaron interactions and bipolarons in one-dimensional bose gases in the strong coupling regime’, Phys. Rev. Lett. **127**, 103401 (2021).

[61] A. S. Dehkharghani, A. G. Volosniev and N. T. Zinner, ‘Coalescence of two impurities in a trapped one-dimensional bose gas’, Phys. Rev. Lett. **121**, 080405 (2018).

[62] L. N. Cooper, ‘Bound electron pairs in a degenerate fermi gas’, Phys. Rev. **104**, 1189–1190 (1956).

[63] A. S. Alexandrov and N. F. Mott, ‘Bipolarons’, Reports on Progress in Physics **57**, 1197–1288 (1994).

[64] M. E. Gershenson, V. Podzorov and A. F. Morpurgo, ‘*Colloquium* : Electronic transport in single-crystal organic transistors’, Reviews of Modern Physics **78**, 973–989 (2006).

[65] J. L. Bredas and G. B. Street, ‘Polarons, bipolarons, and solitons in conducting polymers’, Accounts of Chemical Research **18**, 309–315 (1985).

[66] P. A. Bobbert, T. D. Nguyen, F. W. A. van Oost, B. Koopmans and M. Wohlgenannt, ‘Bipolaron mechanism for organic magnetoresistance’, Physical Review Letters **99**, 216801 (2007).

[67] A. Christianen, J. I. Cirac and R. Schmidt, ‘Bose polaron and the Efimov effect: A Gaussian-state approach’, Physical Review A: Atomic, Molecular, and Optical Physics **105**, 053302 (2022).

[68] C. Baroni, B. Huang, I. Fritsche, E. Dobler, G. Anich, E. Kirilov, R. Grimm, M. A. Bastarrachea-Magnani, P. Massignan and G. M. Bruun, ‘Mediated interactions between Fermi polarons and the role of impurity quantum statistics’, Nature Physics **20**, 68–73 (2024).

[69] J. J. Kinnunen, Z. Wu and G. M. Bruun, ‘Induced p-wave pairing in bose-fermi mixtures’, Phys. Rev. Lett. **121**, 253402 (2018).

[70] S. Ding, M. Drewsen, J. J. Arlt and G. M. Bruun, ‘Mediated interaction between ions in quantum degenerate gases’, Phys. Rev. Lett. **129**, 153401 (2022).

[71] V. Efimov, ‘Energy levels arising from resonant two-body forces in a three-body system’, Physics Letters B **33**, 563–564 (1970).

[72] V. Efimov, ‘Weakly-bound states of three resonantly-interacting particles’, Sov. J. Nucl. Phys. **12**, 589–595 (1971).

[73] T. Kraemer, M. Mark, P. Waldburger, J. G. Danzl, C. Chin, B. Engeser, A. D. Lange, K. Pilch, A. Jaakkola, H.-C. Nägerl and R. Grimm, ‘Evidence for Efimov quantum states in an ultracold gas of caesium atoms’, Nature **440**, 315–318 (2006).

[74] M. Zaccanti, B. Deissler, C. D'Errico, M. Fattori, M. Jona-Lasinio, S. Müller, G. Roati, M. Inguscio and G. Modugno, 'Observation of an Efimov spectrum in an atomic system', Nature Physics **5**, 586–591 (2009).

[75] N. Gross, Z. Shotan, S. Kokkelmans and L. Khaykovich, 'Observation of universality in ultracold ^{7}Li three-body recombination', Phys. Rev. Lett. **103**, 163202 (2009).

[76] T. Lompe, T. B. Ottenstein, F. Serwane, A. N. Wenz, G. Zürn and S. Jochim, 'Radio-frequency association of efimov trimers', Science **330**, 940–944 (2010).

[77] S. E. Pollack, D. Dries and R. G. Hulet, 'Universality in three- and four-body bound states of ultracold atoms', Science **326**, 1683–1685 (2009).

[78] P. Naidon and S. Endo, 'Efimov physics: a review', Reports on Progress in Physics **80**, 056001 (2017).

[79] S. M. Yoshida, S. Endo, J. Levinsen and M. M. Parish, 'Universality of an impurity in a Bose-Einstein condensate', Physical Review X **8**, 011024 (2018).

[80] J. Levinsen, M. M. Parish and G. M. Bruun, 'Impurity in a Bose-Einstein condensate and the Efimov effect', Physical Review Letters **115**, 125302 (2015).

[81] C. J. Pethick and H. Smith, *Bose-Einstein condensation in dilute gases*, Second Edition (Cambridge University Press, 2008).

[82] S. Giorgini, L. P. Pitaevskii and S. Stringari, 'Condensate fraction and critical temperature of a trapped interacting Bose gas', Physical Review A: Atomic, Molecular, and Optical Physics **54**, R4633–R4636 (1996).

[83] S. Grossmann and M. Holthaus, 'On bose-einstein condensation in harmonic traps', Physics Letters A **208**, 188–192 (1995).

[84] E. A. Donley, N. R. Claussen, S. L. Cornish, J. L. Roberts, E. A. Cornell and C. E. Wieman, 'Dynamics of collapsing and exploding Bose–Einstein condensates', Nature **412**, 295–299 (2001).

[85] P. A. Altin, G. R. Dennis, G. D. McDonald, D. Döring, J. E. Debs, J. D. Close, C. M. Savage and N. P. Robins, 'Collapse and three-body loss in a ^{85}rb bose-einstein condensate', Phys. Rev. A **84**, 033632 (2011).

[86] T. Weber, J. Herbig, M. Mark, H.-C. Nägerl and R. Grimm, 'Three-body recombination at large scattering lengths in an ultracold atomic gas', Phys. Rev. Lett. **91**, 123201 (2003).

[87] L. D. Landau, 'Über die bewegung der elektronen in kristalgitter', Physikalische Zeitschrift der Sowjetunion **3**, 644 (1933).

[88] S. I. Pekar, 'Autolocalization of the electron in an inertially polarizable dielectric medium', Zh. Eksp. Teor. Fiz. **16**, 335 (1946).

[89] H. Fröhlich, 'Electrons in lattice fields', Advances in Physics **3**, 325–361 (1954).

[90] A. S. Alexandrov and J. T. Devreese, *Advances in polaron physics*, Vol. 159 (Springer-Verlag Berlin Heidelberg, 2010).

[91] F. Scazza, M. Zaccanti, P. Massignan, M. M. Parish and J. Levinsen, 'Repulsive fermi and bose polarons in quantum gases', Atoms **10**, `10.3390/atoms10020055` (2022).

[92] G. Baym and C. Pethick, *Landau Fermi-Liquid theory: Concepts and applications* (Wiley-VCH, 1991).

[93] J. Kondo, 'Resistance minimum in dilute magnetic alloys', Progress of Theoretical Physics **32**, 37–49 (1964).

[94] R. S. Christensen, J. Levinsen and G. M. Bruun, 'Quasiparticle properties of a mobile impurity in a Bose-Einstein condensate', Physical Review Letters **115**, 160401 (2015).

[95] A. Novikov and M. Ovchinnikov, ‘A diagrammatic calculation of the energy spectrum of quantum impurity in degenerate bose–einstein condensate’, Journal of Physics A: Mathematical and Theoretical **42**, 135301 (2009).

[96] W. Casteels and M. Wouters, ‘Polaron formation in the vicinity of a narrow Feshbach resonance’, Physical Review A: Atomic, Molecular, and Optical Physics **90**, 043602 (2014).

[97] W. Li and S. Das Sarma, ‘Variational study of polarons in Bose-Einstein condensates’, Physical Review A: Atomic, Molecular, and Optical Physics **90**, 013618 (2014).

[98] B. Field, J. Levinsen and M. M. Parish, ‘Fate of the Bose polaron at finite temperature’, Physical Review A: Atomic, Molecular, and Optical Physics **101**, 013623 (2020).

[99] S. P. Rath and R. Schmidt, ‘Field-theoretical study of the Bose polaron’, Physical Review A: Atomic, Molecular, and Optical Physics **88**, 053632 (2013).

[100] N.-E. Guenther, P. Massignan, M. Lewenstein and G. M. Bruun, ‘Bose polarons at finite temperature and strong coupling’, Physical Review Letters **120**, 050405 (2018).

[101] L. A. P. Ardila and S. Giorgini, ‘Impurity in a bose-einstein condensate: study of the attractive and repulsive branch using quantum monte carlo methods’, Phys. Rev. A **92**, 033612 (2015).

[102] L. A. Peña Ardila, G. E. Astrakharchik and S. Giorgini, ‘Strong coupling Bose polarons in a two-dimensional gas’, Physical Review Research **2**, 023405 (2020).

[103] F. Chevy, ‘Universal phase diagram of a strongly interacting Fermi gas with unbalanced spin populations’, Physical Review A: Atomic, Molecular, and Optical Physics **74**, 063628 (2006).

[104] H. S. Adlong, W. E. Liu, F. Scazza, M. Zaccanti, N. D. Oppong, S. Fölling, M. M. Parish and J. Levinsen, 'Quasiparticle lifetime of the repulsive fermi polaron', Phys. Rev. Lett. **125**, 133401 (2020).

[105] N. Mostaan, N. Goldman and F. Grusdt, 'A unified theory of strong coupling bose polarons: from repulsive polarons to non-gaussian many-body bound states', arXiv:2305.00835 (2023).

[106] J. Etrych, G. Martirosyan, A. Cao, C. J. Ho, Z. Hadzibabic and C. Eigen, 'Universal quantum dynamics of Bose polarons', arXiv:2402.14816 (2024).

[107] P. Massignan, M. Zaccanti and G. M. Bruun, 'Polarons, dressed molecules and itinerant ferromagnetism in ultracold fermi gases', Reports on Progress in Physics **77**, 034401 (2014).

[108] R. Schmidt, M. Knap, D. A. Ivanov, J.-S. You, M. Cetina and E. Demler, 'Universal many-body response of heavy impurities coupled to a Fermi sea: a review of recent progress', Reports on Progress in Physics **81**, 024401 (2018).

[109] M. M. Parish and J. Levinsen, 'Fermi polarons and beyond', arXiv:2306.01215 (2023).

[110] F. Grusdt, R. Schmidt, Y. E. Shchadilova and E. Demler, 'Strong-coupling bose polarons in a bose-einstein condensate', Phys. Rev. A **96**, 013607 (2017).

[111] Y. E. Shchadilova, R. Schmidt, F. Grusdt and E. Demler, 'Quantum dynamics of ultracold Bose polarons', Physical Review Letters **117**, 113002 (2016).

[112] A. Christianen, J. I. Cirac and R. Schmidt, 'Phase diagram for strong-coupling Bose polarons', SciPost Phys. **16**, 067 (2024).

[113] A. S. Alexandrov, 'Unconventional pairing symmetry of layered superconductors caused by acoustic phonons', Phys. Rev. B **77**, 094502 (2008).

[114] M. Hohenadler and P. B. Littlewood, ‘Quantum Monte Carlo results for bipolaron stability in quantum dots’, Physical Review B **76**, 155122 (2007).

[115] A. Camacho-Guardian and G. M. Bruun, ‘Landau effective interaction between quasiparticles in a Bose-Einstein condensate’, Physical Review X **8**, 031042 (2018).

[116] W. Casteels, J. Tempere and J. T. Devreese, ‘Bipolarons and multipolarons consisting of impurity atoms in a bose-einstein condensate’, Phys. Rev. A **88**, 013613 (2013).

[117] K.-B. Georg, ‘Lange kohärenzzeit optisch gefangener ensembles’, PhD thesis (Leibniz Universität Hannover, 2012).

[118] J. Will, ‘Symmetrieabhängige frequenzverschiebungen in atomuhren’, PhD thesis (Leibniz Universität Hannover, 2012).

[119] G. Kleine Büning, J. Will, W. Ertmer, C. Klempt and J. Arlt, ‘A slow gravity compensated atom laser’, Applied Physics B **100**, 117–123 (2010).

[120] G. Kleine Büning, J. Will, W. Ertmer, E. Rasel, J. Arlt, C. Klempt, F. Ramirez-Martinez, F. Piéchon and P. Rosenbusch, ‘Extended coherence time on the clock transition of optically trapped rubidium’, Physical Review Letters **106**, 240801 (2011).

[121] N. Winter, ‘Creation of ^{39}K Bose-Einstein Condensates with Tunable Interactions’, PhD thesis (Aarhus University, 2013).

[122] L. Wacker, ‘Few-body physics with ultracold potassium rubidium mixtures’, PhD thesis (Aarhus University, 2015).

[123] N. B. Jørgensen, ‘Observation of Bose polarons in a quantum gas mixture’, PhD thesis (Aarhus University, 2018).

[124] T. G. Skov, ‘Observation of a Lee-Huan-Yang Fluid’, PhD thesis (Aarhus University, 2021).

[125] L. Wacker, N. B. Jørgensen, D. Birkmose, R. Horchani, W. Ertmer, C. Klempt, N. Winter, J. Sherson and J. J. Arlt, 'Tunable dual-species bose-einstein condensates of ^{39}K and ^{87}Rb', Phys. Rev. A **92**, 053602 (2015).

[126] D. A. Steck, 'Rubidium 87 d line data', available online (revision 2.3.3, 28 May, 2024).

[127] L. G. Marcassa, G. D. Telles, S. R. Muniz and V. S. Bagnato, 'Collisional losses in a K-Rb cold mixture', Physical Review A: Atomic, Molecular, and Optical Physics **63**, 013413 (2000).

[128] U. Schlöder, H. Engler, U. Schünemann, R. Grimm and M. Weidemüller, 'Cold inelastic collisions between lithium and cesium in a two-species magneto-optical trap', The European Physical Journal D - Atomic, Molecular, Optical and Plasma Physics **7**, 331–340 (1999).

[129] M. Landini, S. Roy, L. Carcagní, D. Trypogeorgos, M. Fattori, M. Inguscio and G. Modugno, 'Sub-Doppler laser cooling of potassium atoms', Physical Review A: Atomic, Molecular, and Optical Physics **84**, 043432 (2011).

[130] T. Esslinger, I. Bloch and T. W. Hänsch, 'Bose-Einstein condensation in a quadrupole-Ioffe-configuration trap', Physical Review A: Atomic, Molecular, and Optical Physics **58**, R2664–R2667 (1998).

[131] L. Tanzi, C. R. Cabrera, J. Sanz, P. Cheiney, M. Tomza and L. Tarruell, 'Feshbach resonances in potassium Bose-Bose mixtures', Physical Review A: Atomic, Molecular, and Optical Physics **98**, 062712 (2018).

[132] G. Reinaudi, T. Lahaye, Z. Wang and D. Guéry-Odelin, 'Strong saturation absorption imaging of dense clouds of ultracold atoms', Opt. Lett. **32**, 3143–3145 (2007).

[133] T. G. Tiecke, 'Properties of Potassium', available online (revision 1.03, June, 2019).

[134] T. Vibel, M. B. Christensen, M. A. Kristensen, J. J. Thuesen, L. N. Stokholm, C. A. Weidner and J. J. Arlt, 'Spatial calibration of high-density absorption imaging', Journal of Physics B: Atomic, Molecular and Optical Physics **57**, 145301 (2024).

[135] J. C. B. Kangara, A. J. Hachtel, M. C. Gillette, J. T. Barkeloo, E. R. Clements, S. Bali, B. E. Unks, N. A. Proite, D. D. Yavuz, P. J. Martin, J. J. Thorn and D. A. Steck, 'Design and construction of cost-effective tapered amplifier systems for laser cooling and trapping experiments', American Journal of Physics **82**, 805–817 (2014).

[136] G. Salomon, L. Fouché, P. Wang, A. Aspect, P. Bouyer and T. Bourdel, 'Gray-molasses cooling of 39k to a high phase-space density', Europhysics Letters **104**, 63002 (2014).

[137] E. Braaten, D. Kang and L. Platter, 'Short-time operator product expansion for rf spectroscopy of a strongly interacting Fermi gas', Physical Review Letters **104**, 223004 (2010).

[138] J. Söding, D. Guéry-Odelin, P. Desbiolles, F. Chevy, H. Inamori and J. Dalibard, 'Three-body decay of a rubidium Bose–Einstein condensate', Applied Physics B **69**, 257–261 (1999).

[139] E. A. Burt, R. W. Ghrist, C. J. Myatt, M. J. Holland, E. A. Cornell and C. E. Wieman, 'Coherence, correlations, and collisions: what one learns about bose-einstein condensates from their decay', Phys. Rev. Lett. **79**, 337–340 (1997).

[140] L. J. Wacker, N. B. Jørgensen, K. T. Skalmstang, M. G. Skou, A. G. Volosniev and J. J. Arlt, 'Temperature dependence of an Efimov resonance in ^{39}K', Physical Review A: Atomic, Molecular, and Optical Physics **98**, 052706 (2018).

[141] J. ř. Etrych, G. Martirosyan, A. Cao, J. A. P. Glidden, L. H. Dogra, J. M. Hutson, Z. Hadzibabic and C. Eigen, 'Pinpointing feshbach resonances and testing efimov universalities in ^{39}K', Phys. Rev. Res. **5**, 013174 (2023).

[142] L. J. Wacker, N. B. Jørgensen, D. Birkmose, N. Winter, M. Mikkelsen, J. Sherson, N. Zinner and J. J. Arlt, 'Universal three-body physics in ultracold KRb mixtures', Physical Review Letters **117**, 163201 (2016).

[143] P. Cheiney, C. R. Cabrera, J. Sanz, B. Naylor, L. Tanzi and L. Tarruell, 'Bright soliton to quantum droplet transition in a mixture of bose-einstein condensates', Phys. Rev. Lett. **120**, 135301 (2018).

[144] G. Semeghini, G. Ferioli, L. Masi, C. Mazzinghi, L. Wolswijk, F. Minardi, M. Modugno, G. Modugno, M. Inguscio and M. Fattori, 'Self-bound quantum droplets of atomic mixtures in free space', Phys. Rev. Lett. **120**, 235301 (2018).

[145] T. G. Skov, M. G. Skou, N. B. Jørgensen and J. J. Arlt, 'Observation of a lee-huang-yang fluid', Phys. Rev. Lett. **126**, 230404 (2021).

[146] S. Lepoutre, L. Fouché, A. Boissé, G. Berthet, G. Salomon, A. Aspect and T. Bourdel, 'Production of strongly bound ^{39}K bright solitons', Phys. Rev. A **94**, 053626 (2016).

[147] R. A. W. Maier, M. Eisele, E. Tiemann and C. Zimmermann, 'Efimov resonance and three-body parameter in a lithium-rubidium mixture', Phys. Rev. Lett. **115**, 043201 (2015).

[148] R. Pires, J. Ulmanis, S. Häfner, M. Repp, A. Arias, E. D. Kuhnle and M. Weidemüller, 'Observation of efimov resonances in a mixture with extreme mass imbalance', Phys. Rev. Lett. **112**, 250404 (2014).

[149] S.-K. Tung, K. Jiménez-García, J. Johansen, C. V. Parker and C. Chin, 'Geometric scaling of efimov states in a $^{6}\mathrm{Li}-^{133}\mathrm{Cs}$ mixture', Phys. Rev. Lett. **113**, 240402 (2014).

[150] S. Roy, M. Landini, A. Trenkwalder, G. Semeghini, G. Spagnolli, A. Simoni, M. Fattori, M. Inguscio and G. Modugno, 'Test of the universality of the three-body efimov parameter at narrow feshbach resonances', Physical Review Letters **111**, 053202 (2013).

[151] J. P. D'Incao and B. D. Esry, 'Scattering length scaling laws for ultracold three-body collisions', Phys. Rev. Lett. **94**, 213201 (2005).

[152] K. Helfrich, H.-W. Hammer and D. S. Petrov, 'Three-body problem in heteronuclear mixtures with resonant interspecies interaction', Phys. Rev. A **81**, 042715 (2010).

[153] R. Chapurin, X. Xie, M. J. Van de Graaff, J. S. Popowski, J. P. D'Incao, P. S. Julienne, J. Ye and E. A. Cornell, 'Precision test of the limits to universality in few-body physics', Phys. Rev. Lett. **123**, 233402 (2019).

[154] J. Schuster, A. Marte, S. Amtage, B. Sang, G. Rempe and H. C. W. Beijerinck, 'Avalanches in a bose-einstein condensate', Phys. Rev. Lett. **87**, 170404 (2001).

[155] K. K. Nielsen, L. A. Peña Ardila, G. M. Bruun and T. Pohl, 'Critical slowdown of non-equilibrium polaron dynamics', New Journal of Physics **21**, 043014 (2019).

[156] N. F. Ramsey, 'A new molecular beam resonance method', Physical Review **76**, 996–996 (1949).

[157] P. W. Anderson, 'Infrared catastrophe in fermi gases with local scattering potentials', Phys. Rev. Lett. **18**, 1049–1051 (1967).

[158] N.-E. Guenther, R. Schmidt, G. M. Bruun, V. Gurarie and P. Massignan, 'Mobile impurity in a Bose-Einstein condensate and the orthogonality catastrophe', Physical Review A: Atomic, Molecular, and Optical Physics **103**, 013317 (2021).

[159] E. Q. Simmons, R. Sajjad, K. Keithley, H. Mas, J. L. Tanlimco, E. Nolasco-Martinez, Y. Bai, G. H. Fredrickson and D. M. Weld, 'Thermodynamic engine with a quantum degenerate working fluid', Phys. Rev. Res. **5**, L042009 (2023).

[160] Y.-Y. Chen, G. Watanabe, Y.-C. Yu, X.-W. Guan and A. del Campo, 'An interaction-driven many-particle quantum heat engine and its universal behavior', npj Quantum Information **5**, 88 (2019).

[161] O. Abah, M. Paternostro and E. Lutz, 'Shortcut-to-adiabaticity quantum otto refrigerator', Phys. Rev. Res. **2**, 023120 (2020).

[162] J. Koch, K. Menon, E. Cuestas, S. Barbosa, E. Lutz, T. Fogarty, T. Busch and A. Widera, 'A quantum engine in the BEC–BCS crossover', Nature **621**, 723–727 (2023).

[163] J. A. Estrada, F. Mayo, A. J. Roncaglia and P. D. Mininni, 'Quantum engines with interacting bose-einstein condensates', Phys. Rev. A **109**, 012202 (2024).